Milad Asslan

Evolution of Small Strain Shear Stiffness by Fabric Changes in Granular Materials

Schriftenreihe des Lehrstuhls
Geomechanik und Geotechnik
Christian-Albrechts-Universität zu Kiel

5

Schriftenreihe des Lehrstuhls Geomechanik und Geotechnik
Christian-Albrechts-Universität zu Kiel
Heft 5

ISSN 2365-7162

Herausgeber:

Lehrstuhl für Geomechanik und Geotechnik

Christian-Albrechts-Universität zu Kiel

Prof. Dr.-Ing. habil. Frank Wuttke

Ludewig-Meyn-Straße 10

24118 Kiel

Telefon: ++49 – (0)431 – 880 2857

Telefax: ++49 – (0)431 – 880 7606

Internet: www.geotechnics.ifg.uni-kiel.de

Bezugsadresse:

Christian-Albrechts-Universität zu Kiel
Lehrstuhl für Geomechanik und Geotechnik

Evolution of Small Strain Shear Stiffness by Fabric Changes in Granular Materials

Dissertation

in fulfilment of the requirements for the degree "Dr.-Ing."
of the Faculty of Mathematics and Natural Sciences at
Christian-Albrechts-Universität zu Kiel

submitted by

Milad Asslan

Kiel, 2020

Gutachter:

1. Prof. Dr.-Ing. habil. Frank Wuttke
   Christian-Albrechts-Universität zu Kiel

2. Prof. Dr. Thomas Nagel
   Technische Universität Bergakademie Freiberg

Tag der mündlichen Prüfung: 19.02.2020
Zum Druck genehmigt: 27.08.2020

Der Dekan

Vorwort des Herausgebers

Die vorliegende Promotionsschrift von Herrn Dr.-Ing. Milad Asslan ist dem Forschungs- und Arbeitsgebiet der „Bodenmechanik“ und der „Bodendynamik“ zuzuordnen. Die der Arbeit zugrundeliegende Problemstellung hatte sich in der Bearbeitung von offenen Fragen auf dem Gebiet der Bodendynamik im Monitoring des Bodenverhaltens ergeben, besitzt jedoch durch die Bereitstellung von Bodenparametern und der funktionalen Beschreibung der Parameter einen Einfluss in der gesamten Geotechnik. Die Zielstellung der Promotionsarbeit liegt auf der Entwicklung von geeigneten experimentellen Methoden zum Monitoring von Schersteifigkeiten in granularen Materialien unter Mehrphaseneinfluss oder weiteren Strukturänderungen im Material. Als Grundlage der Beschreibung dient die Codawellen-Interferometrie von seismischen Wellenfeldern. In der Auswertungsmethodik wurden verschiedene Herangehensweisen analysiert. Die geeignetste Methodik wurde für die weiteren Analysen in der Modellbildung genutzt. Basierend auf unterschiedlich komplexen Hertzkontaktmodellen erfolgte eine Sensitivitätsanalyse hinsichtlich der notwendigen Komplexität in der Modellbeschreibung. Dazu wurden neben den klassischen Hertzkontakten, die Reibung, die Kornform und die Dichte der granularen Packungen analysiert. Mit der Anwendung der Erkenntnisse auf das Materialkriechen oder die Modelle zur Schersteifigkeit ungesättigter granularer Böden wurden neue funktionale Parameterbeschreibungen abgeleitet. Zur Verallgemeinerung der Bestimmung der Schersteifigkeit in ungesättigten Böden erfolgte die Verknüpfung der funktionalen Steifigkeitsbeschreibung mit der theoretischen Bestimmung der Saugspannungskurve (SWCC), die durch die Eingangsinformationen, wie die Sieblinie und die Dichte der Kornpackung, ermittelt wird. Die Schubsteifigkeit von Böden kann damit basierend auf Informationen zur Sieblinie und Dichte für unterschiedliche Sättigungsgrade bzw. Saugspannungen ermittelt werden. Die Dissertationsschrift beinhaltet damit die konsequente Übertragung des bodendynamischen Monitorings in funktionale Beschreibungen von erforderlichen Bodenparametern abhängig von Struktur- oder Wassergehaltsänderungen. In zahlreichen Validierungsstudien an unterschiedlichen experimentellen Ergebnissen wurde die hohe Prognosefähigkeit der entwickelten Modelle in der Dissertationsschrift dokumentiert. Mit der vorliegenden Arbeit lassen sich die Steifigkeiten von Böden bei sehr kleinen Dehnungsbereichen realitätsnah ermitteln und sicher als Funktion der Materialänderung abbilden.

Kiel, im Mai 2020 Frank Wuttke

Declaration of Authorship

I declare that, apart from the guidance of my supervisor, the content of this thesis is all my own work and no other sources than the ones listed were used. This work has not been submitted either partially or wholly as part of a doctoral degree to any other examining body and has not been published or submitted for publication. The thesis was prepared following the rules of good scientific practice of the German Research Foundation. Furthermore, an academic degree of mine has never been withdrawn.

Kiel, 29.11.2019 Milad Asslan

Acknowledgment

The experimental part of this work was carried out in Bauhaus-University Weimar. The Post Graduate Funding Program of the Free State of Thuringia is very much appreciated for its financial support of this research.

I am deeply grateful to many people who were directly or indirectly involved in this work. First and foremost, I would like to thank my supervisor Prof. Dr.-Ing. Frank Wuttke for his scientific guidance, patience, as well as encouragement during this lengthy process. Without his support, the completion of this research would not have been possible. Many thanks to Prof. Dr. Thomas Nagel for agreeing to review this dissertation.

Genuine gratitude is due to my former colleague at Bauhaus-University and friend Dr.-Ing. Jamal Alabdullah for countless valuable discussions on the subject of unsaturated soils. These discussions led to constructive ideas thanks to his knowledge in this field and experience in laboratory. I also would like to thank Mr. Frank Hoppe for his emotional support and assistance in laboratory. His cheerful spirit is deeply appreciated.

I sincerely Acknowledge the great patience my wife, Kholoud, showed. The pressure in our lives was immense since we had a baby, and I was working full time next to my thesis. She took a bigger share of that pressure to give me space to keep going forward. I am so thankful for all that she offered to make this happen.

Many thanks are due to my family for their support, understanding and encouragement. My parents had a great influence on my insistence on finishing this work. They prepared me from a young age and gave me the mindset to fight through it. My father, a doctor civil engineer, was always the role model I wanted to follow. I feel so blessed to be a part of this family.

This work is dedicated to the soul of my uncle, Nazih Kherbek. He was a professor of geotechnics and head of the department of geotechnics at Tishreen University in Latakia, Syria. He had a great influence on my life and was a second father to me, delivering emotional support all my life. He suddenly passed away during my work. I think he would be very proud of me now.

Milad Asslan

To the soul of my uncle N. Kherbek (1952-2009)
a former professor of geotechnics

Abstract

The initial shear stiffness at small strain is a significant factor to consider for a wide range of geotechnical applications. Determining this initial parameter is critical for describing dynamic soil behavior in the case of wave, wind, machine or traffic vibrations. It is very sensitive to fabric changing processes. Monitoring shear wave velocity, which is directly related to shear stiffness, is an effective tool to detect these fabric changing processes in soil, such as creep and unsaturation. The complex behavior of initial soil parameters, namely initial shear stiffness and shear wave velocity, under consideration of multiphase conditions and time effect, is in the focus of this research. Fabric changing processes were detected experimentally using a signal processing tool called coda wave interferometry and described mathematically.

The properties of soils change with time in a phenomenon called creep. This change has a significant impact on engineering practice since it causes long term settlements of foundations, piles and slopes. The evolution of shear stiffness during creep is established in this research based on measuring shear wave velocity, and a model is accordingly described. This model includes, in addition to the time effect, other physical soil properties at the micro scale, such as particle parameters (interparticle friction, angularity and grain properties) and state parameters (coordination number and confining pressure).

When soils are subjected to change in water content, knowledge of unsaturated soils is required for many engineering applications such as dams, slopes and stability excavations. In this thesis, semi-empirical and numerical approaches to predict a relationship between initial shear stiffness and degree of saturation are presented. In the semi-empirical approach, analytical models that link shear wave velocity to matric suction or degree of saturation based on experimental data are presented. Additionally, a numerical approach that predicts the soil-water characteristic curve (SWCC) can be used in the absence of experimental data. The analytical models from the semi-empirical approach associated with the numerical approach allow predicting change in shear wave velocity based on easy to obtain soil properties. This gives researchers and engineers a valuable tool to assess the dynamic behavior of unsaturated soils for different degrees of saturation.

Zusammenfassung

Die Schubsteifigkeit bei kleinen Dehnungsamplituden ist ein signifikanter Faktor für verschiedene geotechnische Anwendungsbereiche. Die Feststellung dieses Parameters ist entscheidend, um das dynamische Bodenverhalten unter Ereignissen wie Windlasten, maschinen- oder verkehrsbedingte Vibrationen beschreiben zu können. Dieser Parameter wird maßgeblich von strukturverändernden Prozessen beeinflusst. Das Monitoring der Scherwellengeschwindigkeit, welche mit der Schubsteifigkeit direkt korreliert, ist eine effektive Methode, um strukturverändernde Bodenprozesse, wie Kriechen und Sättigungsänderung, zu erkennen. Die vorliegende Arbeit widmet sich der Erforschung des komplexen Verhaltens der initialen Schubsteifigkeit und der Scherwellengeschwindigkeit, vor allem unter Berücksichtigung der Mehrphasen und des Zeiteffektes. Die strukturändernden Prozesse wurden durch die Codawellen-Interferometrie abgebildet und durch mathematisch-physikalische Gesetze beschrieben.

Die Eigenschaften von Böden ändern sich mit der Zeit durch Kriechprozesse. Diese Änderungen verursachen Langzeit-Setzungen bei Fundamenten, Pfählen und Böschungen. Die Änderungen der Schubsteifigkeit während des Kriechvorganges wurden, mithilfe von Scherwellen, analysiert und aufbauend entsprechende Modelle entwickelt. Diese Modelle beinhalten, zusätzlich zum Zeiteffekt, weitere physikalische Bodeneigenschaften, wie z.B. Interpartikelreibung, Kornform, Koordinationszahl und Druck.

Mit der Änderung des Wassergehaltes in Dämmen, Böschungen und Baugruben, muss die Theorie ungesättigter Böden im Design genutzt werden. In der vorliegenden Arbeit wurden semi-empirische und numerische Ansätze vorgestellt, um das Verhältnis zwischen dem Schubmodul und der Wassersättigung abzubilden. Im semi-empirischen Ansatz wurden analytische Modelle, die die Scherwellengeschwindigkeit mit der Saugspannung oder der Sättigung koppeln, abgeleitet. Der numerische Ansatz kann verallgemeinernd bei Abwesenheit von experimentellen Daten genutzt werden, um eine Saugspannungskurve in Abhängigkeit von der Sieblinie zu bestimmen. Zusammen mit dem analytischen Model zum semi-empirischen Ansatz, kann der numerische Ansatz die Änderungen in der Scherwellengeschwindigkeit prognostizieren. Dies erlaubt, das dynamische Verhalten von ungesättigten Böden bei verschiedenen Sättigungsgraden zu beurteilen.

Contents

List of Figures

List of Tables

Chapter 1

Introduction

1.1 Background and motivations

The small strain shear stiffness or initial shear modulus, G_{max}, is an important parameter for a variety of geotechnical designs and applications. The critical role of soil stiffness at small strains in the design and analysis of geotechnical infrastructure is nowadays widely accepted. G_{max} is a key parameter for many geotechnical, dynamic and static analysis. Determining this initial parameter in the small strain range is crucial for describing and predicting soil behavior or soil-structure interaction in the case of far earthquakes, wind loading and machine or traffic vibrations. The initial shear stiffness is equally essential for small strain cyclic situations, such as those caused by wind or wave loading and also for small strain static situations.

The small strain shear stiffness is very sensitive to fabric changing processes, such as processes involving creep and unsaturation. Monitoring shear wave velocity, which is directly related to shear stiffness, is a powerful tool to model the essential soil property of shear stiffness for granular materials under considerations of these two phenomena. Understanding these fabric changing processes, namely creep and unsaturation, has implications in engineering practice, as explained in the next paragraphs.

Soils age and their properties change with time. This change has a significant impact on engineering practice. Creep causes long term settlements of foundations and piles, and thus compromising the safety of buildings based on them.

Additionally, creep increases the capacity of driven piles, small strain shear stiffness and resistance of penetration test, among others. It can have positive and negative outcomes and covers a wide range of geotechnical applications, such as deformation of earth structures, slope stability and deforming of soil around tunnels, to name a few. Exploring these effects has substantial engineering applications and economical benefits. Creep in sand was considerably less studied in the literature than clay, despite the significant applications of investigating the time effect on sand. A model that captures this effect under consideration of granular material would be a considerable contribution to this field.

In most geotechnical analyses, a two-phase system is assumed, a system of particles and fluid-filled voids. It was realized in the last couple of decades that this system does not meet the requirements of engineering practice, where soils are mostly unsaturated. However, since traditional soil mechanics was historically dominant, the majority of researches concerned with G_{max} was done on a two-phase system. The lack of a scientifically reasonable conceptualizing of wave propagation in a multiphase material such as soil leads to uncertainty in determining soil behavior. The stiffness of soils depends on the interaction of the different phases (i.e., particles, air and water phases). Drying or wetting of soil changes its fabric, and thus its shear stiffness and the wave propagation within. Monitoring such a fabric change can give a more in-depth comprehending of dynamic and static soil behavior in practical applications. Dealing with soils that are subjected to change in water content requires knowledge of unsaturated soils in many engineering applications such as construction and operating of dams, slopes, stability of vertical excavations, lateral earth pressure and bearing capacity of shallow foundations. A predictive model of shear wave velocity in unsaturated conditions can provide a valuable tool to researchers and engineers to assess soil behavior.

Monitoring fabric changing processes in sand is not only important for its direct engineering application but also because it offers an insightful conception of fundamental soil particles interaction at the micro scale that provides a prediction of macro scale behavior.

1.2 Objectives and scopes

The objective of the research is the investigation of the complex behavior of the soil parameters, initial shear stiffness and shear wave velocity, under consideration of multiphase conditions and time effect. This was achieved by monitoring the processes that take place with changing state variables or time and describing them mathematically. For the process monitoring, a powerful emerging tool, the *Coda Wave Interferometry*, was utilized to detect the slightest fabric change in a medium.

The testing program consists of two series of tests; creep series and unsaturated series. The former is designed to investigate creep phenomenon with different water contents, while the latter aims to examine wave propagation with different matric suctions. A special experimental system was produced to control pore water pressure and pore air pressure separately. The objectives of this research are as follows:

- Constructing a testing system that allows controlling confining pressure, pore water pressure and pore air pressure separately, in addition to exciting and receiving signals using bender elements.
- Examining the accuracy and robustness of the coda wave interferometry method in the presence of noise and verifying the possibility of acquiring stable, accurate results.
- Investigating the creep phenomenon in Hostun sand using coda wave interferometry to monitor the subtle fabric changes. The increment of velocity or stiffness is to be described mathematically. The model should predict the effect of time under consideration of granular material, such as interparticle friction, angularity, particle parameters and packing.
- Developing a micromechanical approach to calculate the granular properties needed in the model that applies to other granular materials.
- Investigating the effect of water content on creep in sand and presenting an explanation at the micro scale for any effect found.
- Investigating fabric change in unsaturated soils due to changes in matric suction using the coda wave interferometry.

- Proposing a predictive relationship between shear wave velocity and suction. Associating this relationship with other soil properties is essential from a practical point of view.

1.3 Organization of the dissertation

An introduction to the importance of creep phenomenon, small strain shear stiffness and unsaturated soils is presented in Chapter 2. In this chapter, a literature review is discussed, and unsolved problems are highlighted.

Chapter 3 presents the properties of the material tested in this research. The experimental system specifically constructed for testing soils under creep and unsaturated conditions is described in detail. Specimen preparation and test procedure under different initial conditions are presented as well.

The principle of the coda wave interferometry is explained in Chapter 4. A description of techniques to calculate the interferometry and a discussion of their validity and limitations are presented. A comparison among these techniques is carried out, in which their accuracy and robustness in the presence of noise are analyzed.

Chapter 5 discusses the theoretical background of modeling at the contact level. The significance of the effects of friction, angularity and coordination number is demonstrated. The objective of this chapter is to lay the theoretical ground for the discussion and modeling in the next chapter.

Chapter 6 presents the results of a series of creep tests done on specimens of Hostun sand with six different water contents. Coda wave interferometry is utilized to detect small changes in soil fabric during pressure and creep. A model was developed to describe these experimental data. This model includes the effect of friction, angularity and packing (coordination number), in addition to time. Values for those parameters are explicitly determined for Hostun sand with an approach that is generally applicable to other sands. A micromechanical approach is considered in discussing the findings.

Chapter 7 presents the results of a series of unsaturated tests. The effect of matric suction is investigated. Coda wave interferometry is successfully used here as well to detect minimal changes in shear wave velocity. Two approaches were developed to predict the change in shear wave velocity with matric suction or degree of saturation. A semi-empirical approach was considered in Section 7.4 to derive two models to predict shear wave velocity from the soil-water characteristic curve (SWCC). The models can be represented in terms of effective saturation, in terms of saturation or in terms of matric suction. In the case of the absence of SWCC and grain size distribution curve, more general models are proposed. A numerical approach was also developed relying on basic soil properties, namely grain size distribution and void ratio (Section 7.5). Predicting shear wave velocity without performing the time-consuming test to obtain SWCC can then be achieved by combining the analytical models from the semi-empirical approach and the numerical approach. Finally, validation of proposed models with data from this research and from previous studies is performed.

The conclusions of this research and recommendations for further studies are listed in Chapter 8.

Chapter 2

Literature Review

2.1 Introduction

In this chapter, the literature review of creep and initial small stiffness under multiphase conditions is discussed. An introduction to creep is presented in Section 2.2, and previous studies on creep in soils are discussed. Unanswered questions and missing gaps are highlighted. In Section 2.2.1 literature research on the pile setup phenomenon in sand, which is linked to creep, is examined, and practical implications for pile design are pointed out. The principle of shear stiffness at small strain is explained in Section 2.3. Bender elements method, which measures shear wave propagation in soil, and the principles of unsaturated soils are introduced. In Section 2.6, a literature review of existing knowledge about shear stiffness in unsaturated soils is presented. The review discusses the most commonly used models of shear modulus and points out the unsolved problems.

2.2 Creep

Creep in soil causes changes in mechanical properties in the long term and is usually divided into three phases, as shown in Figure 2.1. In the first phase, the primary one, the creep rate decreases with time. Then it becomes constant with time in the secondary phase. In the last phase, the tertiary one, creep rate increases leading to creep rupture. Some materials barely show any tertiary or even secondary phase. It is nowadays well excepted that an increase in the stress level results in an increase in the creep rate [Mitchell & Soga, 2005]. This means

that the rate of creep strain is a function of stress and time, i.e., $\dot{\epsilon} = F(\sigma, t)$, where $\dot{\epsilon}$ is creep strain rate, σ is stress level and t is time. The relationship is expressed in the following so-called time hardening formulation [Kraus, 1980]:

$$\dot{\epsilon} = A\sigma^{\alpha}t^{\beta} \tag{2.1}$$

where A, α and β are constants. In this formulation, A has a unit that is linked to α and β. To avoid having changeable units for A, reference stress and time are introduced:

$$\dot{\epsilon} = A\left(\frac{\sigma}{\sigma_{ref}}\right)^{\alpha}\left(\frac{t_{ref}}{t}\right)^{\beta} \tag{2.2}$$

where $\sigma_{ref} = 1\ kPa$ and $t_{ref} = 1\ min$. Integrating this formulation with respect to time gives strain as a function of stress and time (so-called Bailey-Norton law). These formulations are intended to model only primary and secondary creep, while tertiary creep that includes rupture is modeled differently.

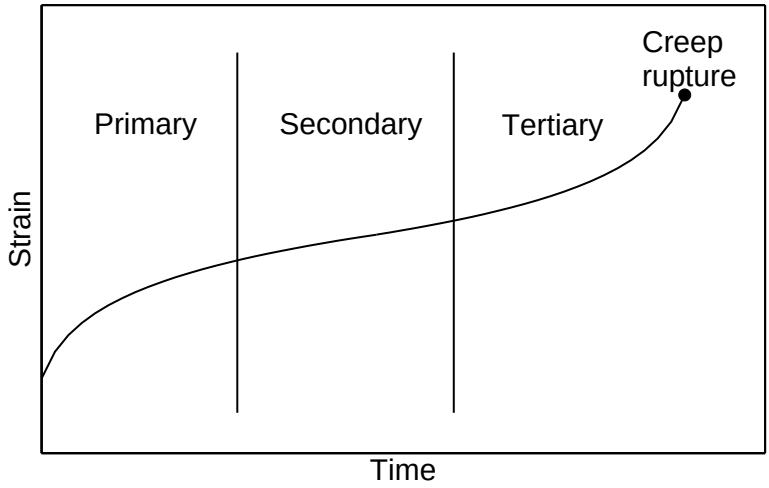

Figure 2.1: Primary, secondary and tertiary phases of creep

Creep is well studied in cohesive soils. In his extensive literature review of aging of soils, Schmertmann [1991] demonstrated experimental data and discussed previous studies that show an increase in preconsolidation stress in soil due to the aging effect. Small strain modulus increases with aging as well. Stokoe & Richart [1973] reported a significant time effect in laboratory tests on cohesive soils. They experimentally showed that shear wave velocity increased with time under constant confining pressure using resonant column. The increase in velocity was greater for finer soils. Schmertmann [1991] also reported an increase in

the one-dimensional compression modulus with aging for compacted fills.

Fox et al. [1992] investigated the creep settlements in peats. Their long-duration oedometer tests showed that the majority of total settlements were creep settlements. Creep plays an important role in increasing capacity in driven piles as well. The perturbed soil surrounding the pile exhibits aging leading to gain in pile strength [Schmertmann, 1991]. Karlsrud et al. [2014] examined the effect of time on the axial bearing capacity of driven steel piles. The piles were loaded to failure in different waiting periods (up to 24 months) after driving. They concluded that aging could result in a significant gain in pile capacity with time. Previously, Jensen et al. [2004] also studied the influence of time on the ultimate bearing capacity of axially loaded piles. They proposed a relationship to account for the time effect in pile design.

Afifi & Richart [1973] studied the effect of time on the small strain shear modulus through resonant column tests. They found that shear modulus increased with time for different types of fine soils under constant confining pressure. This increase was larger for finer soils. Schmertmann [1991] also reported an aging effect on the small strain shear modulus in the field.

In geotechnical practice, settlements and strength of driven piles are two examples, among others, of the importance of creep. Creep causes long term settlements of foundations, and thus compromises the safety of building founded on these foundations. The strength of piles increases with time, but it is not appropriately considered in the current pile designs. This results in a too conservative design. Most literature focused on the significance of creep in fine materials. Less attention was paid to aging effects in sands, despite that studies have shown that sand also exhibits creep phenomenon. Creep in sand is responsible for increasing in settlements, resistance in cone penetration test and standard penetration test, capacity for driven piles and small strain shear modulus. Understanding these effects has engineering applications and economical benefits.

The aging effect in clean sand was reported by Schmertmann [1991]. He also drew attention to the fact that cone penetration test (CPT) and standard penetration test (SPT) resistances increase with time for clean sand. He stated that aging is also present in shear strength for gravels and in the high strain range.

Karlsrud et al. [2014] proved that there is a significant gain in shaft friction on driven piles in sand. They found that the capacity increased by a factor of two within two years after pile installation. Daramola [1980] gave evidence that aging occurs in saturated sands. Wang et al. [2008] numerically simulated aging in dry, clean sand. They found that creep significantly alters the contact force distribution. The force chains get homogenized during creep that leads to more stable force chains, which in return are demonstrated by an increase in shear modulus and strength. Wang & Tsui [2009] investigated the aging effect on sand using resonant column under different conditions. They found that small strain shear modulus increased with time while damping continuously decreased. By adding kaolinite to sand, a gain in the aging rate was observed. Dai et al. [2013] proved that sand shows an aging effect even in a short period of time. They used coda wave interferometry to detect creep in sand and found that velocity is a power function of time. Baxter [1999] performed an experimental study on the aging of sand. He carried out bender elements measurements on a carbonate beach sand, which contains trace amounts of shells and organic, and a quartz sand inside a rigid wall cell. He found that for the carbonate sand saturation increased the creep rate, while for the quartz sand, the dry specimen had a higher rate. In four of the tests, a negative creep rate (decrease in stiffness) was observed in quartz sand in contrary to previous literature. He hypothesized that the cell walls might have expanded during the test, causing the erroneous results. Cone penetration tests were performed on the dry specimens at the beginning of aging. Baxter [1999] acknowledged that these tests significantly altered the received signals of the bender elements, which made interpretation of shear wave velocity development difficult. He recommended viewing the corresponding data of dry specimens with caution. With no consistent trend in his data, the results were not conclusive.

Lade et al. [2009] highlighted the fact that clay and sand behave differently with respect to time. Augustesen et al. [2004] investigated the time-dependent behavior of different soils through one-dimensional and triaxial test conditions in addition to giving a literature review. They found that time-dependent phenomena are more pronounced in clay than sand and that clay and sand demonstrate different behaviors. While the stress-strain relationship in clay is very sensitive to the strain rate (isotach behavior), sand does not show any change in the stress-strain relationship for very different strain rates (nonisotach behavior). This has

been also confirmed by other researchers (e.g., Lade et al. [2009] and Lade [2009]).

Most research published on creep in sand was carried out by means of strain measurements. Measuring velocity change during creep is substantially more sensitive to change in the soil fabric. Such change can occur with a minute change in the porosity of the specimen. Any change in porosity cannot be solely responsible for the increase in stiffness, as argued by Leonards & Altschaeffl [1964]. Much more change in the soil fabric takes place with very little change in volume. Evidence for such fabric change can be found in [Wang et al., 2008] and [Wang et al., 2016]. This means that merely measuring strain is not a sensitive method to monitor creep. Rather, wave measurements, combined with suitable signal processing, present a better tool to monitor slight changes in soil fabric, and thus detecting creep.

Creep in sand can be very subtle. Traditional methods to obtain wave velocity are not sensitive enough to detect these slight changes in sand fabric. Therefore, a better, more sensitive signal processing method is needed.

The effect of water content in sand on the creep phenomenon is not clear. The testing program for the creep tests of this work is designed to answer this question. A general relationship between wave velocity and time under consideration of granular material is still missing in the literature. The objective of this study is to establish a general model that includes time effect, in addition to other physical soil properties at the micro scale, such as interparticle friction, angularity, coordination number, pressure and grain properties.

2.2.1 Pile setup in sand

The increase of pile capacity for piles installed in clay is well acknowledged. This phenomenon is called pile setup and is partially attributed to the change in effective stress corresponding to pore pressure induced by pile driving. On the other hand, pile setup in sand is a less understood phenomenon, and it just got into research attention in the last two decades. This development of capacity exceeds the short time necessary for pore water pressure dissipation in cohesionless soils and is a result of the aging effect. Although the increase in pile capacity has been

proven by many researchers, the current design methods do not recognize it and a comprehensive knowledge of the role played by soil properties, pile properties and driving methods is still missing.

Chow et al. [1998] investigated pile behavior over time in dense marine sand. Static and dynamic load tests were performed on 4 open-ended pipe piles with a diameter of 32 cm and a length of 11 m and 22 m in a testing site in northern France. They found that the average friction resistance 5 years after the installation was 85 % and 72 % higher than their values 6 months after installation for the 11-m piles. For the 22-m piles, the shaft capacity appeared to have increased by 140 %. In their review of case histories, they indicated that shaft capacity increases by around 25 % to 75 % per log cycle of time in the medium to long term, while base resistance develops insignificantly. Corrosion was discussed to explain the mechanism of capacity increase. They found that shaft resistance increased in a way that does not match the corrosion areas on the pile shaft. Besides, previous studies in the literature show a similar increase for corroding and non-corroding materials, like steel, concrete and timber, installed above and below the water table. Therefore, they ruled out the corrosion explanation leaving creep in sand as the main mechanism.

Jardine et al. [2006] showed that the shaft capacity of piles driven in sand increases significantly with time after installation. They performed first-time static tests on steel pipe piles in dense sand. They found that aging initiates already only a few days after installation. In about 8 months, the shaft capacity increased to double its value a few days after installation. They suggested that standard design procedures usually meet pile capacity of about 10 days after installation and do not take into consideration the time effect. This points out the practical benefit of considering time effect in the case of piles loading at least a couple of months after installation.

A data review of 55 piles from the literature was carried out by Alawneh et al. [2009]. The data contain static and dynamic load tests on concrete and steel piles driven in sand soils with relative densities ranging from 35 % to 65 %. The piles were varying in material, length, diameter and initial capacity. They determined that pile capacity rose greatly with time. The gain was found to reach 300 % and may continue up to a time longer than 200 days. The long term setup cannot be

explained by the dissipation of excess pore water pressure, which is a process that takes a few minutes to a few hours in cohesionless soil. The toe resistance was found to be constant with time, while the shaft resistance was solely responsible for the gain in total pile capacity. The magnitude of setup in their database increased with increasing pile penetration depth and decreasing pile diameter, i.e., with increasing pile slenderness ratio.

The Norwegian Geotechnical Institute published a large study on the increase in axial bearing capacity of driven piles in sand and clay due to aging effects (Norwegian Geotechnical Institute [2014]). The study was also summarized by Karlsrud et al. [2014]. They carried out an extensive series of load tests at various time intervals over 2 years. The load tests were performed using a hydraulic cylinder mounted on a reaction frame attached to concrete strip foundations, as shown in Figure 2.2. The load was measured by means of a load cell. At each site, they had 6 piles, each 20 m in length, tested. The loads were increased in steps up to failure. The reference capacity was chosen to be at 10 days since most design methods consider pile capacity many days after installation. They found a significant increase in shaft capacity from 1.75 to 2.5 after 1 to 2 years compared to the capacity after 10 days for piles installed in sand. The denser sand had a larger increase in capacity. They suggested that driving the pile causes grain crushing of sand particles, which permits more fabric change over time. They theorized that creep in the sand surrounding the pile shaft could cause a large increase in effective stress, which is reflected in shaft friction.

Gavin et al. [2015] performed experiments on steel, concrete and timber driven piles in silica sand. They found that shaft capacity increases with time up to about one year. No difference could be found between onshore and offshore driven piles. Piles with applied, maintained tension loads throughout the aging period demonstrated less increase in capacity than piles with no loading.

There are fewer studies on jacked piles than driven piles. Lim & Lehane [2015] tried to fill this gap by testing 18 jacked piles in 3 sand sites. They monitored radial stress on the pile shafts and shaft friction for 72 days. In contrast to driven piles, the gain in capacity was found to be small. However, they found a significant capacity increase within the first day after installation. Site mineralogy, soil structure and groundwater caused scatter in the data. They suggested that the

Figure 2.2: Loading system setup used at test sites [Karlsrud et al., 2014]

major component of such a gain is the increase in shear stiffness and dilatation in the surrounding soil following pile installation.

As shown above, practical implications for pile design can be derived from a better understanding of creep in sand. As proposed by Chow et al. [1998], a waiting period can be considered before loading the piles to maximize the capacity. This way, larger loads can be permitted. Alternatively, the cost of pile production may be reduced if piles were installed early and allowed to age before loading.

2.3 Small strain shear stiffness

The shear stiffness, or shear modulus, is usually expressed as the secant modulus by the extreme points on the hysteresis loop [Seed et al., 1986], as shown in Figure 2.3. At low strain amplitudes, the shear modulus is high. It decreases as the strain amplitude increases. The figure demonstrates that shear modulus will depend on the amplitude of the strain. The locus of points corresponding to the tips of hysteresis loops of various cyclic strain amplitudes is called a *backbone curve* or *skeleton curve*. The slope in the origin point to this curve corresponds to the *maximum shear modulus* G_{max} or G_0, which is also called *initial shear*

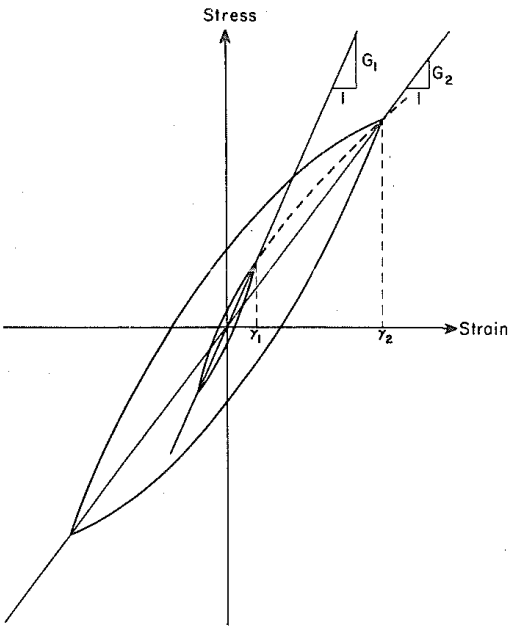

Figure 2.3: Hysteretic stress-strain relationship at different strain amplitudes after Seed et al. [1986]

modulus or *small strain shear stiffness*.

When the strain amplitude exceeds a certain threshold, the shear modulus starts to drop to a lower value, until it gets to a significantly smaller value at large strains. The variation of shear modulus with strain, represented as the modulus ratio G/G_{max}, defines the so-called *modulus reduction curve* shown in Figure 2.4. This threshold is called the *linear elastic threshold strain* and represents a boundary between two types of soil behavior. When the shear strain amplitude is smaller than this threshold, the following characteristics are explicit:

- the particles are not displaced with respect to each other, and thus there is essentially no permanent microstructural change.
- residual cyclic pore-water pressure does not essentially develop even for a saturated undrained case.
- the volume change is practically unchanged.

When this shear strain threshold is exceeded, the particles are permanently displaced with respect to each other, and thus the microstructure is altered irreversibly, and the soil stiffness changes permanently. The value of this threshold

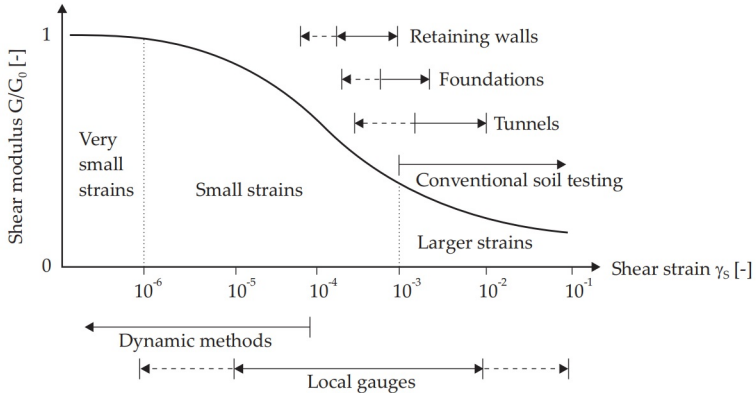

Figure 2.4: Modulus reduction curve of soil with typical strain ranges for laboratory tests and structures [Benz, 2007] (modified after Atkinson & Sallfors [1991]; Mair [1993])

varies according to plasticity and other factors and ranges between 10^{-3} % and 10^{-2} % [Hsu & Vucetic, 2004; Vucetic, 1994; Ishihara, 1996].

Figure 2.4 shows the reduction of stiffness with an increment of strain [Atkinson & Sallfors, 1991; Mair, 1993]. In general, it is expected that G_{max} does not change in the small strain range. The figure also illustrates typical strain ranges for structures and typical laboratory tests to measure different strains. Vibrations caused by seismic in situ tests, traffic, construction works, weak earthquakes or even blasting usually have shear strain amplitudes below $5x10^{-3}$ %.

Clayton [2011] verified the significance of using small strain shear stiffness in practical application by running a numerical experiment for estimating the ground deformations around a singly propped retaining wall. He also did a sensitivity analysis of predicting displacements and bending moments to different stiffness parameters. A propped cantilever wall was modeled using linear and nonlinear elasticity, and horizontal wall displacements, vertical displacements at original ground level, vertical displacements at excavation level, bending moments, and prop loads were calculated for different soil models. It was shown that stiffness at very small strain and the change of stiffness parameters with increasing strain had significant effects on computed displacements and wall bending moments. Predicted displacement patterns were sensitive to most parameters, including small strain stiffness and rate of stiffness degradation. He concluded

that small strain stiffness can be used to establish the stiffness profile, which has a great influence on displacement patterns around new and existing infrastructure. [Atkinson, 2000] discussed in detail the influence of nonlinearity of soil stiffness in geotechnical routine design. He analyzed the influence of nonlinearity on foundation behavior and on the choice of design stiffness. He concluded that soil stiffness parameters back-calculated from observed settlements of full-scale and model foundations are nonlinear and decay with settlements in the same way that stiffness decays with strain.

2.4 Measuring small strain shear stiffness

A variety of testing methods are available for measuring dynamic soil properties using field and laboratory techniques. Each of these methods has its own advantages and disadvantages. Choosing the right method needs careful attention and a good understanding of dynamic behavior, which depends on the type of problem. This understanding is necessary to realize the uncertainty in the measured data. Uncertainty can be originated by sampling disturbance, anisotropy, variability of soil, limitations of field or laboratory equipment, testing errors or interpretation errors [Kramer, 1996]. Therefore, effort must be paid to avoid these uncertainty sources or at least minimize them. Tests performed to obtain shear stiffness are categorized into two groups; in situ tests and laboratory tests.

In situ tests take into consideration the current state in the field. They do not need sampling, and some of them are not even invasive. The same tests measure properties corresponded to a large volume of soil. However, in situ tests assess soil properties of only the current state of soil with no possible control of the boundary conditions. Seismic tests require a thorough interpretation of recorded data, which may include background noise. Surface tests are non-invasive and measure a large volume of soil. In contrast, tests that require boreholes are more expensive but measure more specific soil properties with the possibility of taking samples for extra laboratory tests. The most common in situ tests are seismic reflection test, seismic refraction test, spectral analysis of surface waves (SASW), seismic downhole and seismic uphole test.

Several laboratory tests are performed in the range of small strain. They include local deformation transducers, resonant column test, piezoelectric bender element test and ultrasonic test. Details of the previous methods can be found in [Kramer, 1996]. The method used in this research is *Bender Elements*, which can excite and receive waves in a medium. Thus, wave velocity and corresponding small strain stiffness can be measured. The following section explains the principle of bender elements.

2.4.1 Bender elements

The bender element method is a simple technique to obtain the very small strain elastic shear modulus of soil G_{max} by measuring the propagation velocity of shear waves through a specimen by means of piezoelectric elements. The history of *piezoelectricity* dates back to 1880 when Pierre and Jacques Curie first discovered the piezoelectric effect in various substances, including Rochelle salt and quartz. Piezoelectric materials can generate an electric charge with the application of pressure; conversely, they can change physical dimensions with the application of an electric field (converse piezoelectricity). The word piezoelectricity comes from Greek; piezo means pressure in Greek, so the term (Piezoelectricity) means (electricity by pressure). In a piezoelectric material, ions can be moved more easily along some crystal axes than others. Pressure in certain directions results in a displacement of ions such that opposite faces of the crystal assume opposite charges. When pressure is released, the ions return to original positions.

Shirley [1978] first developed bender elements transducers to measure shear waves in the laboratory, using two ceramic piezoelectric elements fixed diametrically in a cylindrical specimen. Shirley & Hampton [1978] achieved further technical improvement using a transducer includes two piezoceramic plates rigidly bonded along their length. Schultheiss [1981] and Dyvik & Madshus [1985] initiated utilizing bender elements in conventional geotechnical apparatuses (e.g., triaxial, direct simple shear and oedometer devices). They introduced the experimental procedures and theoretical interpretation to carry out a bender elements test. In the 90s, the bender elements test got more attention. Therefore, sources of errors were sought, and the problem of signal interpretation arose [Viggiani & Atkinson, 1995; Jovičić et al., 1996].

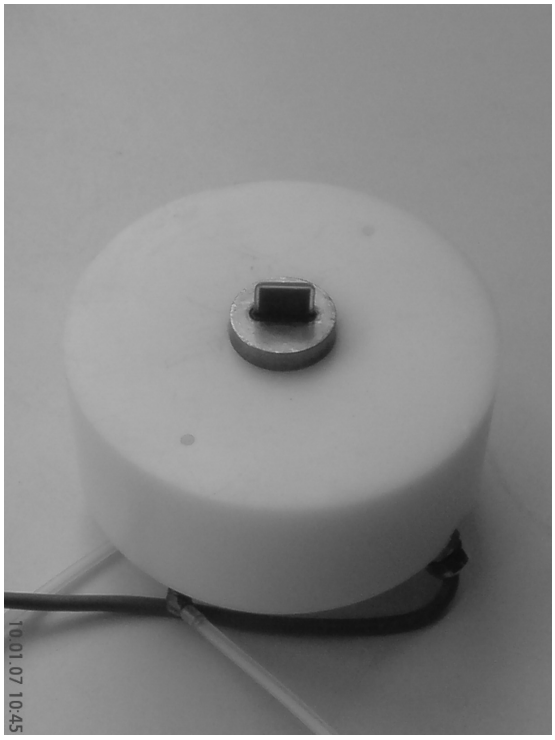

Figure 2.5: A bender element installed in a top cap of a triaxial cell

The bender elements technique was used to investigate the dependency of small strain shear stiffness G_{max} and shear wave velocity v_s on many parameters and factors such as grain size [Wichtmann & Triantafyllidis, 2009], confining pressure [Kuwano & Jardine, 2002; Asslan & Wuttke, 2010; Wuttke et al., 2012], stress path [Lee & Huang, 2007], time effect [Chang et al., 2006], anisotropy [Modoni et al., 1999; Pennington et al., 2001; Landon & DeGroot, 2006; Zeng & Grolewski, 2005; Piriyakul, 2006], Cementation [Pestana & Salvati, 2006] and unsaturated conditions [Cho & Santamarina, 2001; Takkabutr, 2006; Sawangsuriya et al., 2008]. The latter effect is discussed in detail in the following sections.

The bender elements technique has been getting more interest from researches due to its wide range of applicability. What made it attractive is that the computation of G_{max} is more direct than other methods like the resonant column test or in situ tests. Besides, bender elements are easy to install into most soil testing apparatus (e.g., triaxial test (Figure 2.5), shear test, resonant column test and oedometer test). The bender elements themselves are cheap, small and

lightweight, furthermore, they are non-destructive.

However, this method assumes one-dimensional wave propagation. Therefore, a plane wave is assumed to be propagated in the medium. In reality, the case is three-dimensional wave propagation from a not-perfect-point source, causing the near-field effect. Furthermore, the specimen has its boundaries. Therefore, there is reflection and interference of waves. Another hypothetical assumption is considering the material isotropic, uniform and continuum, which disregards travel path and dispersion. Sufficient contact should be between the bender elements and the surrounding soil to transmit the mechanical wave from the elements to the soil. If this was not the case, the received signal could be unclear and difficult to be analyzed, especially for soils with large particles. That is why it is better to have a minimum penetration in the soil relevant to the particles diameter. These disadvantages can be overcome by using advanced signal processing methods, applying appropriate theoretical models and sophisticated laboratory equipment, as discussed later.

2.5 Principles of unsaturated soils

Unsaturated soil is commonly viewed as a three-phase material. The most common equation for effective stress is the one proposed by Bishop [1959]:

$$\sigma' = (\sigma - u_a) + \chi(u_a - u_w) \tag{2.3}$$

where σ' is effective stress, σ is total pressure, u_a is pore air pressure, χ is a parameter related to the degree of saturation that varies between 0 for dry soil and 1 for fluid-saturated soil, and u_w is pore water pressure. This equation relates effective stress to two independent stress state variables, namely, $(\sigma - u_a)$, which is called *net normal stress* and $(u_a - u_w)$, which is called *matric suction*. These variables are independent of soil properties. Total suction in soil is defined as the free energy state of soil water [Edlefsen & Anderson, 1943]. It has two components; matric suction, which is the capillary component of free energy, and *osmotic suction* that is related to dissolved ions in solution. Thus, the total suction is given as:

$$\psi = (\sigma - u_a) + \pi \tag{2.4}$$

where ψ is total suction, $(\sigma - u_a)$ is matric suction and π is osmotic suction. The matric suction is mainly related to capillary force, while osmotic suction is more related to the diffuse double layer around clay particles . Osmotic suction is generally less important than matric suction and can be neglected [Fredlund & Rahardjo, 1993].

It was experimentally proven by Bishop & Donald [1961] that changing confining pressure, pore air pressure and pore water pressure in a way that keeps stress state variables $(\sigma - u_a)$ and $(u_a - u_w)$ constant has no effect on the stress-strain curve. These results supported the use of stress state variables in Equation 2.3.

Matric suction is applied using a high air entry disk, which works as a membrane between water and air. When the disk is saturated with water, it prevents air from penetrating through water due to the contractile skin. The difference between air and water pressure on both sides of the disk is, in definition, the matric suction.

2.6 Small strain shear stiffness in unsaturated soils

While many studies were done to establish a model to describe small strain shear stiffness, G_{max}, in the dry case, no consistent model was established for unsaturated soil. Most studies in the literature do not concern with small strain range. For this range, few models have been proposed to quantify G_{max} in unsaturated soil. These models rely on limited experimental data. In this section, experimental and theoretical investigations on small strain shear stiffness in unsaturated soils are presented and discussed.

Sawangsuriya [2006] and Sawangsuriya et al. [2008] studied three compacted subgrade soils at the as-compacted state, which is the initial compacted condition during construction. They experimentally investigated the dependence of G_{max} on matric suction, water content and dry unit weight. The shear wave velocity was measured using the bender elements method, while the matric suction was measured with the filter paper method. They concluded that matric suction has

a major effect on the stiffness of soil since it represents the combined effects of the forces holding the water in soil. In their tests, shear modulus increases as matric suction increases. Consequently, an empirical G_{max}-suction-water content relation was proposed. This model took into account the effect of compaction energy and water content as follows:

$$G_{max} = (w\xi\omega)(\alpha log\psi - \beta) \tag{2.5}$$

where G_{max} is small strain shear stiffness, w is water content, ξ is compaction energy ratio, which is defined as the ratio of compaction energy achieved by the enhanced or reduced Proctor effort to the compaction energy achieved by the standard Proctor effort, ω is the optimum water content ratio, which is the ratio of the optimum water content obtained from the enhanced or reduced Proctor effort to the optimum water content obtained from the standard Proctor effort, ψ is matric suction (osmotic suction was neglected) and α and β are fitting parameters.

They found that shear modulus increases as matric suction increases, as shown in Figure 2.6. The small strain shear stiffness increases significantly in the suction range for all compacting efforts: enhanced Proctor, standard Proctor and reduced Proctor. While it decreases substantially for the corresponding water content range (Figure 2.7). Normalized G_{max} with respect to water content, w, compaction energy ratio, ξ, and optimum water content ratio, ω, is shown in Figure 2.8 versus matric suction for a clayey sand.

They observed no trend between shear modulus and dry unit weight. This finding is in agreement with [Edil & Sawangsuriya, 2005]. Furthermore, the maximum shear modulus did not correspond to the maximum dry unit weight.

In a different study, Sawangsuriya et al. [2009] investigated the behavior of soil at small strain with changing suction for five compacted soils under net pressure of 35 kPa. The tests started as the specimens were saturated, then they were dried along the soil-water characteristic curve (SWCC). Along this drying path, soil suction increased and water content decreased. The shear wave could be measured with the means of bender elements. They proposed two empirical models to relate G_{max} with SWCC:

$$Model\ 1 : G_{max} = Af(e)(\sigma - u_a)^n + C\Theta^{\kappa}(u_a - u_w) \tag{2.6}$$

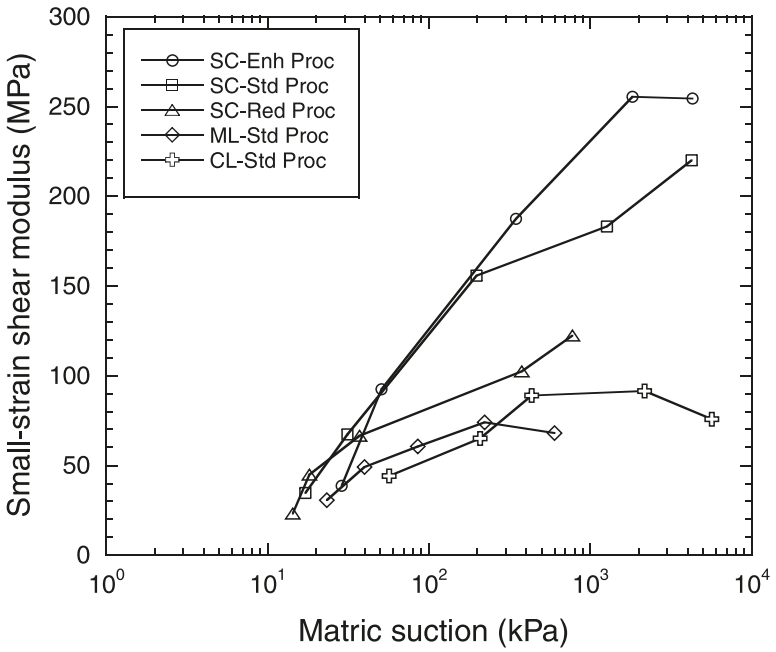

Figure 2.6: Small strain shear modulus versus matric suction for clayey sand (SC), lean clay (CL), and silt (ML) soils with different compaction efforts [Sawangsuriya et al., 2008]

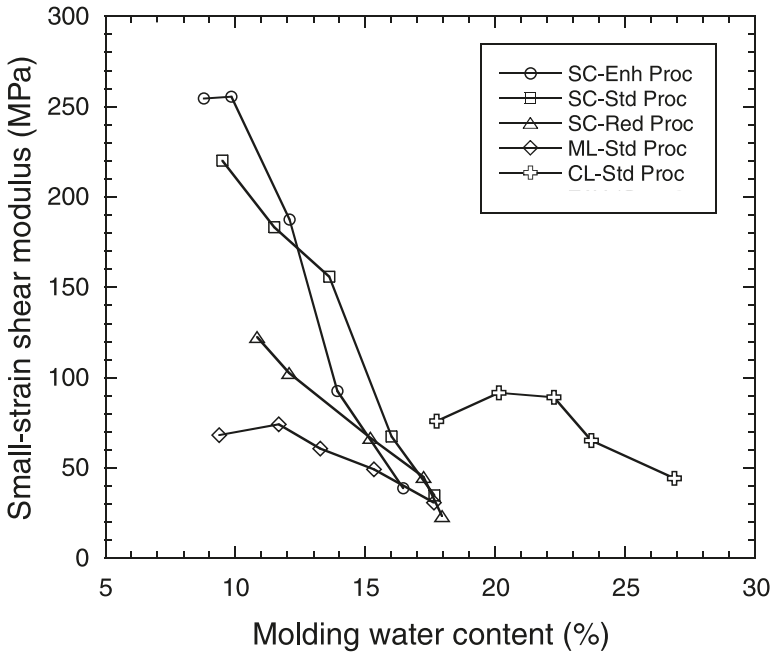

Figure 2.7: Small strain shear modulus versus initial molding water content for clayey sand (SC), lean clay (CL), and silt (ML) soils with different compaction efforts [Sawangsuriya et al., 2008]

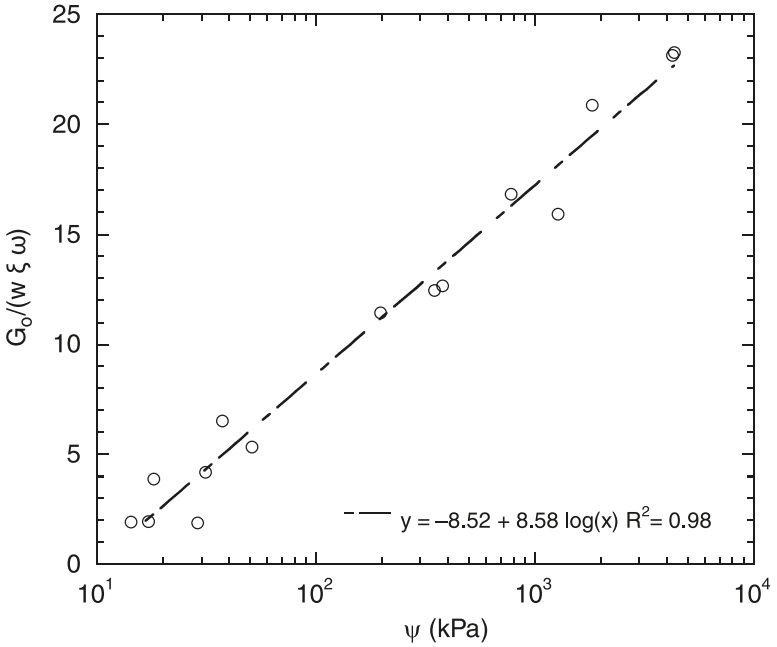

Figure 2.8: Normalized $G_{max}/(w\xi\omega)$ versus matric suction for clayey sand [Sawangsuriya et al., 2008]

$$Model\ 2 : G_{max} = Af(e)[(\sigma - u_a) + \Theta^{\kappa}(u_a - u_w)]^n \tag{2.7}$$

where A, C, κ and n are fitting parameters, $f(e) = 1/(0.3 + 0.7e^2)$ is a void ratio expression and Θ is the normalized volumetric water content. These proposed models depend on the SWCC to predict changes in soil behavior as water content decreases and soil suction increases along the drying path of the SWCC.

Figure 2.9 shows an increment of G_{max} with matric suction for clayey sand (SC) specimens compacted with standard Proctor energy as well as enhanced one and subjected to a net pressure of 35 kPa [Sawangsuriya et al., 2009]. The two curves are the fitted models to the experimental data. It was found that G_{max} increases as matric suction increases and water content decreases.

However, all tests in the previous study had a constant net pressure of 35 kPa. No predictions were made for other values of net confining pressure. Therefore, these models are restricted to this value.

Mancuso et al. [2002] studied small strain behavior of a silty sand in controlled-

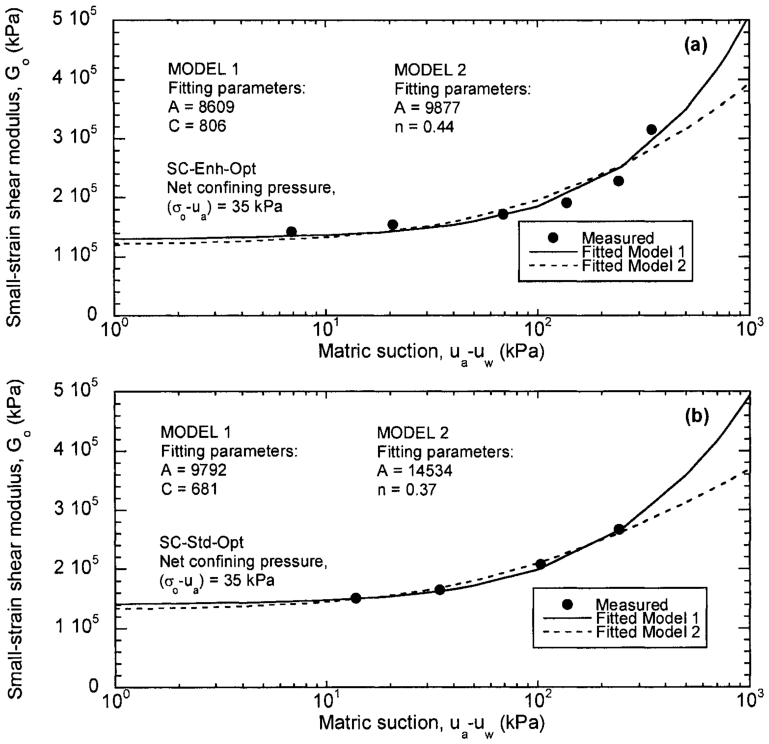

Figure 2.9: G_{max}-matric suction relationship for clayey sand compacted with standard Proctor energy (a) and enhanced one (b) [Sawangsuriya et al., 2009]

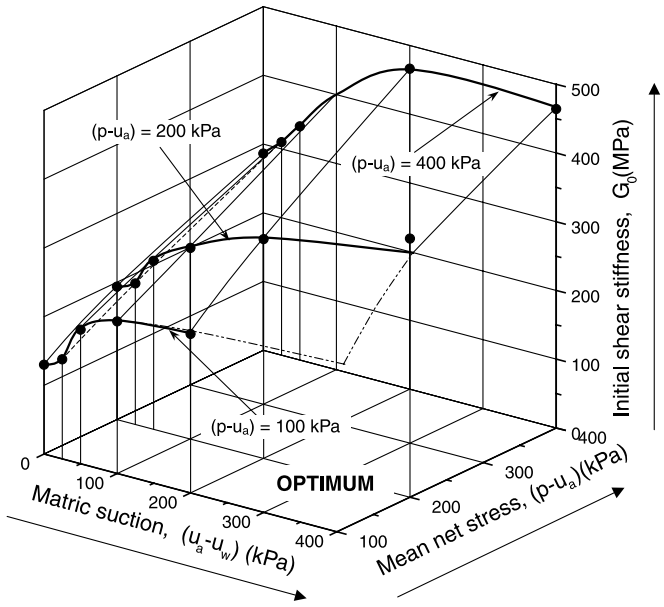

Figure 2.10: Small strain shear stiffness variation with matric suction in a controlled-suction resonant column for silty sand at optimum compaction [Mancuso et al., 2002]

suction resonant column and torsional shear tests. The tests were carried out in the suction range from 0 kPa to 400 kPa and mean net stresses of 100 kPa, 200 kPa, and 400 kPa. Figure 2.10 illustrates the variation of small strain shear stiffness with matric suction for a silty sand at different net stresses. Matric suction has a significant effect on G_{max} for all studied values of net stress. The figure indicates that shear modulus values measured at a constant mean net stress show an S-shaped increase with suction. Similar conclusions were found for wet of optimum compaction. Three zones can be distinguished in Figure 2.10: (1) zone 1 that starts at full saturation and limited to suction values lower than air entry value. In this zone, air is not a continuous phase thus bulk water dominates soil behavior; (2) zone 2 at intermediate suction values, where shear modulus increases more rapidly as suction increases and water menisci start to develop; (3) zone 3 at higher suction, where shear modulus tends toward a threshold value.

Most of the effects are detected for suctions ranging from 0 kPa to about 200 kPa, while for higher values, G_{max} tends toward a threshold that depends on the net stress level. They found a difference in shear modulus depending on molding water content, in a way that wet compaction induces a weaker fabric than optimum compaction. Figure 2.10 also indicates, as expected, that G_{max} increases with increasing net stress.

Alramahi et al. [2008] confirmed the increment of elastic moduli with increasing matric suction. They investigated elastic wave velocities for three soils under matric suction up to 100 kPa using compression and bender elements. The tests were done in a modified triaxial apparatus, in which p- and s-waves were measured as suction increases. The data indicated that shear wave velocity increases as matric suction increases following a semi empirical model:

$$v_s = \alpha(\frac{\sigma - u_a}{\sigma_{ref}})^{\beta} \left[1 + S\frac{u_a - u_w}{\sigma - u_a}\right]^{\beta_{unsat}} \tag{2.8}$$

where v_s is shear wave velocity, α, β and β_{unsat} are fitting parameters, σ is confining pressure, u_a is air pressure, σ_{ref}=1 kPa, S is the degree of saturation and u_w is water pressure.

Hoyos et al. [2008] and Takkabutr [2006] utilized resonant column and bender elements techniques to examine soil response of unsaturated soil at small strain.

G_{max} increased with increasing matric suction in the range of 0-110 kPa for confining pressure range of 7-35 kPa. They suggested that G_{max} depends only on confining pressure and matric suction of soil.

Picornell & Nazarian [1998] emphasized on the importance of soil suction on small strain stiffness. They observed an increase in stiffness with increasing soil suction using pressure plates to apply suction and bender elements to measure shear wave velocity. This increase was by a factor of 1.8 for sands, 2.5 for silt and 10 for clay. They attributed this significant effect of suction on shear modulus for clay to the deformation of flat particles under menisci forces resulting in an increase in several contact points where menisci can develop further.

However, there is no consensus regarding the continuous increase of G_{max} with soil suction. Many researchers found that the maximum value of G_{max} does not correspond to maximum matric suction. Marinho et al. [1995] indicated that G_{max} increased initially with increasing suction, then G_{max} keeps constant or slightly decreases with suction. Figure 2.11 shows the variation of G_{max} measured from bender elements test with soil suction for unsaturated soil. The figure indicates that small strain shear stiffness increases with suction up to a critical value, beyond which shear modulus decreases or stops increasing. Similar results can be found in [Yesiller et al., 2000]. They conducted tests on three compacted soils using ultrasonic waves. They found that maximum velocities occur at optimum water content, which corresponds to the maximum total density and minimum void ratio (Figure 2.12). Senthilmurugan & Ilamparuthi [2005] also achieved the same conclusion. In their intensive study, the p-wave velocity increases with water content up to optimum water content; then it decreases dramatically. This is valid irrespective of the compaction method and specimen size.

Nazarian & Yuan [2008] analyzed the variation of longitudinal soil wave velocity with water content using seismic non-destructive methods. They found that maximum modulus is obtained at a water content lower than the optimum one. Thus, maximum stiffness does not correspond to minimum water content, i.e., maximum suction. However, for clean sand, it does. This contradiction can be attributed to the change in density as water content changes, following the Proctor curve. Consequently, this density change affects soil stiffness substantially. While for clean sand, the Proctor curve is flatter and no significant change in

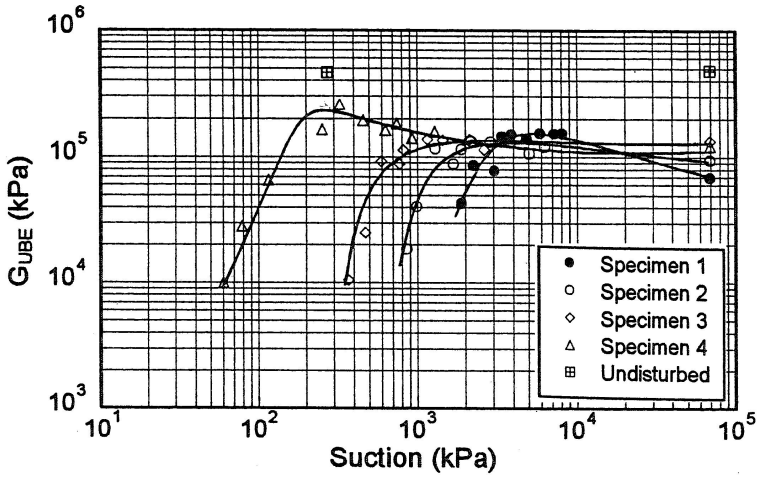

Figure 2.11: Variation of small strain shear stiffness of unsaturated soil using bender elements , G_{UBE}, with soil suction [Marinho et al., 1995]

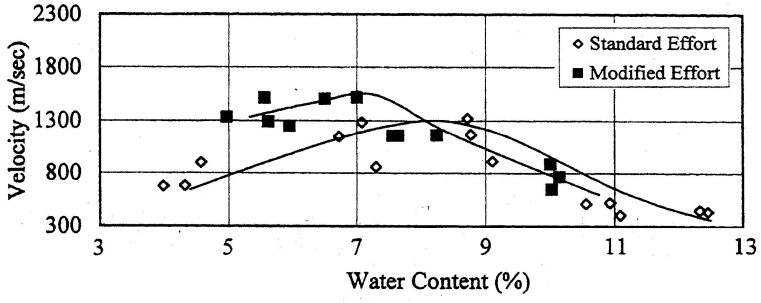

Figure 2.12: Variation of p-wave velocity with water content [Yesiller et al., 2000]

density is expected. This finding was also concluded by Weidinger et al. [2009], who stated that maximum shear wave velocity occurred at dry of optimum water content then decreased with increasing water content. They did not separate the effect of water content from the effect of dry density.

Table 2.1 summarizes the factors affecting elastic moduli in unsaturated soil in the literature. From the previous discussion, it can be concluded that the results in the literature are controversial as the table clarifies. Researchers used different techniques ranging from wave propagation to resonant column. Typically, data and the number of tests are very limited in unsaturated testing because the tests are very time consuming. This limitation of data restricted extending proposed models to other types of soil. Therefore, these models did not prove consistency for other materials.

For most of the studies in the literature, different specimens were prepared for the purpose of measuring stiffness. Matric suction was measured using different techniques for each specimen. Slightly different compaction energy may result in different soil fabric, especially when testing fine soil. Also, only specific values of matric suction were chosen, at which stiffness was measured. The low number of matric suction values does not permit to have a prediction of stiffness for the whole range of matric suction. For example, Sawangsuriya et al. [2009] measured shear modulus up to 600 kPa, while the SWCCs of tested soils extend up to 10^6 kPa. These problems are overcome in this research by controlling matric suction during the test, which allows measuring wave velocities along the SWCC for one specific specimen. The objective of this study is to measure velocity extensively, with small suction intervals, for the whole SWCC. This way, any established relationship between velocity and matric suction will be valid for the whole matric suction range.

The proposed models in the literature are based on empirical relationships. The model parameters are usually merely fitting parameters that have no physical meaning themselves and no connection to other properties. A correlation with other soil properties is essential from a practical point of view. Overall, a deeper understanding of the dynamic behavior of unsaturated soil is still missing.

Table 2.1: Factors affecting elastic moduli in unsaturated soil

Conclusion	*Reference*
Moduli increase with increasing suction, and maximum moduli are at maximum suction	[Sawangsuriya et al., 2008; Sawangsuriya, 2006; Sawangsuriya et al., 2009; Mancuso et al., 2002; Alramahi et al., 2008; Hoyos et al., 2008; Takkabutr, 2006; Picornell & Nazarian, 1998]
Maximum moduli are around optimum water content	[Marinho et al., 1995; Yesiller et al., 2000; Senthilmurugan & Ilamparuthi, 2005; Nazarian & Yuan, 2008; Weidinger et al., 2009]
Moduli increase with decreasing fine content and plasticity	[Dinesh et al., 2008; Yesiller et al., 2000; Senthilmurugan & Ilamparuthi, 2005; Inci et al., 2003]
Moduli increase with increasing confining pressure or increasing net stress	[Hoyos et al., 2008; Takkabutr, 2006; Dinesh et al., 2008; Mancuso et al., 2002]
Moduli increase with increasing compaction effort	[Sawangsuriya et al., 2008; Sawangsuriya, 2006; Sawangsuriya et al., 2009; Yesiller et al., 2000; Senthilmurugan & Ilamparuthi, 2005; Inci et al., 2003]

2.7 Summary

Creep in sand was considerably less studied in the literature than clay, despite the significant applications of understanding the time effect on sand. Most research on sand used strain measurements to detect volume change during creep, which is insensitive and not directly related to fabric change, where creep takes place on the particle level. Measurements of shear wave velocity offer a sensitive, non-destructive tool to monitor slight changes in soil fabric, and thus detecting creep in sand. No conclusive results in the literature were found on the effect of water content on creep in sand. Such an effect needs to be investigated. Examination of creep in sand is of valuable practical interest, especially for pile design. Taking creep into account for piles can lead to a considerably higher pile capacity or a reduction in costs. This study focuses on establishing a general model between wave velocity and time under consideration of granular material. Such a model should include, in addition to time effect, other physical soil properties at the micro scale, such as interparticle friction, angularity, coordination number, pressure and grain properties.

In this chapter, a literature review for measuring G_{max} in unsaturated soil was discussed. Different effects on G_{max} are summarized in Table 2.1. Controversial conclusions can be derived from the literature. The dependency of G_{max} on matric suction does not have consensus, and better understanding is needed at this point. A relationship of G_{max} for unsaturated soils is in the focus of this research. It is essential from a practical point of view to associate any proposed model with other soil properties.

Chapter 3

Experimental Setup

3.1 Introduction

This chapter presents the properties of the material tested in this research. The equipment explicitly adjusted for testing soils under creep and unsaturated conditions is described in detail in Section 3.3. Then, specimen preparation methods under different initial conditions are presented in Section 3.4. Tests of this research are categorized into creep series and unsaturated series of tests. Each series of tests has its procedure and boundary conditions, which are explained in Section 3.5. The objective of these tests is to investigate fabric change in soil under multiphase conditions.

3.2 Material properties

Two materials were used in this research, Hostun sand as a natural material and glass beads as an artificial material. Hostun sand was chosen because it is well known in the literature and easy comparison could be made when needed. Grain size distributions of material used are shown in Figure 3.1. As artificial material, uniform round glass beads was used with a diameter of 3.5 mm. The artificial material has a specific gravity of 2.5, which is very similar to sand. The advantage of using this artificial material is that the influence of confining pressure on shear wave velocity can be specified and isolated and the effect of angularity can be avoided as done in Chapter 6. Table 3.1 presents the physical properties of the material used in this research such as median grain size, D_{50}, uniformity

coefficient, C_u, in addition to minimum and maximum density and void ratio, specific gravity and classification according to the Unified Soil Classification System (USCS). For glass beads, no classification is available. Only the tested maximum density and the corresponding void ratio are available. Figure 3.2 shows the soil-water characteristic curve of Hostun sand used for the unsaturated series of tests [Alabdullah, 2010]. This curve is crucial for understanding the behavior of unsaturated soils.

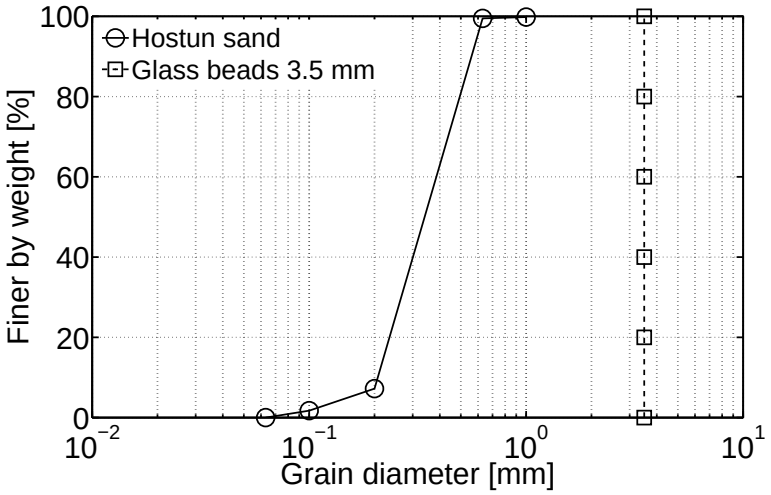

Figure 3.1: Sieve analysis of natural and artificial material used in this research

Table 3.1: Soil parameters of material used in this research

Property	*Hostun sand*	*Glass beads*
D_{50} $[mm]$	0.33	3.50
C_u $[-]$	1.81	1.00
Minimum density, ρ_{min} $[g/cm^3]$	1.36	-
Maximum density, ρ_{max} $[g/cm^3]$	1.61	1.55
Minimum void ratio, e_{min}	0.65	0.61
Maximum void ratio, e_{max}	0.95	-
Specific gravity, G_s	2.65	2.5
Classification (USCS)	SP	-

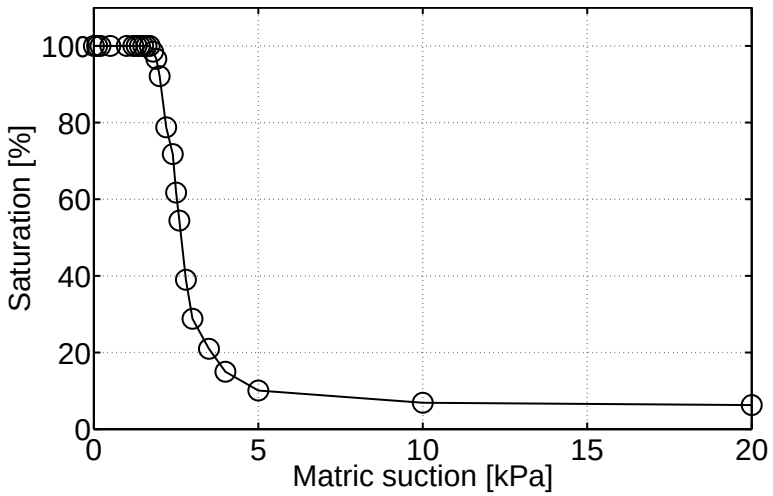

Figure 3.2: Soil-water characteristic curve of Hostun sand [Alabdullah, 2010]

3.3 Equipment

Hoyos & Macari [2001] developed a true triaxial cell with matric suction control. Silva et al. [2002] modified this cell to allow for bender elements measurements. The same cell was utilized again by Porras Ortiz [2004]. Sawangsuriya [2006] produced a similar cell to investigate unsaturated behavior using shear waves. It was noticed that pore water in these cells is applied on only one side of the specimen. That does not ensure homogenous distribution of water content within the specimen, especially at low water content, where the water phase is not a continuum. This problem is avoided here by applying pore water pressure at the top and bottom cap of the specimen. The equipment used in this study was modified specially to meet the purposes of performing the tests in this research. A triaxial cell was adjusted to enable controlling of unsaturated conditions and measuring wave velocity at the same time. A set of hardware and software was put together to carry out the experiments. The objective of this system is to allow controlling air pressure and water pressure separately; thus, controlling matric suction and net stress, as well as sending and recording waves in soil at the same time. The system is demonstrated in Figure 3.3 and Figure 3.4. The equipment used in this research contains the following parts:

- Pair of Piezoelectric *bender elements* installed in a triaxial cell, as shown in Figure 3.4 and Figure 3.5, to excite and receive shear waves. The bender elements had the following dimensions: length=14.2 mm, height (penetration into specimen)=10 mm, thickness=1.5 mm. The principle of bender

elements is explained in Section 2.4.1.

- Triaxial cell modified to contain bender elements shown in Figure 3.5. The bender elements are installed in the base and cap of the cell. The cell is grounded to avoid cross-talk and isolated to minimize noise.
- Twin-burette volume change indicator, which is connected to the manual air pressure valve and the cell. The pressure can be applied through this burette, while the volume change of the cell water can be measured.
- Manual and a digital air pressure controller to control the pressure in the cell.
- Signal amplifier (M68D3) to amplify and to filter the output signal. This is a special amplifier for piezoelectric sensors with 3 amplifier channels and Adjustable low-pass and high-pass filter. In all tests, a 50 kHz-low-pass filter was used and a 1000x amplification.
- Data logger (NI USB-6251) from National Instruments to record data over time and transfer analogue signal (i.e., transducer signal) to a digital one and vice versa. It also sends the signal which excites the bender element. The National Instruments USB-6251 is a USB high-speed multifunction data acquisition (DAQ) module optimized for accuracy at fast sampling rates with 16 analogue inputs (1.25 MS/s sampling rate and 16 bits resolution) and 2 analogue outputs (2.8 MS/s sampling rate and 16 bits resolution).
- Personal computer with a LabVIEW program installed to control and save the input and output signals. LabVIEW is a platform and development environment for a visual programming language from National Instruments. The advantage of this program is, it allows the signal to be saved for further analysis and offers full control over signal excitation, i.e., to excite different wave forms, frequencies, amplitudes and sampling rates. A LabVIEW program was written, which sends a signal to the bender elements through the data logger in different wave forms and frequencies, and saves received signal.

Figure 3.5 shows the details of the unsaturated cell used in this research. The cell is a triaxial cell modified to apply suction and measure shear waves. Water pressure is applied through a 1-bar high air entry disk. This high air entry disk is a ceramic disk with uniform small pores. When the disk is saturated with water, the surface tension prevents air from passing through; thus, it works as a membrane between water and air. This situation holds until air pressure is strong enough to break the water surface. This occurs at an air pressure value called the air entry value (AEV). The difference between air pressure on one side of the disk and the water pressure on the other side is defined as *matric suction* [Fredlund & Rahardjo, 1993]. For the ceramic disks used in this cell, the air entry value is 1 bar. A pair of ceramic disks are installed in the top cap and bottom base of the cell to ensure homogeneity and to reduce the required time to apply a specific suction. Water pressure is applied to these disks through a burette, which is connected to a digital manometer to control the applied pressure. The burette, in this case, helps to measure specimen water volume change.

Air pressure, u_a, is applied through a porous stone in the top cap and the base of the cell. This porous stone is connected to air pressure through connection 2 in Figure 3.5, which is controlled by a manometer. Confining pressure, σ, is applied through connection 3 and also connected to air pressure through a burette and controlled by a manometer. The difference between confining pressure and air pressure is defined as *net stress*. A pair of bender elements are installed in the top cap and bottom base of the cell. There are cables going through the cap and the base to control the electrical signal from and to the bender elements . Cable 4 in Figure 3.5 transfers signal from the data logger to the bender element, which transforms it into mechanical energy and starts to excite shear waves. The other cable, 5, transfers received signal to an amplifier and then to a data logger. The data logger is connected to a computer in which the software LabVIEW controls the whole electrical system. The electrical system is demonstrated in Figure 3.4.

Figure 3.6 illustrates a photograph of the top cap of the unsaturated cell. A cavity is made in the cap and the base to fix bender elements inside. The electrical cable goes through a tunnel behind the cavity into cell water then to outside the cell. The cables are surrounded by o-rings at different points to prevent water from going along the cables. The top cap, as well as the bottom base, have two ceramic disks to increase water flow, a porous stone through which air pressure

is applied, and a bender element.

Figure 3.7 demonstrates an unsaturated specimen with the top cap and all tubes connected. Figure 3.8 illustrates a top view of the same specimen. Each ceramic disk has two tubes attached to it in order to circulate water beneath it so no air bubbles can be trapped there. A photograph of the whole system ready for the test is shown in Figure 3.3.

When applying pressure, the cell walls expand, producing more volume inside the cell. Accordingly, the false volume change is measured and might be incorrectly attributed to specimen volume change causing an error in the measurements. Besides pressure, there is also time-induced volume change [Head, 1986]. When pressure is applied to the cell for some time, the cell starts to creep. For the previous reasons, the cell and other equipment (e.g., burette) used in the tests were calibrated using a stainless steel dummy to correct the measurements. This calibration is implemented in the calculations of this research. The volume change for loading and unloading paths were compared. They showed the elastic behavior of the cell. Therefore, no change in cell behavior is expected due to loading-uploading cycles.

For the creep tests, the same system was used. The control of specimen water and air pressure was not needed since the specimen was tested in the as-compacted state. An open-system burette connected to the specimen was used. In the saturation condition, this burette can measure pore water volume change. This provides an extra possibility to measure the volume change during the test for a saturated specimen.

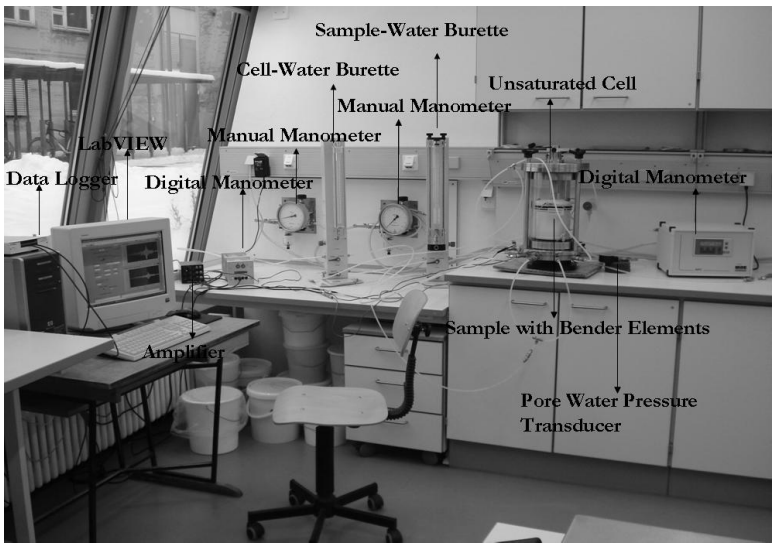

Figure 3.3: Photo of the laboratory system for unsaturated soil

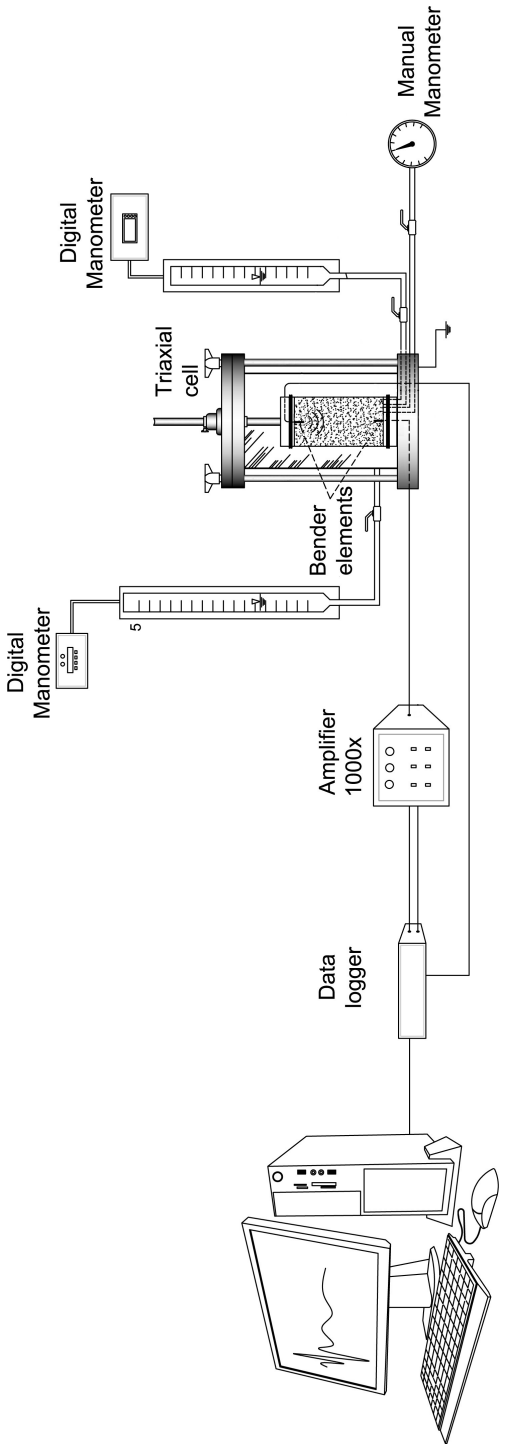

Figure 3.4: Laboratory system

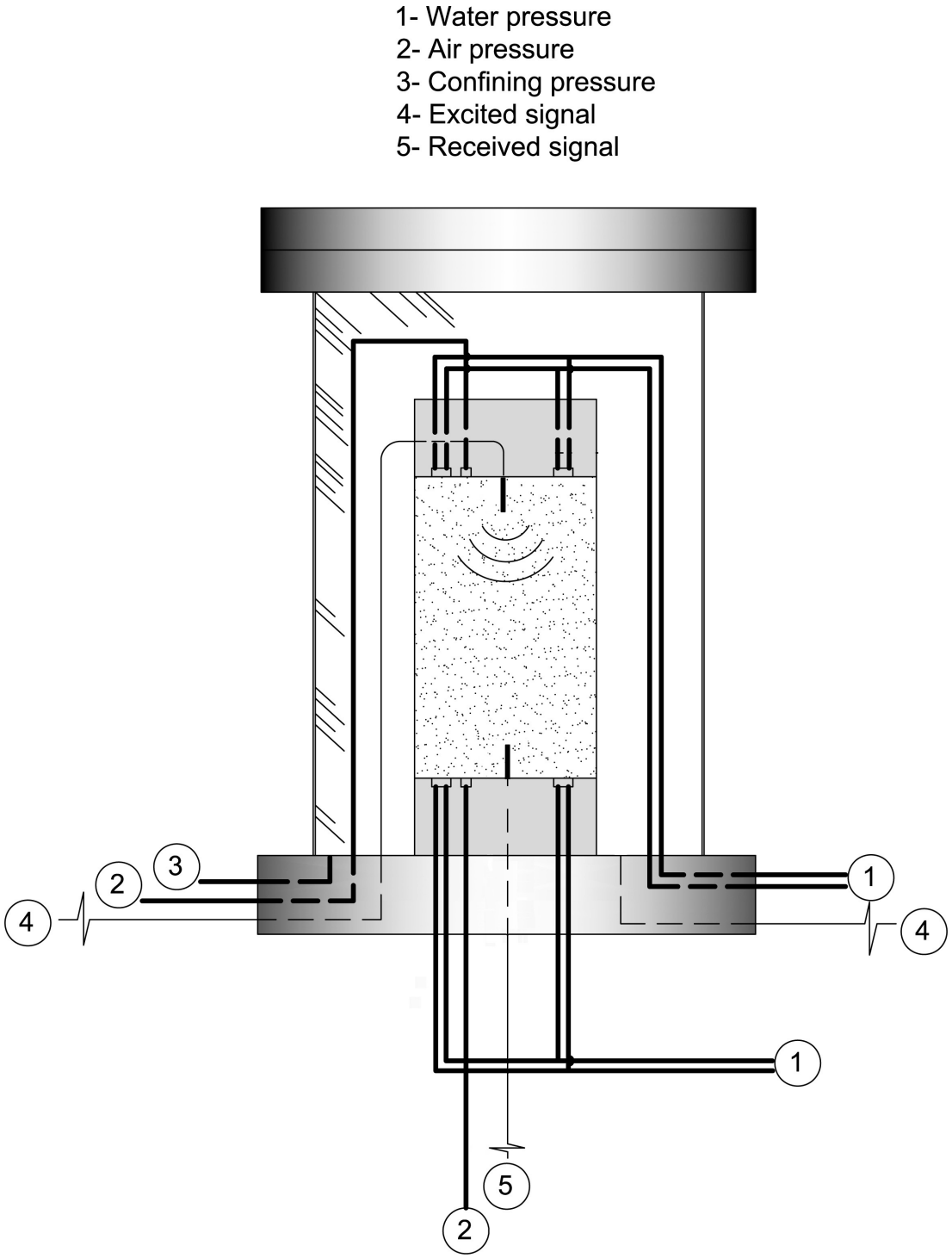

Figure 3.5: Details of the unsaturated cell

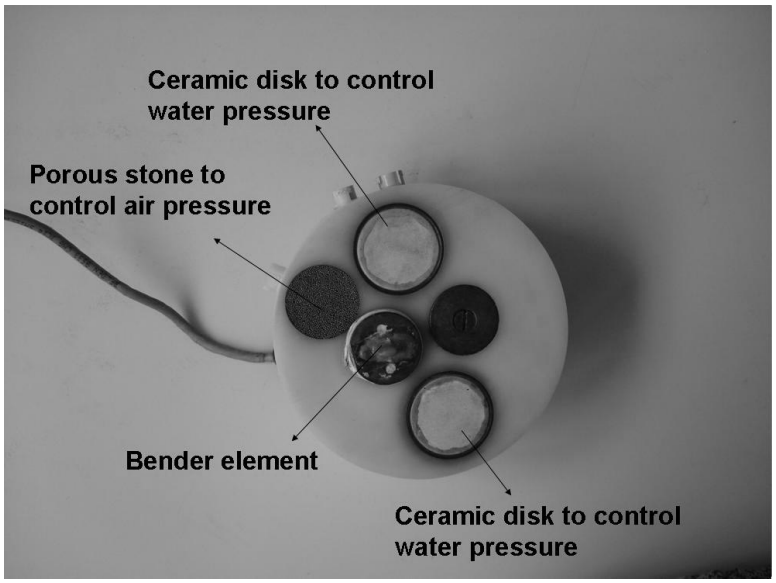

Figure 3.6: Photo of the top cap of the unsaturated cell

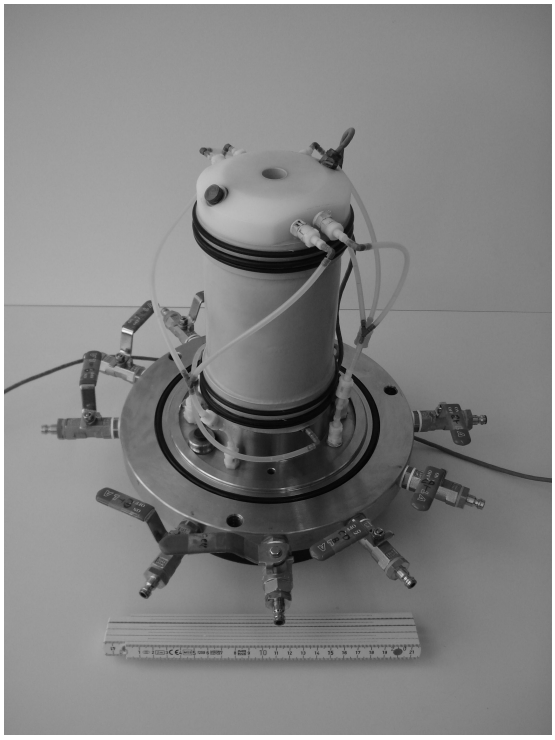

Figure 3.7: Specimen ready for test

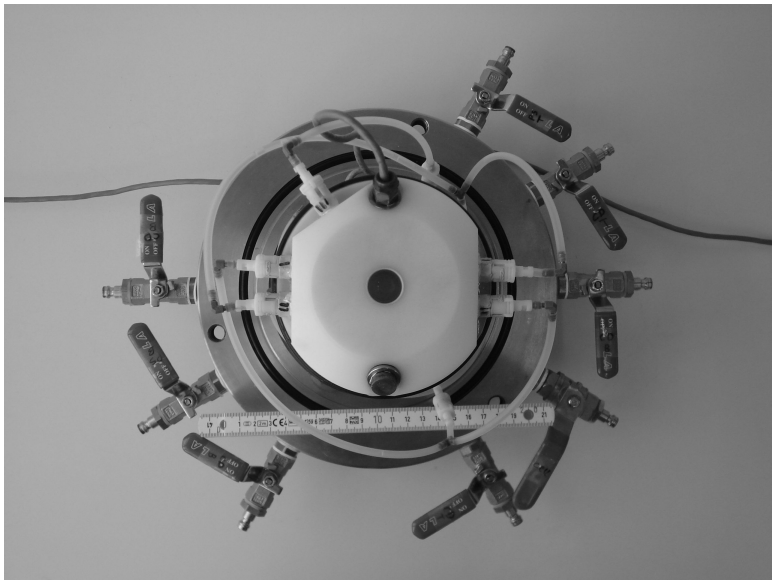

Figure 3.8: Top view of the specimen in Figure 3.7

3.4 Specimen preparation

For the unsaturated tests, specimens were prepared initially dry, then saturated with de-aired water before the test begins. A cylindrical split mold was used to give the right shape to the specimen. The split mold consists of two parts which can be separated from each other after building the specimen. A thin latex membrane (0.4 mm) is placed inside the mold and fixed at the cell base with at least two o-rings. The o-rings prevent water from getting inside the specimen. A vacuum is applied between the latex membrane and the metal mold. This way, the membrane stretches and ensures a perfect cylindrical shape.

A filter paper is placed on the bottom porous stone to prevent soil from getting inside the pores of the porous stone. Then, the oven-dried soil is pluviated into the mold and compacted in layers where specific volume and weight are controlled, as seen in Figure 3.9. The top cap is then set on top of the mold with filter paper, and the membrane is pulled around it, then fixed with o-rings. A small vacuum pressure 5-10 kPa is then applied inside the specimen; thereafter, the split mold can be removed since the specimen can hold standing alone, as seen in Figure 3.10. The cell frame is then installed and tightened by screws and filled with fresh de-aired water (see Figure 3.11).

Thereafter, the cell frame can be installed, and de-aired water fills the cell. Small confining pressure of 10 kPa is applied while the specimen vacuum is simultaneously released. Water is then allowed to run for a while through the specimen from bottom to top via the porous stones to push any air bubbles trapped inside. This method is most effective for soils of high permeability, such as sand. In order to ensure that soil is completely saturated, the back pressure method is utilized. In this method, pore water pressure inside the specimen is increased to force water to go among soil particles. In the meanwhile, cell pressure remains 10 kPa higher than back pressure (i.e., pore water pressure) in order to support the specimen. The following steps are carried out to ensure and verify saturation:

1. Cell pressure is increased from 10 kPa to 60 kPa with all valves of the specimen closed. The pore water pressure inside the specimen is measured by a pore water pressure transducer. This cell pressure increment causes an increment in the pore water pressure of Δu. This allows us to calculate the pore pressure coefficient or Skempton factor B as:

$$B = \frac{\Delta u}{\Delta \sigma} \tag{3.1}$$

   In the ideal case of 100 % saturation, B should be or close to 1.

2. Back pressure inside the specimen is increased to 50 kPa (i.e., 10 kPa less than cell pressure). This pressure pushes water into the specimen creating a higher saturation level.

3. Cell pressure is increased once more with all other valves closed. The last two steps are repeated, and Skempton factor B is calculated for each step.

For stiff and very stiff soil, it is not possible to achieve a B-value of 1 [Head, 1986]. A better saturation criterion, in this case, is to have the same B-value at two successive back pressure steps. This is the criterion used in this research. The back pressure used was up to 400 kPa.

After this saturation process, both cell and back pressure were reduced back to the initial situation of cell pressure 10 kPa and pore water pressure 0 kPa. This process does not affect the stress state of the specimen since the effective

stress is always constant at 10 kPa.

For the creep series of tests, dry and wet specimens were prepared following the preparation of the dry specimen explained above. The saturated specimen was prepared exactly as the saturated one for unsaturated tests, i.e., initially dry, then saturated using the Skempton method.

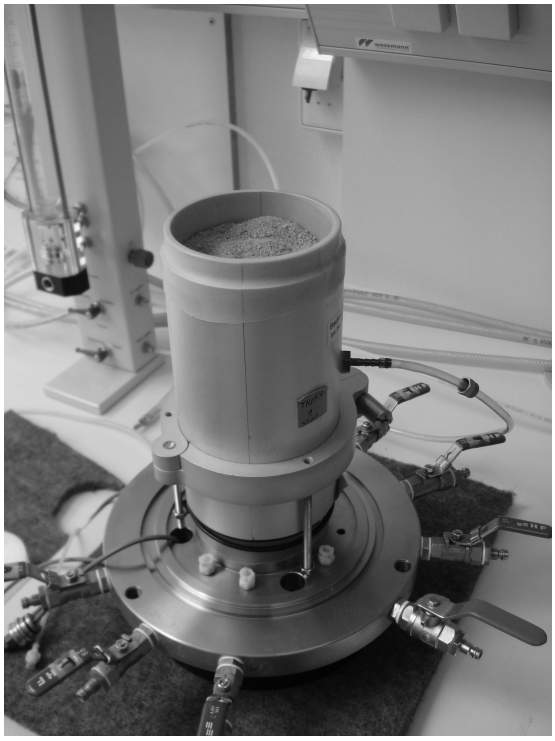

Figure 3.9: Specimen during sand pluviation and compaction

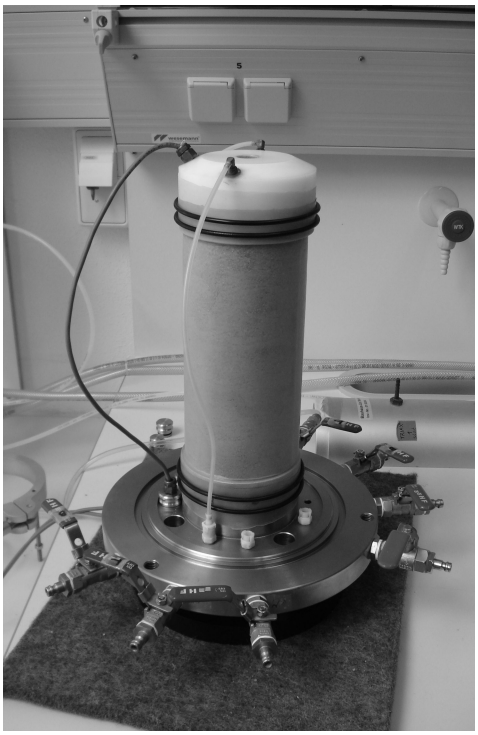

Figure 3.10: Specimen after removing the mold

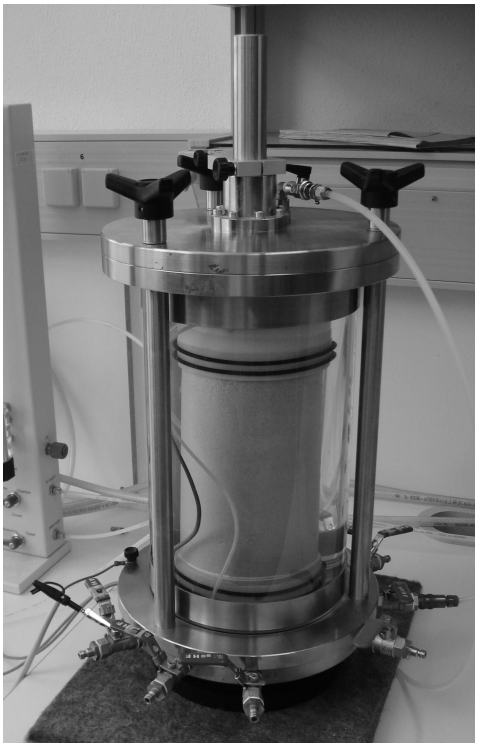

Figure 3.11: Cell ready for a test

3.5 Experimental procedures

3.5.1 Test procedure for creep series

The cell used for the creep tests is the unsaturated test cell described in Section 3.3. Specimen perpetration for dry, wet and saturated material was done following the procedure described in Section 3.4. Pore water pressure and pore air pressure were not controlled during the test; rather, an open system burette was connected to the specimen, and these pressures were kept at 0 kPa. Specimens were 11 cm in height and 10 cm in diameter. Different saturation levels ranging from 0 to 100 % were tested in this series in order to detect the water content effect on the creep process. Initial conditions are listed in Table 3.2.

The specimens were subjected to small increments in confining pressure of 2 kPa. Confining pressure increased from 10 kPa to 80 kPa in about 1 hour. Afterward, the final confining pressure, 80 kPa, was held for 8 hours. In this phase, the creep process was monitored. Finally, confining pressure was decreased back to 10 kPa in 2 kPa decrement steps, as illustrated in Figure 3.12. In the loading and unloading phases, shear wave measurements were taken at each pressure step. In the creep phase, measurements were taken every 30 minutes.

Table 3.2: Experimental program for creep series of tests

Saturation level, S [%]	*Water content, w* [%]	*Void ratio, e*	*Dry density,* ρ $[g/cm^3]$
0	0	0.65	1.61
19.7	5.6	0.75	1.51
33.9	9.6	0.75	1.51
56.3	14.6	0.69	1.57
80.5	20.1	0.69	1.56
100	24.9	0.66	1.61

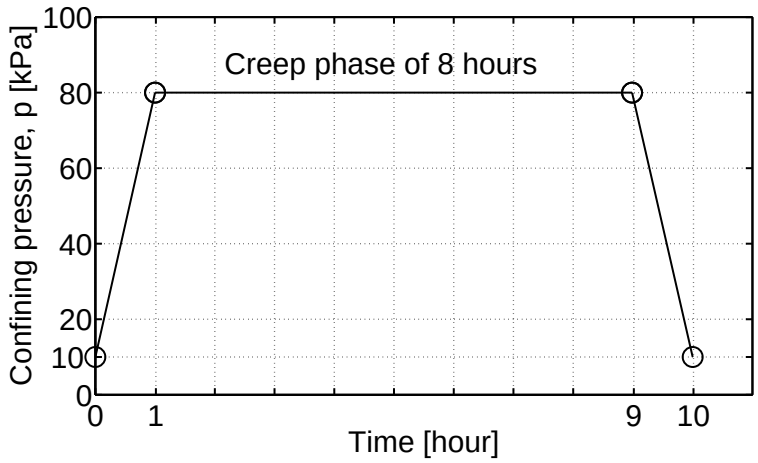

Figure 3.12: Test procedure for the creep series of tests

3.5.2 Test procedure for unsaturated series

Before starting the test, all ceramic disks and tubes had to be completely saturated with water without any air bubbles. The channels beneath the ceramic disks must be fully saturated. This was done by allowing de-aired water to run through these tubes in the flushing system (Figure 3.5). The ceramic disks themselves must also be saturated. This was achieved by allowing water to run into the specimen through the porous stone using connection 2 in Figure 3.5 and applying a vacuum through ceramic disks using connection 1 in Figure 3.5.

For each unsaturated test, the net stress $(\sigma - u_a)$ was kept constant, while matric suction $(u_a - u_w)$ increased following the drying path of the SWCC. For sand specimens, two net stress values were applied, 50 kPa and 100 kPa. The test starts with a saturated specimen; then, water pressure was decreased gradually while air pressure and confining pressure were maintained. Thus, matric suction increased from 0 kPa to 20 kPa. This method is called *Axis-Translation Technique* [Hilf, 1956]. When $u_a = 1$ bar, then matric suction $(u_a - u_w)$ is equal to the absolute value of the negative pore water pressure. Consequently, when the pore water pressure becomes highly negative, air bubbles are formed inside water, and they fill the measuring system in a phenomenon called *Cavitation*. The axis-translation technique is a commonly-used method to avoid this problem. It transfers the reference of water pressure from atmospheric pressure to air pressure. Accordingly, water pressure does not become negative. In this technique,

the pore water pressure is increased to the value of the new reference, the pore air pressure. Applying matric suction $(u_a - u_w)$ is achieved by decreasing the pore water pressure by a value equal to the desired matric suction. The matric suction does not depend on the value of pore air pressure; rather, it depends only on the difference between pore air pressure and pore water pressure [Fredlund & Rahardjo, 1993; Hilf, 1956]. Since the pore water pressure remains positive, the problem of cavitation is avoided.

For the first test in Table 3.3, the initial conditions were: confining pressure is 200 kPa, air pressure is 100 kPa and water pressure is 100 kPa. Then to apply matric suction values, water pressure was gradually decreased from 100 kPa to 80 kPa in the values shown in Table 3.4. Similarly, the other test was conducted. In both tests, confining pressure was constant. This allows similar cell volume change to occur. Specimens were 11 cm in height and 10 cm in diameter.

At each suction step, shear wave measurement was taken. These matric suction steps were at 1, 2, 4, 6, 8, 10 and 20 kPa, as in Table 3.3. After applying each suction step, a period of time passed before equilibrium was reached. Equilibrium took a few days for most steps. In the meanwhile, wave measurements were recorded daily.

Table 3.3: Experimental program for unsaturated tests on Hostun sand

Net stress, $(\sigma - u_a)$ $[kPa]$	*Matric suction,* $(u_a - u_w)$ $[kPa]$
100	0, 1, 2, 4, 6, 8, 10, 20
50	0, 1, 2, 4, 6, 8, 10, 20

Table 3.4: Pressure values of confining pressure, σ, air pressure, u_a, and water pressure, u_w, throughout the unsaturated tests

σ $[kPa]$	u_a $[kPa]$	u_w $[kPa]$
200	100	100, 99, 98, 96, 94, 92, 90, 80
200	150	150, 149, 148, 146, 144, 142, 140, 130

3.6 Summary

The properties of used natural and artificial materials in this research were presented in this chapter. The utilized equipment was described in detail. This includes modifying a triaxial cell that enables controlling of confining pressure, water pressure and air pressure separately and measuring wave in unsaturated soils and with creep. This cell permits studying the evolution of shear wave velocity with a change in matric suction for unsaturated soils. Required specimen preparation and calibration were discussed. Tests in this research were divided into two groups, creep tests and unsaturated tests. Each one of them was directed to study the behavior of soil under specific conditions. For each series of tests, the experimental procedure was explained, and an experimental program with boundary conditions was presented.

Chapter 4

Evolution Monitoring by Coda Wave Analysis

4.1 Introduction

Coda Wave Interferometry (CWI) is a method for detecting small changes in a medium. The principle of the CWI is explained in the following sections. A description of existing techniques to calculate the interferometry and a discussion of their validity and limitations are presented in this chapter. An improved technique, the *Sliding Window Technique* that offers stable, accurate results, even in the presence of noise, is presented here. Finally, a comparison among these techniques is carried out, in which their accuracy and robustness are analyzed.

4.2 Principle of the coda wave interferometry

Coda wave interferometry is a method for monitoring changes in media over time using waves. It is a sensitive method to detect minor changes between two signals. Waves in soil encounter scattering due to heterogeneity in the medium. This results in wave trains that come after the main part of the wave, called *coda wave*, which means the tail of the wave. This part of the wave, the coda, travels through different paths in the medium and, when the medium is limited, also back and forth stacking more information. This results in a very sensitive time history that can detect any minor change in the travel path due to changes in the medium. The coda wave is extremely repeatable, i.e., if the same waveform

is excited between the same two points under the same conditions, both waves are identical. Whereas, any small change in the medium results in a change in the coda wave that can be detected in this method. A more detailed explanation about the principles of the coda wave interferometry can be found in [Snieder, 2004; Grêt et al., 2006b]. In the following sections, the *Doublet Technique*, the most common technique to calculate the interferometry in literature, and the *Stretch Technique* are explained. Furthermore, an improved technique, the *Sliding Window Technique*, is proposed.

4.3 Doublet technique

To estimate the change between two waves, before and after some perturbation, the time history is divided into non-overlapping windows, and cross correlation is applied to each window [Snieder, 2006; Grêt et al., 2006b]. The normalized time-shifted cross correlation coefficient is given by:

$$CC^{t_c,t_w}(\delta t) = \frac{\int_{t_c-t_w}^{t_c+t_w} u_{unp}(t)u_{per}(t+\delta t)dt}{\sqrt{\int_{t_c-t_w}^{t_c+t_w} u_{unp}^2(t)dt \int_{t_c-t_w}^{t_c+t_w} u_{per}^2(t)dt}} \tag{4.1}$$

where time window is centered around time t_c and has a duration of $2t_w$, δt is the time shift of the perturbed waveform relative to the unperturbed waveform, u_{unp} is the unperturbed wave field, which is the summation of waves over all possible trajectories of the unperturbed medium, and u_{per} is the perturbed wave field. Accordingly, time shift δt that corresponds with the maximum correlation is detected for each window. The detected shift time should show a linear gradient over total time. Snieder [2006] explained theoretically how the time-shifted correlation coefficient could be used to estimate the mean and variance of the travel time perturbation caused by the perturbation of the medium.

The coda wave interferometry method was successfully used in the field of geophysics. Grêt et al. [2006b] analyzed the dependency of velocity on uniaxial stress, temperature and water saturation. Grêt et al. [2006a] applied coda wave interferometry to seismic waves excited by a hammer source in a mining environment. Snieder & Hagerty [2004] used the coda wave interferometry to monitor small changes in pressure in a volcano over a large scale.

Figure 4.1a shows two time histories measured between a source and a receiver from this research at two states; before and after a pressure increment of 5 kPa. The two rectangular windows *i* and *ii* indicate the main part of the wave (Figure 4.1b) and the coda wave (Figure 4.1c), respectively. It is obvious that both time histories coincide in the main wave (Figure 4.1b), while in Figure 4.1c, they are more distinguishable in the coda wave regarding the shift on the time axis. Since all interpretation methods that are available in the literature deal with the main wave, they is no possibility to detect such small perturbation in soil. In contrast, the coda wave interferometry method analyzes the later part of the wave, which travels more through the medium collecting more data. A visible shift of the time axis is illustrated in Figure 4.1c. This shift increases as window *ii* moves right along the time axis in Figure 4.1a. This time axis can be divided into segments in order to apply cross correlation between both time histories to each segment. Too many time windows will result in more time-consuming analysis, while the outcome of too few windows may be inaccurate. In this research, 7 to 10 time windows, each about 2 ms wide, were typically used.

A cross correlation between perturbed and unperturbed waves for a specific time window is demonstrated in Figure 4.2a. The maximum correlation and its time shift are determined using the *cross correlation method*. Time shifts for all time windows in Figure 4.1a are illustrated versus time in Figure 4.2b. The change in time shift along the axis of time history, i.e., the inclination θ, represents the change in velocity since the length is constant. This inclination intersects with the x-axis at the beginning of the waves, i.e., at about 2 ms in this example. Thus, by dividing the time shift over the central time of each window, one gets the velocity gradient $\delta v/v$ (Figure 4.2c). In this example, the mean velocity gradient was 2.2 % for a 5-kPa increment of confining pressure. The stacking of the acquired signal can improve the quality of the signal and, therefore, the accuracy of the coda wave interferometry. Stacking was used in this research whenever needed to improve the signal-to-noise ratio. By applying this analysis to further pressure increments, a velocity gradient over pressure steps can be monitored. This is valid for any perturbation in a medium besides pressure, such as water content, void ratio, aging and temperature. The minimum perturbation which can be detected using this technique is a question of signal quality, i.e., receivers sensitivity and system quality.

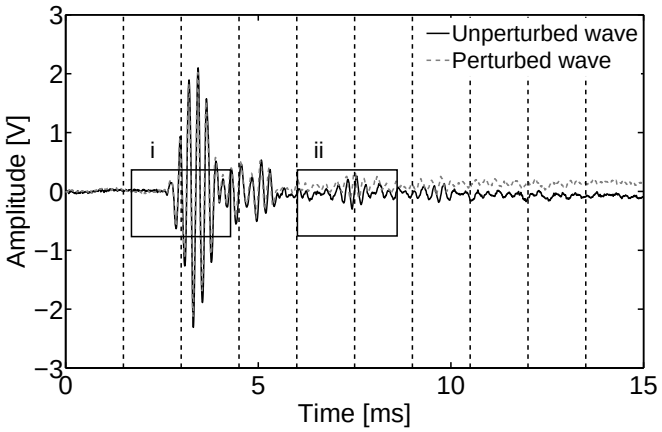

(a) Time histories of perturbed and unperturbed waves

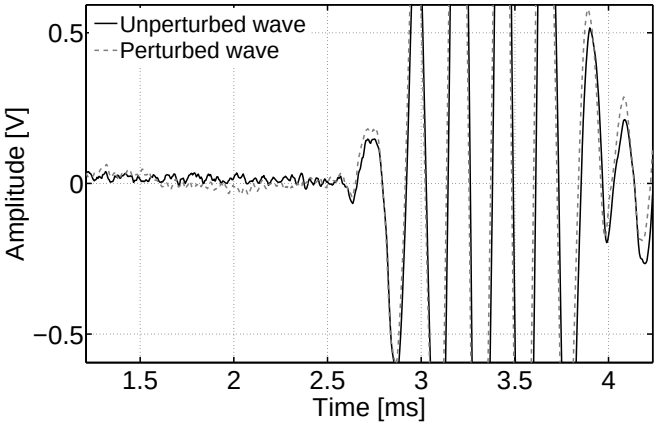

(b) Both time histories in window i in the main wave

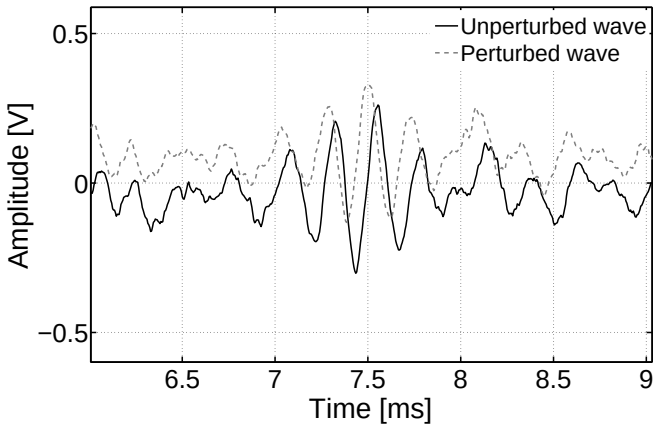

(c) Both time histories in window ii in the coda wave

Figure 4.1: Time histories of perturbed and unperturbed waves considering small confining pressure increment of 5 kPa

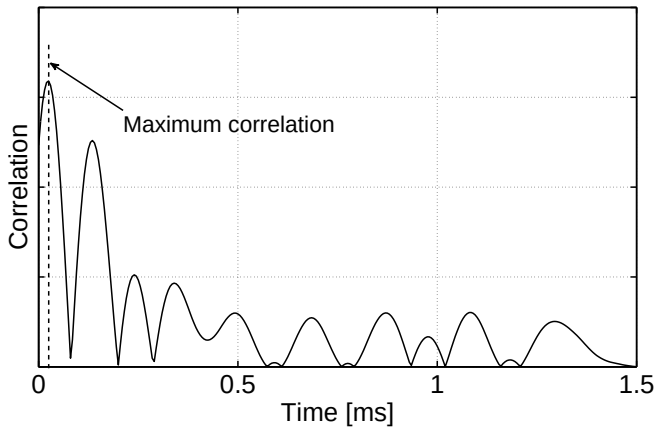

(a) Cross correlation of perturbed and unperturbed waves

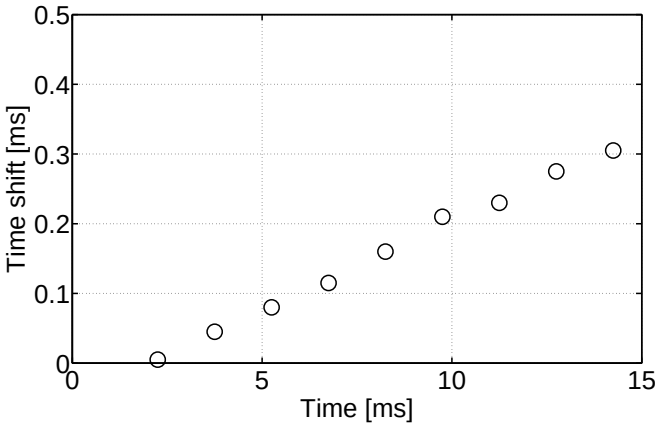

(b) Time shift for each time window over time history

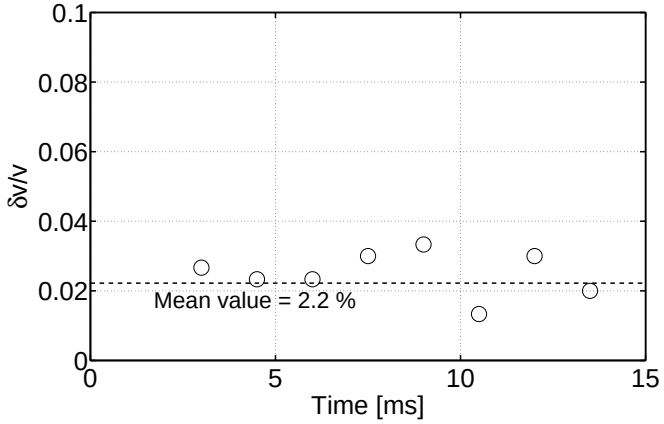

(c) Velocity change between unperturbed and perturbed waves

Figure 4.2: Steps to calculate velocity gradient of perturbed and unperturbed waves considering small confining pressure increment of 5 kPa

4.4 Stretch technique

The stretch technique of the coda wave interferometry considers another approach to calculate the change in compared signals. The faster signal is stretched gradually and cross correlated with the slower signal. For each $\theta-$value, cross correlation is calculated, where $\theta = \delta v/v = -\delta t/t$. The $\theta-$value that returns the highest correlation is considered the velocity gradient between these two signals. The normalized cross correlation coefficient is given by Sens-Schönfelder & Larose [2008] as:

$$CC(\theta) = \frac{\int_0^T u_{unp}(t) u_{per}\left[t(1-\theta)\right] dt}{\sqrt{\int_0^T u_{unp}^2(t) dt \int_0^T u_{per}^2\left[t(1-\theta)\right] dt}} \tag{4.2}$$

where T is the length of the time history considered. Since the signal is considered and calculated as a whole in the stretch technique, the correlation between the two signals is biased towards the higher amplitudes at the beginning of the signal. To overcome this bias, Dai et al. [2013] suggested that both signals are multiplied with an amplification function $e^{\alpha t}$, where α is a factor and t is time, which is the inverse of this decaying function of the signals. This makes the amplitudes of signals more constant. The factor α was typically in the range of 0.3 to 0.5 for the tests in this research. Using a too large value of α leads to large amplification of any deviation from zero in the coda part of the signal, which in turn leads to a bias towards that part in the cross correlation calculation. Figure 4.3 demonstrates velocity gradients $\delta v/v$ for Hostun sand at net stress 100 kPa with and without amplification after increasing the matric suction from 1 kPa to 2 kPa. The figure signifies the help amplification offers in simplifying finding the peak of the curve since the stretching curve without amplification is flatter. Both curves have peaks that are typically close to each other. In this example, the peaks coincide with each other. Using amplification is more accurate, and the peak of its curve is easier to locate.

Figure 4.4 compares the stretch technique and the doublet technique of the coda wave interferometry for the same data in Figure 4.3. The cross correlation of the stretch technique is plotted against values of $\theta = \delta v/v$ between 0 % and 5 %. While the velocity gradient of the doublet technique is presented with its standard deviation, both techniques result in very similar values.

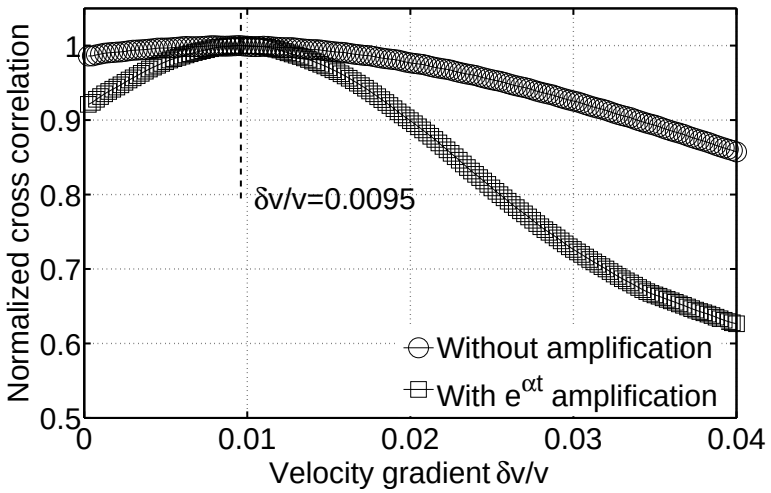

Figure 4.3: Velocity gradient $\delta v/v$ for Hostun sand at net stress 100 kPa with and without amplification

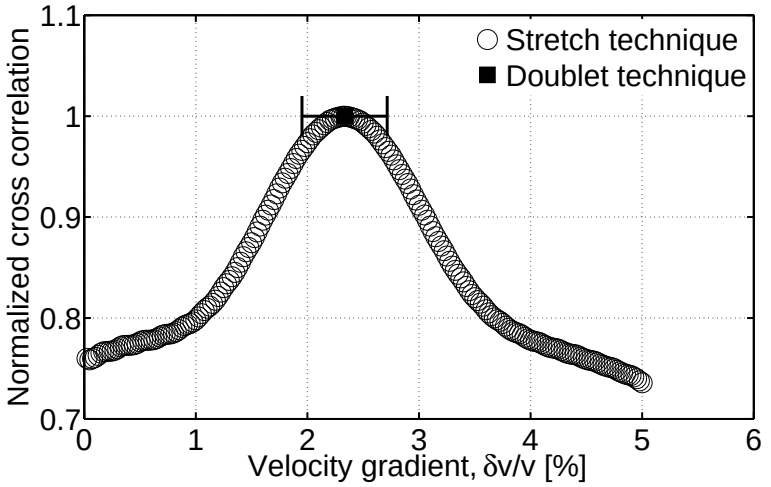

Figure 4.4: Velocity gradient $\delta v/v$ calculated with stretch technique and doublet technique with the standard deviation

4.5 Sliding window technique

The standard procedure in the doublet technique implies dividing time history into specific non-overlapping windows and calculating cross correlation within each window. A narrow window does not usually represent the correlation between both signals. Therefore, a time history divided into narrow windows would result in too scattered time shifts. Wider windows would improve the correlation between signals within each window but decrease the number of windows in the

time history. A low number of windows leads to deriving the inclination line of $\theta = \delta v/v$ from only a couple of points. Hadziioannou et al. [2009] showed that when the signal-to-noise ratio is decreased to 2, velocity change measurements become inaccurate.

To avoid this problem, a technique is introduced here to detect the time shift between two signals in a more reliable way. This technique is an improvement of the doublet technique. A single sliding window is considered. This window should be wide enough to have a good representation of the correlation within it. The window is then slid along the time history. For each slide, the time shift from cross correlation is obtained. The cross correlation coefficient follows Equation 4.2, except that windows are overlapping, which means, t_c takes more values, while for the doublet technique, the number of values for t_c is $T/2t_w$. As a result, time shifts for all slid windows along the time history are presented as in Figure 4.5. The inclination of the line represents $\theta = \delta v/v$. The number of time shifts is large enough to make deriving the inclination line more stable. A window width of about 2 ms and a slide step of about 50 μs gave satisfying results for the data in this research. Another way to see this is by calculating cross correlation from a large number of overlapping windows in the time domain. This technique is not to be confused with the cross-spectral moving-window technique proposed by Poupinet et al. [1984]. Examples of utilizing it can be found in [Fréchet et al., 1989; Clarke et al., 2011; Hadziioannou et al., 2009; Mikesell et al., 2015]. In the cross-spectral moving-window technique, a window is moved along the whole time history, and Fourier transform is computed for each window. The slope of the phase indicates the time shift between the two signals. While in the sliding window technique used here, the cross correlation is calculated directly in the time domain. Estimation of the accuracy of this technique is carried out in the next section.

4.6 Comparison among CWI techniques

A comparison among the above-mentioned CWI techniques is required, in which the accuracy and robustness of these techniques under the absence and the presence of noise can be analyzed. For this purpose, a signal was chosen from this

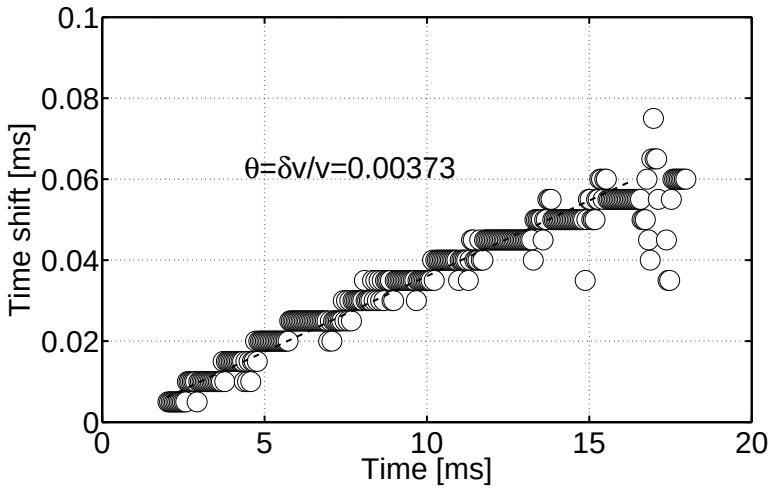

Figure 4.5: Time shift for slid windows over time history for Hostun sand with net stress of 100 kPa after increasing suction pressure from 4 kPa to 6 kPa

research, and its sampling frequency was increased 10 times, from 200 kHz to 2 MHz, using linear interpolation. This increase was desired in order to increase the resolution of the analysis. Then, an artificial shrinking by an arbitrary value of 1 % was mathematically produced. The objective of this procedure is to have two waves, an unperturbed wave (the first one) and a perturbed wave (the second one), where the difference between them is defined. The three techniques were utilized to determine the change in velocity between these two waves. Subsequently, random white noise was introduced to both waves. The signal-to-noise ratio was SNR=25 dB. Then, the three techniques were applied once again to the exact same two noisy signals.

Figure 4.6 shows the results of the doublet technique for the two clean signals (without noise) in Figure 4.6a. The window used for this technique has a width of 650 μs. The time shift has an inclination of $\theta = \delta v/v = 1$ %. Figure 4.6c shows that the θ has some deviation from its mean value. Figure 4.7b shows the results of applying the stretch technique with amplification to the clean signals. Values of θ between 0 % and 2 % with steps of 0.01 % each were tested. This technique produced a curve, whose peak is at the correct value of $\theta = 1$ %. For this technique, resampling one of the two signals is necessary, which is not a trivial task. Linear interpolation was used here. Both signals were amplified with amplification factor $\alpha = 0.3$, in order to correct for the bias in cross correlation towards the higher energy in the main part of the signal (see Section 4.4). Figure 4.7c

demonstrates the outcome of the sliding window technique. The inclination of the time shift is $\theta = \delta v/v = 1$ %, providing the correct answer. The window was slid a couple of hundred times over the time axis, producing a very dense θ-line. The window used for this technique has a width of 650 μs and was slid with 25-μs steps. There is a slight deviation in the line, but it is compensated for by the density of the data points. On the other hand, the doublet technique is simpler to calculate, while the other two require additional mathematical steps.

The results of the doublet technique for the noisy signals in Figure 4.8a are shown in Figures 4.8b and 4.8c. It is evident that the time shift does not strictly follow a straight line anymore. The velocity change $\delta v/v$ has even negative values. The mean value was found to be $\theta = \delta v/v = 1.33$ %. The data points in Figure 4.8c have a significant deviation from their mean value. It is obvious that this technique becomes unstable at this signal-to-noise ratio and delivers erroneous results. The normalized cross correlation from the stretch technique is plotted against velocity change in Figure 4.9b. Its peak indicates that $\theta = \delta v/v = 1.06$ %. The amplification was disregarded here because it provided a less smooth curve in Figure 4.9b. This is because the decaying function of the noisy signals is different from the one of the clean signals due to the presence of noise. Amplifying the coda part in the noisy signals leads to less satisfactory results since the cross correlation between both signals in the coda part is weaker. Figure 4.9c shows the results of the sliding window technique of the noisy signals. The time shift points lie in a line up to about 4 ms. Afterward, deviation from this mean line starts to appear. The mean change was found to be not far from the correct value with $\theta = \delta v/v = 1.03$ %. Because of the large number of data points, there is great confidence in the value derived here.

For applying these techniques, a couple of parameters were required to be chosen to improve the results, e.g., window width, amplification factor and sliding steps. Wider windows would improve the correlation between signals within each window but decrease the number of windows in the time history. A low number of windows leads to deriving the inclination line of $\theta = \delta v/v$ from only a couple of points. In the sliding window technique, sliding the window in smaller steps increases the resolution in Figure 4.9c up to a point, after which the increase in the number of steps has no influence on the result, and it needlessly increases the calculation time. The parameters had to be optimized for better results. Those

parameters were maintained for the analysis of clean and noisy signals, with the exception of the amplification factor for the reasons explained above.

From this analysis, it can be concluded that the stretch technique and the sliding window technique are stable and robust in the case of noisy signals. The doublet technique can deliver erroneous results if the signal-to-noise ratio drops below a certain value. It is recommended, therefore, to use the former two techniques for all cases and all three techniques only if the signal-to-noise ratio is sufficiently high. Since a lot of attention and effort were paid in this research to isolate all system cables and block possible noise sources, the signals acquired were of very high quality. On top of that, each signal was stacked 10 times, and a 50 kHz low-pass filter was used to improve the signal-to-noise ratio. It was noticed that two sequentially measured signals are identical, even in the coda part, indicating that noise is barely present in the measurement. Therefore, all three techniques of the coda wave interferometry were used to assess fabric change in this research. The three techniques gave the same result most of the time. Whenever they delivered slightly different values, an average mean was calculated.

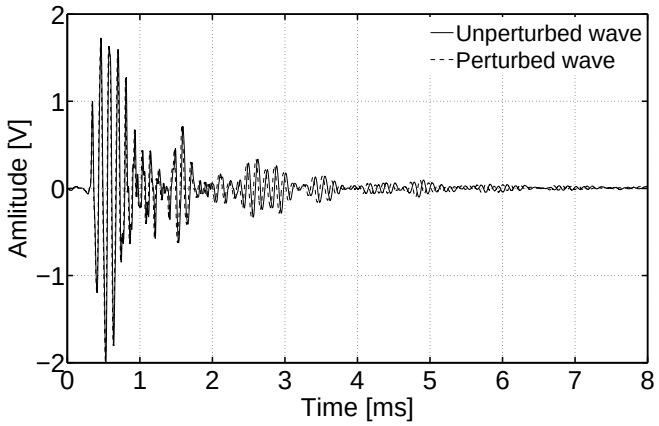

(a) Time histories of clean perturbed and unperturbed waves

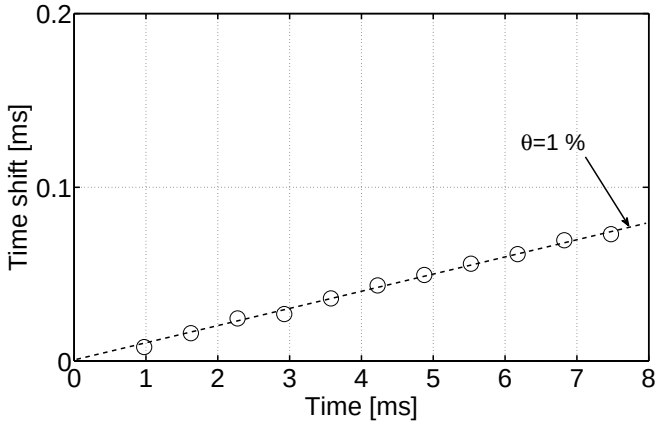

(b) Time shift for each time window over time history in the doublet technique

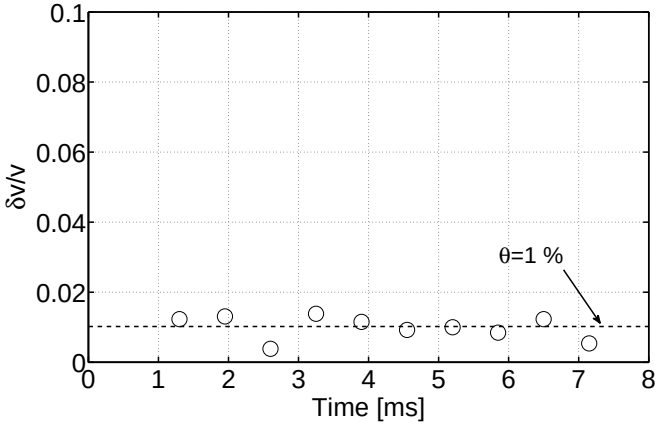

(c) Velocity change between unperturbed and perturbed waves

Figure 4.6: Results of the doublet technique for clean signals

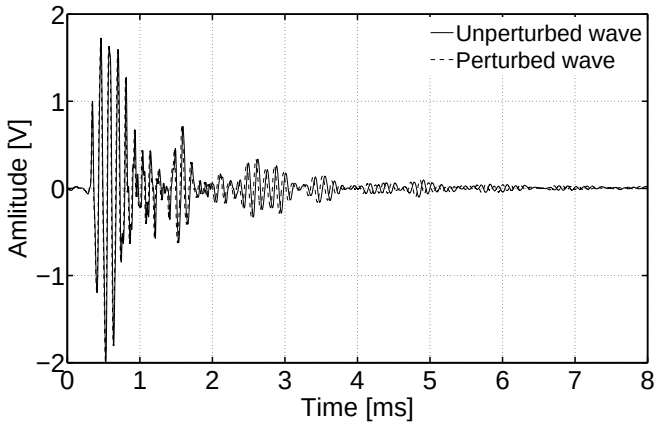

(a) Time histories of clean perturbed and unperturbed waves

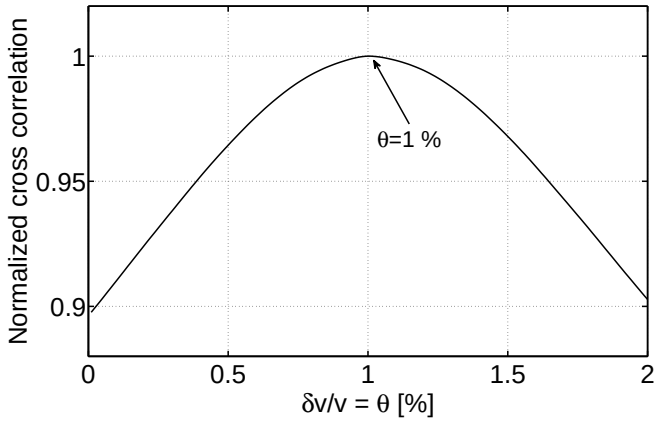

(b) Normalized cross correlation for different values of $\delta v/v$ in the stretch technique

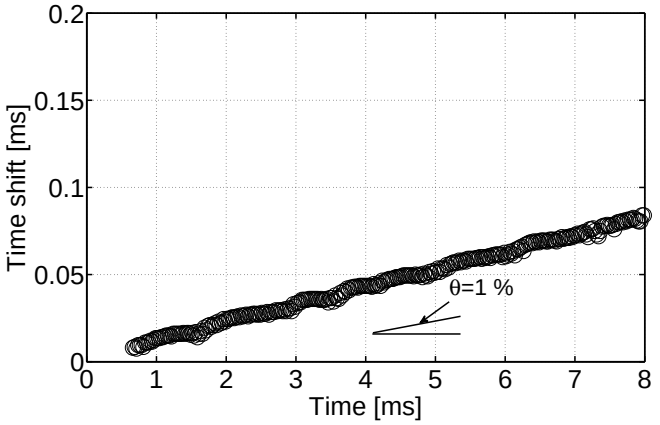

(c) Time shift for slid windows over time history in the sliding window technique

Figure 4.7: Results of the stretch technique and sliding window technique for clean signals

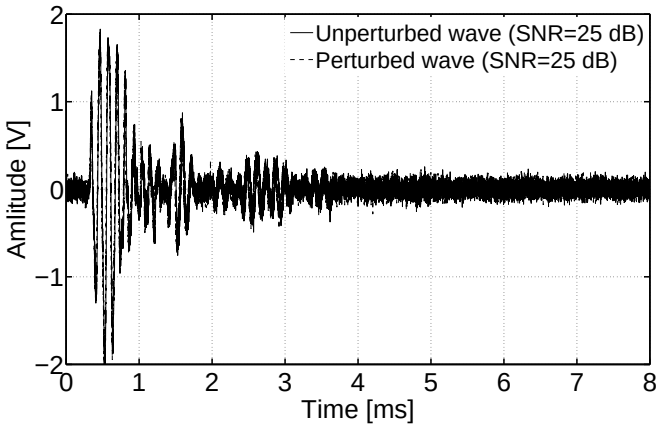

(a) Time histories of noisy perturbed and unperturbed waves

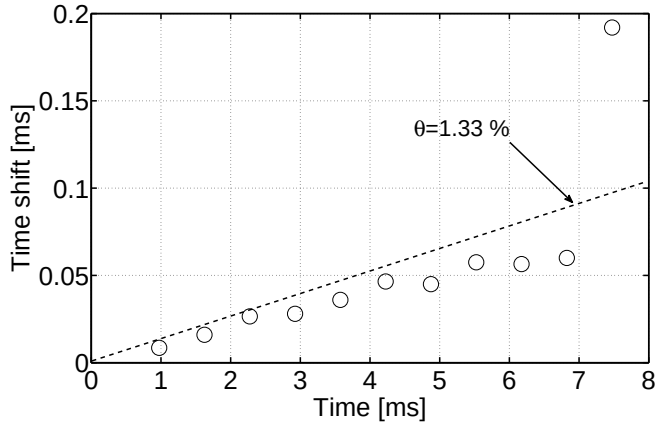

(b) Time shift for each time window over time history in the doublet technique

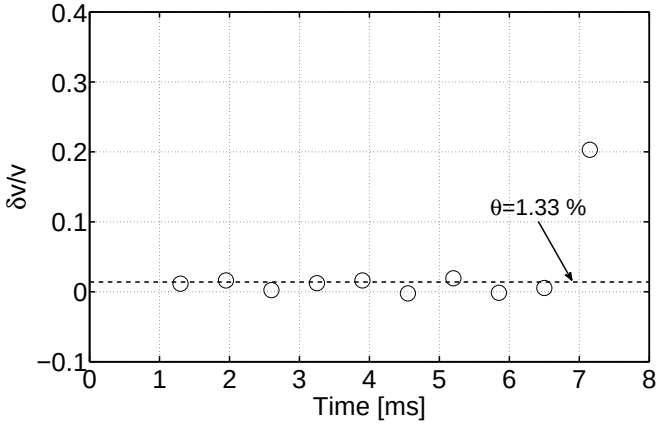

(c) Velocity change between unperturbed and perturbed waves

Figure 4.8: Results of the doublet technique for noisy signals

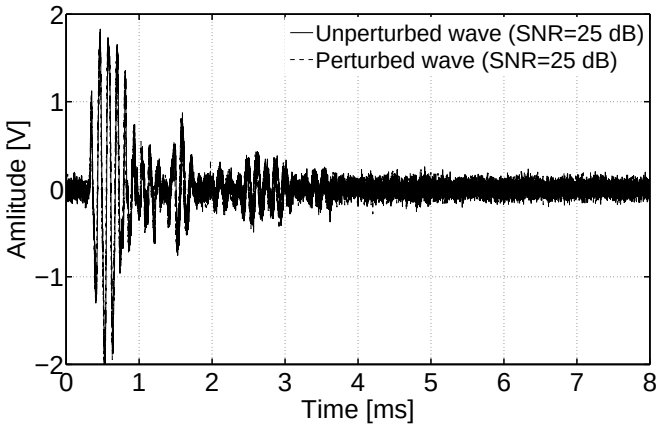

(a) Time histories of noisy perturbed and unperturbed waves

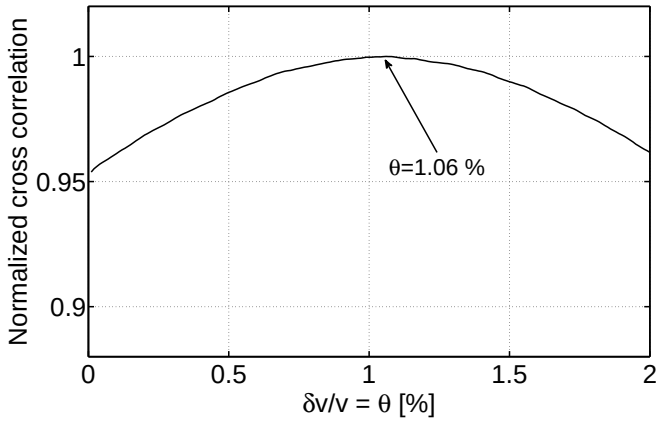

(b) Normalized cross correlation for different values of $\delta v/v$ in the stretch technique

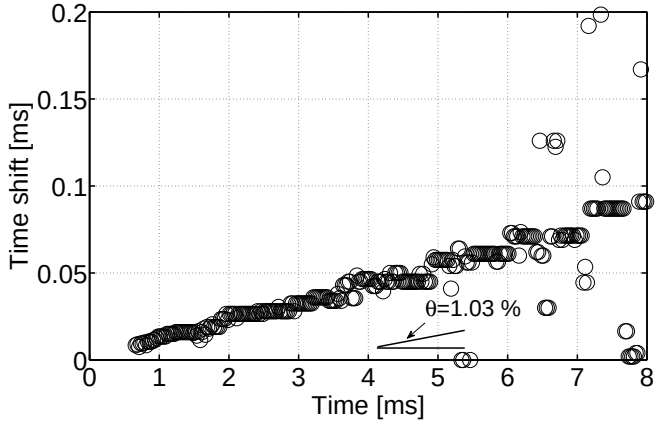

(c) Time shift for slid windows over time history in the sliding window technique

Figure 4.9: Results of the stretch technique and sliding window technique for noisy signals

4.7 Summary

The method of the coda wave interferometry was introduced in this chapter, and its existing techniques, the doublet technique and the stretch technique, were explained and discussed. The sliding window technique, as an improvement of the doublet technique, was introduced. In this technique, a window is considered, just like in the doublet technique, and slid in very tiny steps over the time history. For each slid window, the cross correlation between the two considered signals is calculated in the time domain. This technique delivered satisfactory results and is stable when random noise was added to the signals. It was successfully used in detecting fabric change for experiments in this research. It was proven that the stretch technique and the sliding window technique have a great advantage over the more commonly used doublet technique. In the absence of noise, the above-mentioned techniques deliver similar results. All three techniques were used in this research to determine velocity change. The CWI is limited to detecting velocity change in a medium. It does not measure absolute velocity. The change in velocity has to be small enough, in the range of a few percentage points, between two consecutive waves to be detected with this method. Furthermore, in the case of local change in the medium, localization of that change is not possible.

Chapter 5

Physical Background of Analytical Shear Stiffness Models

5.1 Introduction

In this chapter, a discussion of the theoretical background at the contact level is carried out. Assumptions of Hertzian theory are presented; then, the significance of the effects of friction, angularity and coordination number is demonstrated. These effects are often neglected when proposing models for small strain stiffness in the literature. It is shown here that these effects are essential for any model of shear modulus or wave velocity. This discussion is necessary to establish a model for creep in granular material in Chapter 6.

5.2 Hertzian theory

Stiffness at small strain is controlled by the interaction of particles in their contact area. Therefore, this load-deformation behavior is a result of a fabric response. This stiffness determines the elastic wave velocity. When a force applied to two solid particles, these particles deform at their contact areas. Contact theories attempt to relate applied load to particle and grain packing deformation.

The Hertzian theory considers two identical spheres made of linear elastic materials. It is assumed that the initial contact area is a point before loading. When the particles undergo a small force N normal to the contact area, they

deform producing a normal displacement δ and a contact area with radius:

$$r_c = \left[\frac{3(1-\nu_g)NR}{8G_g}\right]^{1/3} \tag{5.1}$$

$$\delta = \frac{2r_c^2}{R} \tag{5.2}$$

where ν_g is the Poisson's ratio of the particle material, R is the radius of mono-size particles that is considerably larger than r_c, and G_g is the shear stiffness of particles.

In a random mono-size-sphere packing, the normal force N can be expressed in term of an average confining pressure σ:

$$N = \frac{4\pi R^2 \sigma}{cn(1-n)} \tag{5.3}$$

where cn is the coordination number. The contact radius becomes:

$$r_c = R\left[\frac{3\pi(1-\nu_g)\sigma}{2cn(1-n)G_g}\right]^{1/3} \tag{5.4}$$

The normal stiffness is given by the following expression:

$$S_n = \frac{4r_c G_g}{1-\nu_g} \tag{5.5}$$

For a dry, random, mono-size-particle packing, Walton [1987] showed that effective bulk modulus B_{eff} and shear modulus G_{eff} of the packing can be expressed in terms of normal stiffness S_n and shear stiffness S_τ:

$$B_{eff} = \frac{cn(1-n)}{12\pi R} S_n \tag{5.6}$$

$$G_{eff} = \frac{cn(1-n)}{20\pi R}(S_n + 1.5S_\tau) \tag{5.7}$$

Substituting Equations 5.4 and 5.5 in Equation 5.6 gives:

$$B_{eff} = \left[\frac{cn^2(1-n)^2 G_g^2 \sigma}{18\pi^2(1-\nu_g)^2}\right]^{1/3} \tag{5.8}$$

5.3 Effect of friction

Mindlin [Mindlin, 1949, 1954] extended the Hertzian theory into what is now known as the Hertz-Mindlin theory by considering the relative displacement on the contact surface due to tangential forces. He suggested that slip may occur on the annulus of the contact in such a way that Coulomb's law of friction $\tau = f\sigma$ holds, where τ is the tangential component, σ is the normal pressure and f is the coefficient of friction. The relationship between τ and σ is represented experimentally by a straight line with a slope ϕ_μ. Accordingly, f is expressed as:

$$f = \frac{\tau}{\sigma} = tan\phi_\mu \tag{5.9}$$

In the Hertz-Mindlin theory, the shear stiffness can be given as:

$$S_\tau = \frac{8 r_c G_g}{2 - \nu_g} \tag{5.10}$$

while the normal stiffness remains as in Equation 5.5. The effective shear modulus, which is the shear modulus of the whole packing, becomes [Mavko et al., 2009]:

$$G_{eff} = \frac{2 + 3f - \nu_g(1 + 3f)}{5(2 - \nu_g)} \left[\frac{3cn^2(1-n)^2 G_g^2}{2\pi^2(1-\nu_g)^2} \sigma \right]^{1/3} \tag{5.11}$$

where f $(0 \leq f \leq 1)$ is the friction coefficient, while the effective bulk modulus remains as in Equation 5.8. When the particles have absolutely frictionless surface, i.e., $f = 0$, then $S_\tau = 0$, while when the particles have friction fully or partially then:

$$S_\tau = f \frac{8 r_c G_g}{2 - \nu_g} \tag{5.12}$$

$$\nu_{eff} = \frac{2 - 2f + \nu_g(2f - 1)}{2\left[4 + f - \nu_g(2 + f)\right]} \tag{5.13}$$

The effective Poisson's ratio of the whole frame, ν_{eff}, becomes a function of Poisson's ratio of the grain, ν_g, and of friction coefficient, f. When $f = 1$, then $\nu_{eff,f=1} = \nu_g/(10 - 6\nu_g)$ and ν_{eff} ranges only from 0 to 0.07 for the whole range of ν_g from 0 to 0.5. That means, for full friction, whatever Poisson's ratio the grains have, the whole packing has a very low Poisson's ratio. For a typical Poisson's ratio of quartz grains of 0.08, $\nu_{eff,f=1} = 0.008$ according to Hertz-Mindlin

theory. While when $f = 0$, then $\nu_{eff,f=0} = 0.25$. Figure 5.1 demonstrates how influential f is on the value of effective Poisson's ratio of the whole frame as represented mathematically by Equation 5.13. It is noted in this figure how the effective Poisson's ratio strongly depends on the friction coefficient for any value of Poisson's ratio of grains.

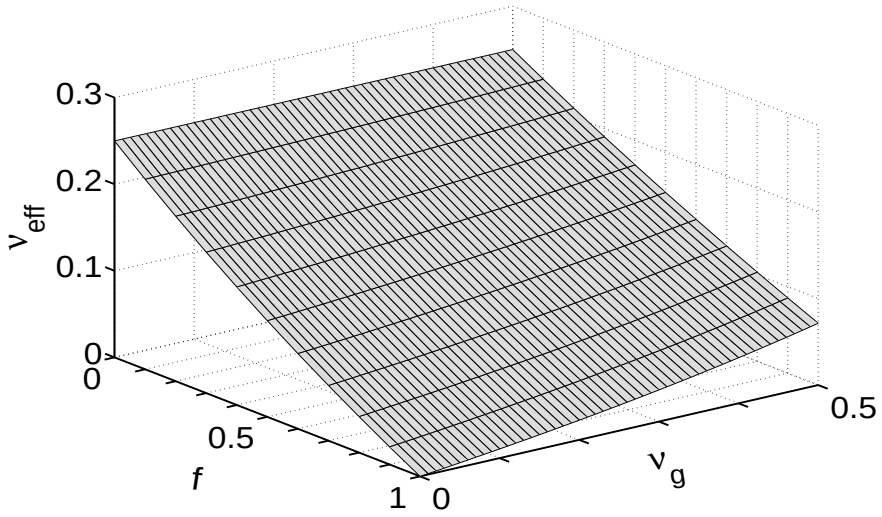

Figure 5.1: Variation of the effective Poisson's ratio of the frame, ν_{eff}, with the grain Poisson's ratio, ν_g, for different values of friction coefficient, f, after Equation 5.13

Bachrach [1998] and Bachrach et al. [2000] modeled sand as a material with two types of particles: 1) a material with all the particles having friction $f = 1$ and $S_\tau \neq 0$; thus, non-slipping particles and 2) a material without any friction $f = 0$ and $S_\tau = 0$ with the possibility to slip. They measured p- and s-wave velocities in sand in the field, from which they calculated Poisson's ratio and compared it with the one suggested by the Hertz-Mindlin theory. There was a considerable difference between both values. As shown in Figure 5.1, the theoretical value of effective Poisson's ratio is very small for the friction of $f = 1$ but increases significantly as friction decreases. The reason for that is, the slip decreases the shearing between grains. To overcome this disparity, they assumed 50 % of non-slipping particles and 50 % of slipping particles. This results in a coincide of calculated and measured Poisson's ratio.

The influence of interparticle friction on soil response was studied by Barreto

& O'Sullivan [2012] using an extensive set of three-dimensional discrete element method simulations. They simulated triaxial and true triaxial compression tests on samples with different coefficients of friction from 0.01 to 0.5. They determined that an increase in the coefficients of friction added to the stability in macro scale and increased the shear stiffness. They found that when friction between particles is dominant, the strong force chains that carry most of the load tend to buckle and rely less on the surrounding weaker chains to support them. While when friction is low, these strong force chains lean on their neighboring particles causing lateral strain.

Friction in granular material was evaluated using a micromechanical model of a three-dimensional irregular pack of spherical glass beads [Holtzman et al., 2010]. They analyzed the sensitivity of effective moduli to the intergranular friction coefficient. They confirmed that the shear modulus increase with the friction coefficient.

5.4 Effect of angularity

The shape of particles can have a significant influence on the macro stiffness. Contact models usually consider perfect spheres, while soil particles have some degree of angularity, which is a measure of the sharpness of grain corners. Angularity is also called roundness in the literature. The Particle has local curvatures that differ in their radii, as shown in Figure 5.2.

Roundness is defined as the arithmetic mean of the roundness of the individual corners of a grain in the plane of measurement [Boggs, 2006]. The roundness of individual corners is given by the ratio of the mean radius of curvature of the corners to the radius of the maximum circle that can be inscribed within the outline of the grain in the plane of measurement [Wadell, 1932]. The degree of roundness R_W is thus expressed as:

$$R_W = \frac{\sum_{i=1}^{K} R_{ci}}{R_g K} \tag{5.14}$$

where R_{ci} is the local radius of curvature of individual corners, R_g is the radius

of the maximum inscribed circle, as shown in Figure 5.2 and K is the number of corners. In the case of a perfect sphere, R_c equals R_g.

A couple of attempts were carried out in order to simplify the time consuming and laborious process used to measure all corners in the Wadell's method. A roundness scale was presented by Russell & Taylor [1937] in which they divided roundness into five classes, from angular to well rounded, based on comparison with photographs. For each class, a roundness range was assigned. Pettijohn [1949] proposed a similar scale with slightly different values. [Powers, 1953] added one class to the previous roundness scale and adjusted the values assigned for each class. All these scales employed Wadell's definition of roundness, which has been used repeatedly by researchers. These scales do not specify the roundness accurately enough. In addition to that, assigning the particle to a specific class based on a photograph is subjective. For the particles used in this research, Wadell's definition is used to determine the roundness of sand particles. A relatively large number of particles was examined in a microscopic photo, where local radii of corners and maximum inscribed circles were measured, as explained in Chapter 6.

Neglecting the effect of angularity may result in a significant overestimation of wave velocity, as shown in Figure 5.3 [Bachrach, 1998; Bachrach et al., 2000]. The figure compares the theoretical values of s-wave velocity calculated for different coordination numbers, 4, 6 and 8, with experimental field data. A substantial difference is noticed. On the other hand, by including the effect of angularity, a very good agreement was found. By assuming the coordination number to be 5 and utilizing a roundness ratio R_c/R_g smaller than 1, theoretical data and experimental data coincided well. A similar conclusion was also found for p-waves.

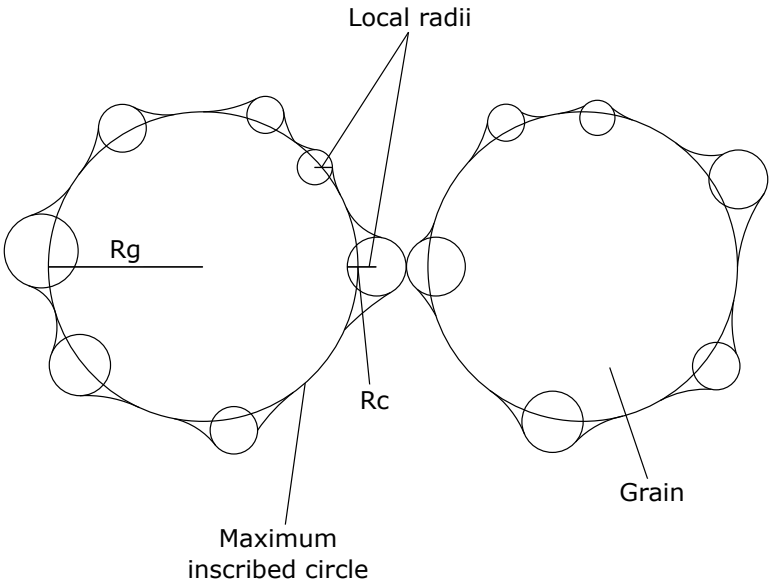

Figure 5.2: Contact between two angular grains with multiple local curvatures

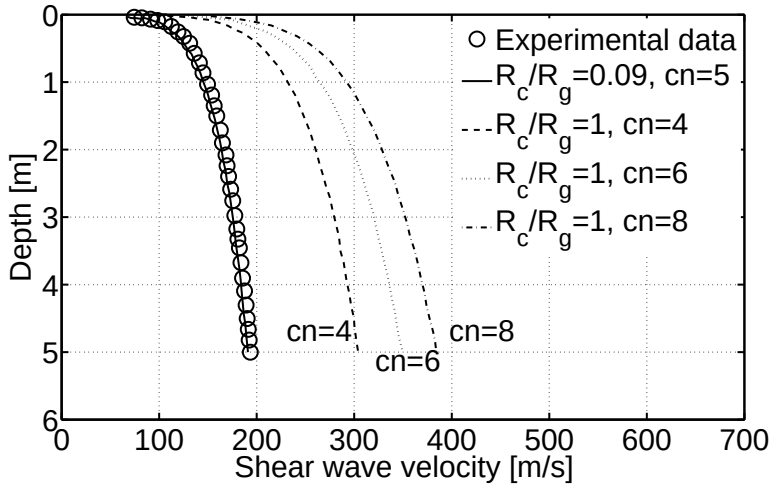

Figure 5.3: Comparison between theoretical shear wave velocity without considering of angularity with experimental data [Bachrach et al., 2000]

5.5 Effect of packing

In a grain pack, the coordination number, cn, is the average number of contacts each grain has. It plays a major role in describing granular material. The coordination number ranges from 6 for Simple Cubic, SC, to 12 for Hexagonal Close Packing, HCP, and Face Centered cubic, FCC. The reduction in void ratio causes the packing to get denser, resulting in a higher coordination number. Although *cn* ranges from 6 to 12 in theory, in reality, only from 6 to 9.5 [Santamarina et al., 2001]. The relationship between porosity in a packing of perfectly spherical grains and the average number of contacts of a grain has been studied by many researchers. Smith et al. [1929] prepared samples of lead beads and carefully counted the number of contacts for each bead. Consequently, they determined the average number of contacts for different porosities. They found that all beads had coordination numbers between 6 and 12, which corresponds well with theory. Table 5.1 demonstrates their results of the coordination number for different porosities. Manegold & Engelhardt [1933] studied this relationship analytically. They calculated the coordination number for different porosities between 0.26 and 0.77. Their result is tabulated in Mavko et al. [2009]. Murphy [1982] gathered data from many researchers on computer simulations of packing as well as experimental observations. These data can be best fitted using the following exponential function of porosity as reported by García & Medina [2006]:

$$cn = 24e^{-2.57n} - 0.371 \tag{5.15}$$

Table 5.1: Coordination number for different porosities [Smith et al., 1929]

Porosity, n	*Coordination number, cn*
0.447	6.87 ± 1.05
0.440	7.25 ± 1.16
0.426	8.05 ± 1.17
0.372	9.57 ± 2.02
0.359	9.05 ± 1.78

Figure 5.4 demonstrates the fitting curve of the compiled data by Murphy [1982], results from Smith et al. [1929] and Manegold & Engelhardt [1933], in addition to theoretical values of porosities for regular packing. It is evident that

data from different sources, theoretical and experimental, are consistent with each other.

The fact that coordination number declines with increasing porosity has a direct influence on wave velocity since velocity increases with the increase in the number of contacts per grain. This is why it is important to determine the coordination number for the specimens used in this research. The porosity of specimens used in the creep tests and the unsaturated tests in this research was around 0.41, very close to the minimum porosity for Hostun sand. Considering Figure 5.4, this matches the coordination number of 8. Therefore, the packing of specimens in this research corresponds to the regular packing of *Cubical Tetrahedral, CT*, also known in the literature as *Simple Hexagonal*.

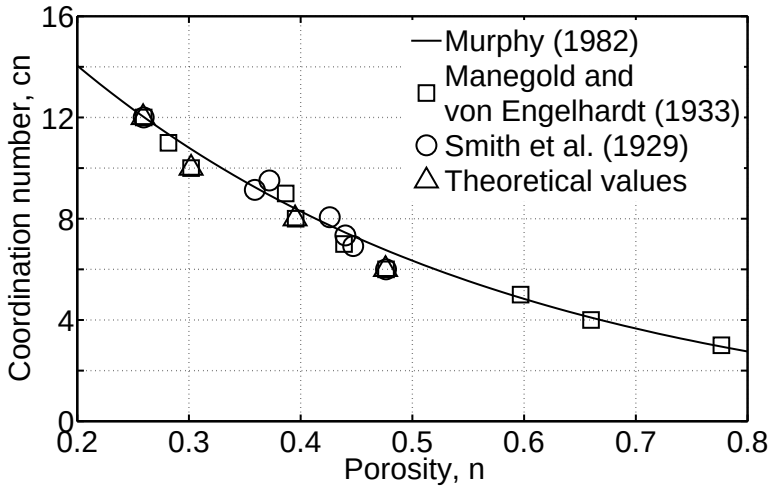

Figure 5.4: Coordination number versus porosity for random packs of identical spheres

5.6 Summary

It was demonstrated how influential interparticle friction, f, is on shear modulus and stability at the macro scale. Poisson's ratio is very sensitive to friction as well. It was also shown in the literature that the angularity of a particle, R_c/R_g, has a significant effect on shear wave velocity. The procedure to measure angularity was explained. Analytical and experimental relationships between coordination number, cn, and porosity were presented. The models for velocity or shear modulus in the literature usually discarded these important effects and handled mainly the effect of pressure. Neglecting these effects may lead to substantially erroneous results, as was demonstrated. The objective of the next chapter is to include these granular considerations in a model that also predicts the effect of time. Theoretically, friction can take any value between 0 and 1, angularity between 0 and 1 and coordination number between 6 and 12. Previous studies offered merely a fitting value for a specific set of data. In the next chapter, specific values for these parameters are derived for Hostun sand, and those effects are handled systematically with a predictive approach that is general for all granular soils.

Chapter 6

Evolution and Predicting of Shear Stiffness During Creep

6.1 Introduction

This chapter presents a series of creep tests done on specimens of Hostun sand with six different water contents. Coda wave interferometry is utilized to detect small changes in soil fabric during pressure and creep. A model is developed to describe these experimental data. This model includes the effect of friction, angularity and packing. Values for those parameters are determined specifically for Hostun sand with an approach that is generally applicable to other sands. A micromechanical approach is considered in discussing the findings.

6.2 Results and analysis

Shear wave measurements from the test on dry Hostun sand with its three phases: loading, creep and unloading are normalized and chronologically cascaded in Figure 6.1. This cascade includes 86 signals. A measurement of the shear wave was recorded every 2-kPa increment in the loading phase, starting from 10 kPa up to 80 kPa. Then in the 8-hour creep phase, a measurement was recorded every 30 minutes. In the unloading phase, a measurement was taken in 2-kPa interval steps down to 10 kPa. During loading and unloading, differences in time arrival of signals are more apparent in the coda part. It is evident how signals are accumulating change in time arrival while moving right on the x-axis. In the creep phase

of the test, there is no detectable difference between two consecutive signals in the first arrival part. Such consecutive signals are almost identical and coincide with each other. On the other hand, a slight change in time arrival is visually distinguishable in the coda part throughout the creep phase. By following the mathematical procedure of coda wave interferometry as described in Chapter 4, even such a small difference can be determined.

Figure 6.2a shows two shear wave measurements in the creep phase of the test on dry Hostun sand taken at 0 min (unperturbed wave) and at 30 min (perturbed wave) after starting creep. The two rectangular windows i and ii indicate the main part and the coda part of the signals. Both waves in the main part (window i) are plotted in a higher resolution in Figure 6.2b. It is clear that these signals coincide with each other, and determining any time shift between them is very difficult. Figure 6.2c demonstrates a visible time shift between perturbed and unperturbed signals in the coda part (window ii). This time shift increases proportionally to travel time as window ii moves right. By dividing travel time into such windows, it is possible to calculate the average time shift for each window. This is done by determining the maximum cross correlation between the perturbed and the unperturbed waves in each such window. To increase the signal-to-noise ratio, each measurement in this research was stacked 10 times.

A time shift for each time window is calculated and plotted versus time in Figure 6.3. It is worth mentioning that choosing a narrow window may cause instability of the cross correlation calculations. A wide time window, on the other hand, involves more averaging of time shift inside the window during the cross correlation process in addition to having fewer values to calculate the slope inclination from. Consequently, typically 7 to 10 time windows were considered for analysis in this research. By dividing the time shift over the central time of each time window, the inclination of the slope $\theta = -\delta t/t$ that represents velocity gradient $\delta v/v$ is calculated as in Figure 6.4. The inclination θ can be calculated between each two points in Figure 6.3 then averaged over the whole travel time. Velocity gradient for Hostun sand with $S = 0$ % was found to be 0.375 % for 30 min of creep time. This exhibits the valuable feature of coda wave interferometry in identifying such a slight medium change, which cannot be detected in other methods. Figure 6.5 shows the velocity gradient and its accumulation over the loading phase of the test. The gradient starts by about 2.3 % at 10-12 kPa

pressure and ends by 0.6 % at 78-80 kPa. The standard deviations resulted from averaging the slope inclination $\theta = -\delta t/t$, as explained in Figures 6.3 and 6.4, are also demonstrated in Figure 6.5 as error bars. These error bars range from 0.38 % for the pressure step 10-12 kPa to 0.14 % for the pressure step 78-80 kPa.

In the stretch technique of the coda wave interferometry, the correlation between the two signals is biased towards the higher amplitudes at the beginning of the signal. These amplitudes decrease with time following a decaying function of the form $e^{-\alpha t}$, where α is a factor and t is time, as shown in Figure 6.6. To overcome this problem, the decaying function should be accounted for. Both signals are multiplied with the inverse of this decaying function resulting in signals with more steady amplitudes over time, as demonstrated in Figure 6.7. The factor α in the amplification function $e^{\alpha t}$ was typically in the range of 0.3 to 0.5 for the tests in this research. Special care must be taken not to use a large exponent value, which leads to too much amplification and deviation from zero at the coda part of the signal that in turn produces misleading results.

Figure 6.8 clarifies the importance of amplifying the signals before running the cross correlation. The figure shows the relationship between normalised cross correlation and velocity gradient $\delta v/v$. The cross correlation of signals without amplification is clearly shifted towards early coming higher amplitudes. Furthermore, the cross correlation curve of signals without amplification is flat around the peak, indicating that cross correlation is not sensitive to the velocity gradient. That makes determining the maximum correlation difficult. On the other hand, amplifying both signals before calculating their cross correlation makes determining of the maximum correlation much easier since the correlation changes dramatically when the velocity gradient varies. Additionally, the velocity gradient is shifted towards the coda of the signals where more information about the medium is stacked. Therefore, amplification is always applied in this research whenever the stretch technique of coda wave interferometry is used.

In order to compare the stretch technique with the doublet technique, normalized cross correlation is plotted as a function of stretched signals with velocity gradients $\delta v/v$ between 0 % and 5 % in Figure 6.9 in addition to the velocity gradient from the doublet technique with its standard deviation. It is obvious from this figure that both techniques produce an almost identical value of velocity

gradient for this specific example of pressure increase from 10 kPa to 12 kPa.

The improved technique to calculate the coda wave interferometry, the sliding window, was introduced in Section 4.5. Since the measurements taken in this research were of high quality, the three techniques of coda wave, the doublet technique, the stretch technique and the sliding window technique, should give similar results as demonstrated in Section 4.6. To verify this, all three techniques were used to calculate the accumulated velocity gradient for all steps in the loading phase, from 0 kPa to 80 kPa, of the test on Hostun sand with $S = 0$ %. The results are plotted in Figure 6.10. The curves approximately coincide with each other over 35 steps, suggesting that all techniques are equally effective. Accordingly, these techniques were cooperatively used to evaluate signals in this research. All techniques led to the same value most of the time. Whenever they delivered slightly different values, an average mean was calculated.

Figure 6.11 shows the shear wave velocity gradient for Hostun sand with $S = 0$ % in loading from 10 kPa to 80 kPa, creep for 8 hours at 80 kPa and unloading back to 10 kPa. The figure demonstrates clearly how velocity changes significantly at low confining pressure. The gradient value for each pressure step is around 3 % for low pressure values and decreases rapidly with increasing pressure till it reaches about 0.5 % at 80 kPa. Figure 6.12 demonstrates the accumulated velocity gradient over the whole test. In the loading phase, shear wave velocity changed about 39 %, while in the creep phase gradient was as little as 1.25 %.

The normalized shear wave velocity for Hostun sand with $S = 0$ % in all three phases of the test is illustrated in Figure 6.13. The velocity is normalized to its initial value at confining pressure of 10 kPa. It increases 41.63 %, following the accumulative gradient of the loading phase from Figure 6.12. In the creep phase, it increases merely 1.25 %, then declines down to almost the initial value in the unloading phase. The slope of loading and unloading curves is a straight line in the logarithmic scale, indicating a power law of the form $v_s \propto \sigma^n$, where n is 0.167.

Figure 6.14 demonstrates the accumulated gradient in shear wave velocity during the 8-hour creep phase for Hostun sand with S=0 %. Figures 6.15 through 6.19 show the accumulated gradient of shear wave velocity for degrees of saturation of 19.7 %, 33.9 %, 56.3 %, 80.5 % and 100 %, respectively.

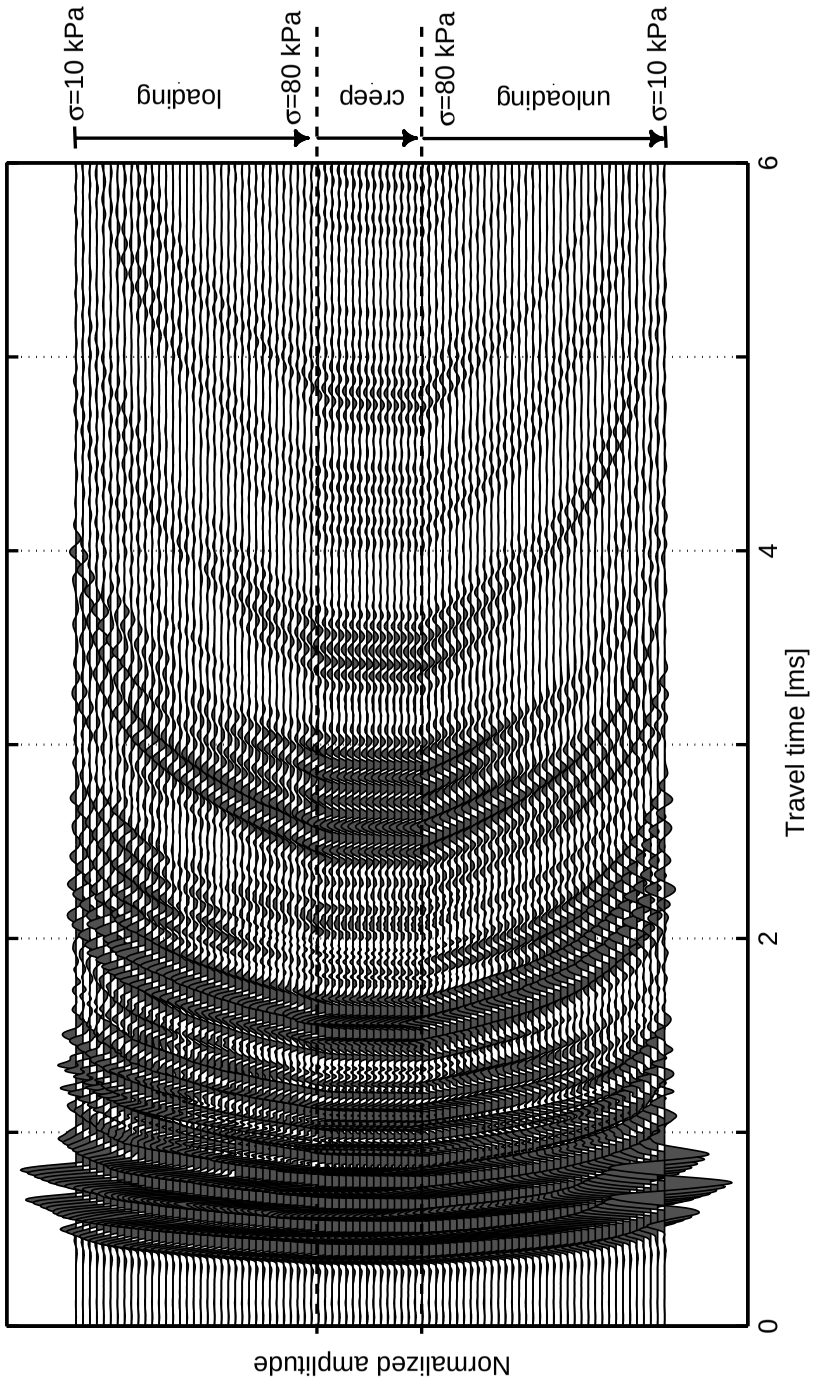

Figure 6.1: Cascade of 86 shear wave measurements on dry Hostun sand during loading, creep and unloading phases of the test

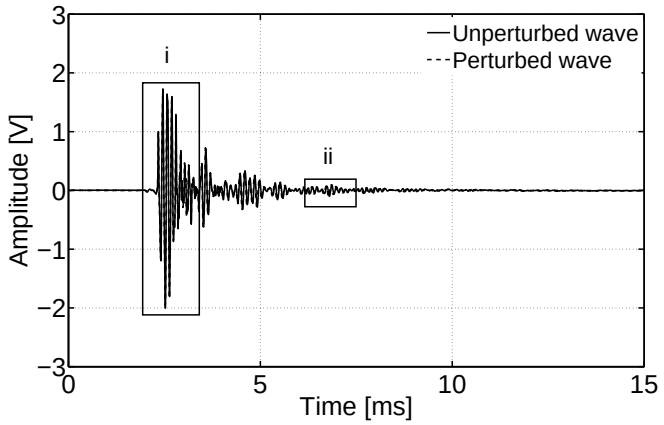

(a) Time histories of an unperturbed wave at 0 min and a perturbed wave at 30 min after starting creep

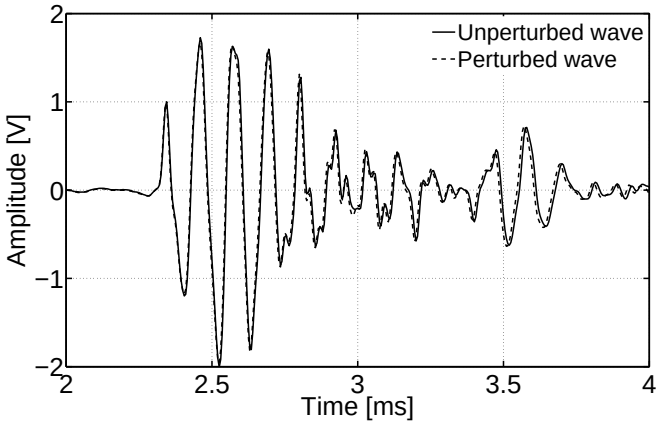

(b) Time histories in window i of perturbed and unperturbed waves in the main part of the wave

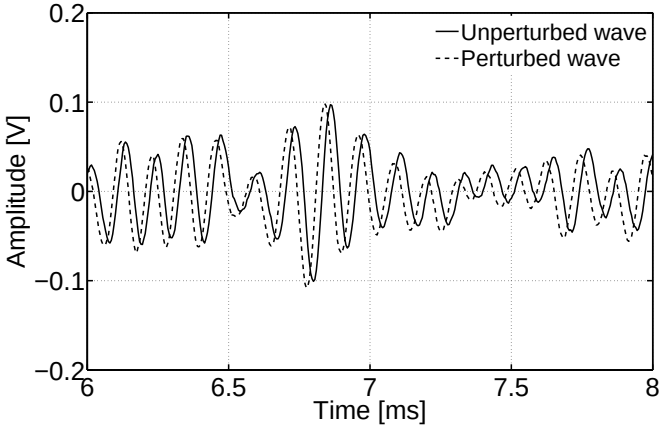

(c) Time histories in window ii of perturbed and unperturbed waves in the coda part of the wave

Figure 6.2: Time histories of perturbed and unperturbed waves considering 30 min creep time

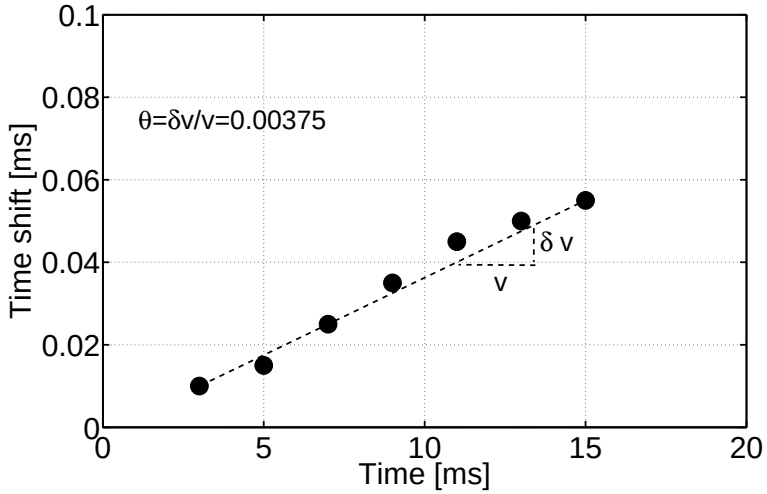

Figure 6.3: Time shift for each time window over time history for dry Hostun sand. Shear wave measurements were taken at 0 min and 30 min after starting creep

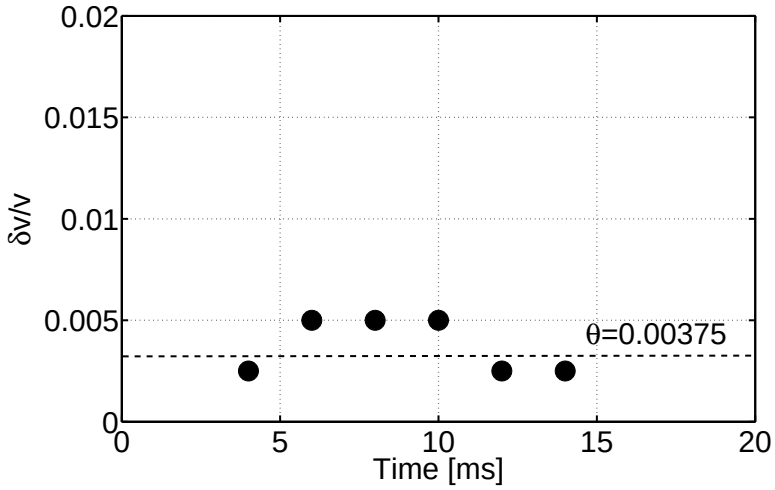

Figure 6.4: Velocity gradient for each time window over time history for dry Hostun sand. Shear wave measurements were taken at 0 min and 30 min after starting creep

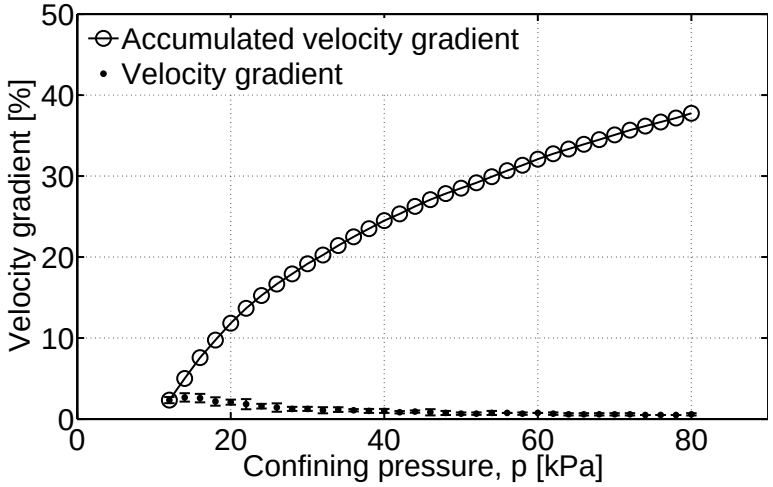

Figure 6.5: Velocity gradient with standard deviation and accumulated velocity gradient during loading

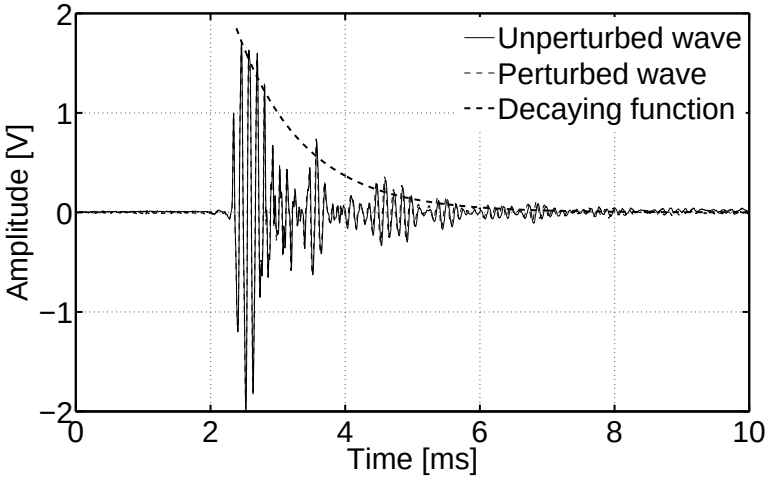

Figure 6.6: Time histories of perturbed and unperturbed waves with decaying function

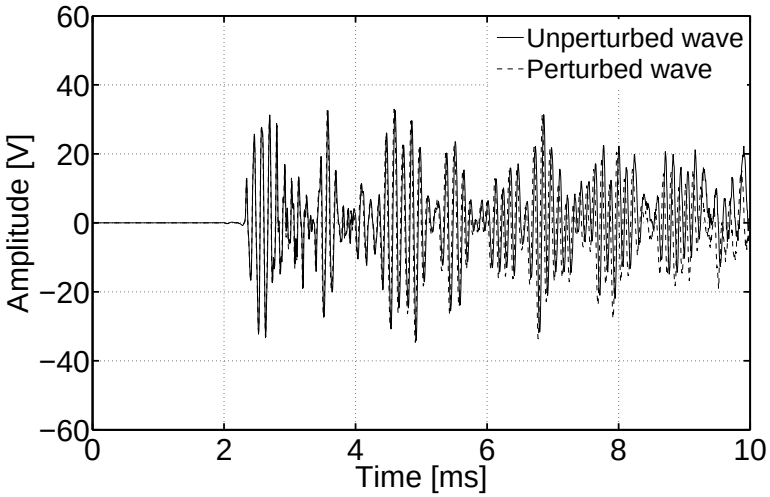

Figure 6.7: Time histories of perturbed and unperturbed waves after multiplying with amplification function $e^{\alpha t}$

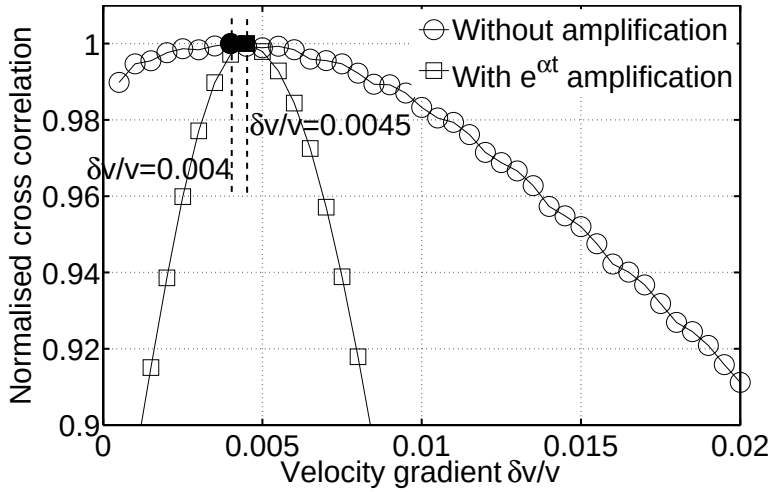

Figure 6.8: Velocity gradient $\delta v/v$ for Hostun sand with S=0 % with and without amplification

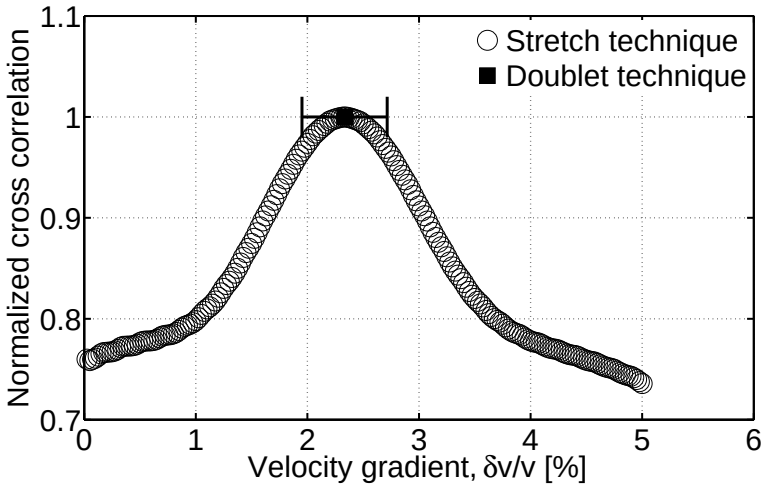

Figure 6.9: Velocity gradient $\delta v/v$ calculated with stretch technique and doublet technique with the standard deviation

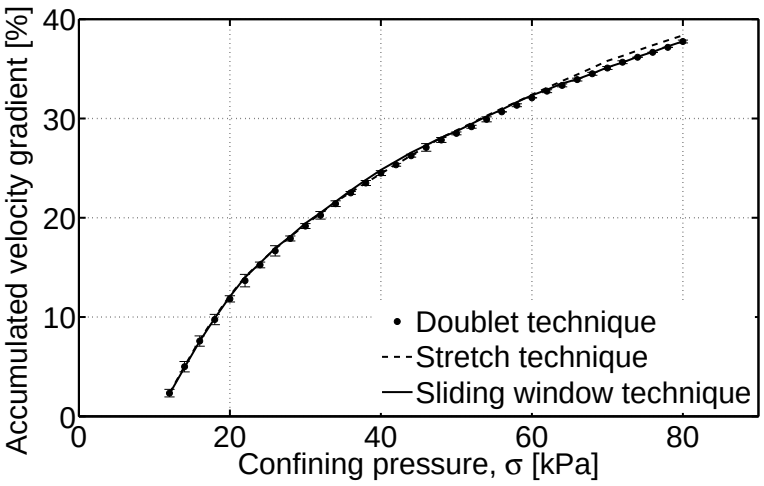

Figure 6.10: The stretch technique, the doublet technique and the sliding window technique of coda wave interferometry for Hostun sand with S=0 %

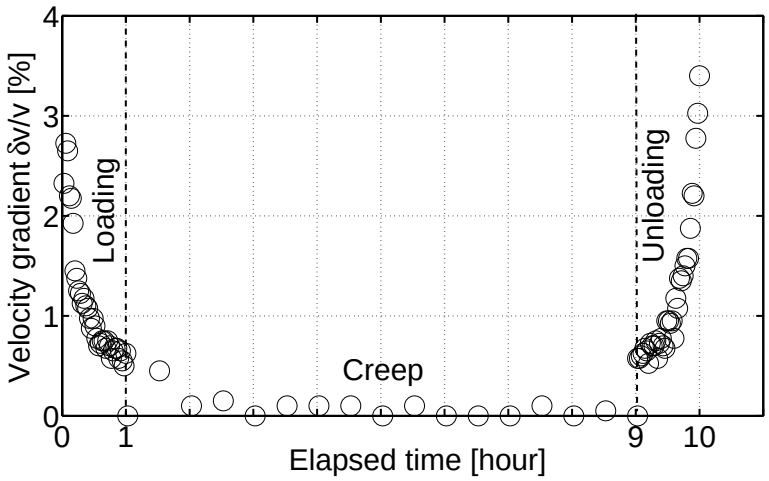

Figure 6.11: Velocity gradient $\delta v/v$ for Hostun sand with S=0 % in loading, creep and unloading phases of the test

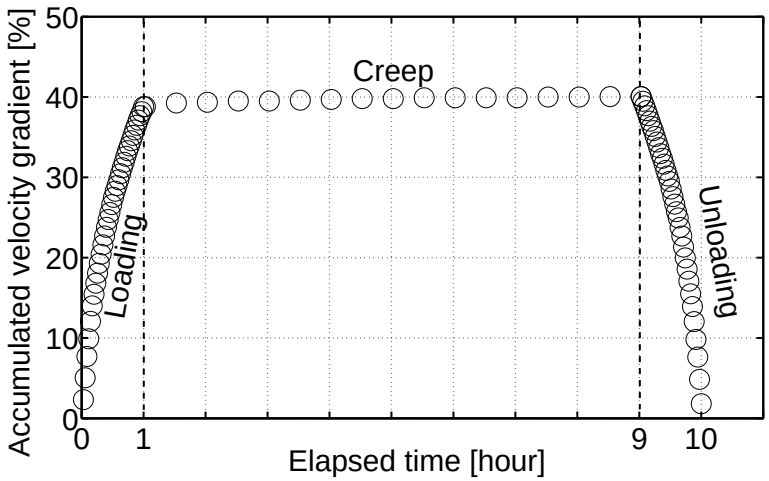

Figure 6.12: Accumulated velocity gradient for Hostun sand with S=0 % in loading, creep and unloading phases of the test

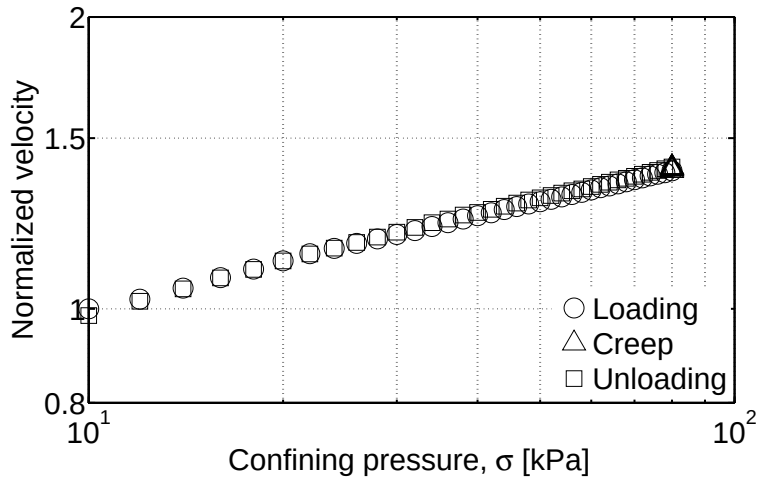

Figure 6.13: Normalized velocity for Hostun sand with S=0 % in loading, creep and unloading phases of the test versus confining pressure

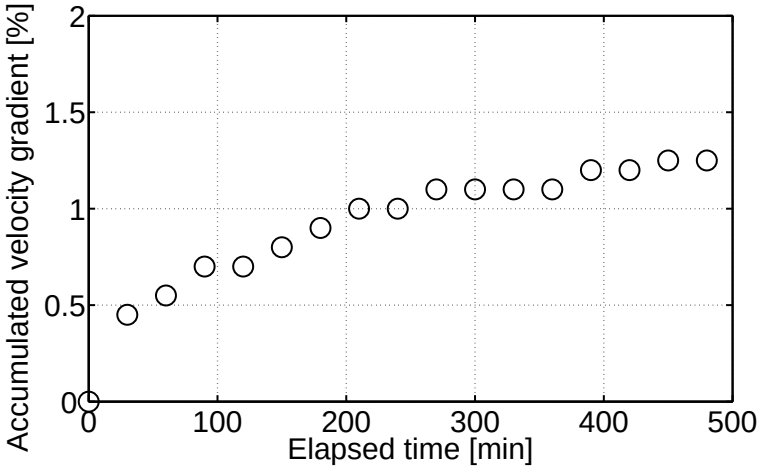

Figure 6.14: Accumulated velocity gradient during the 8-hour creep phase for Hostun sand with S=0 %

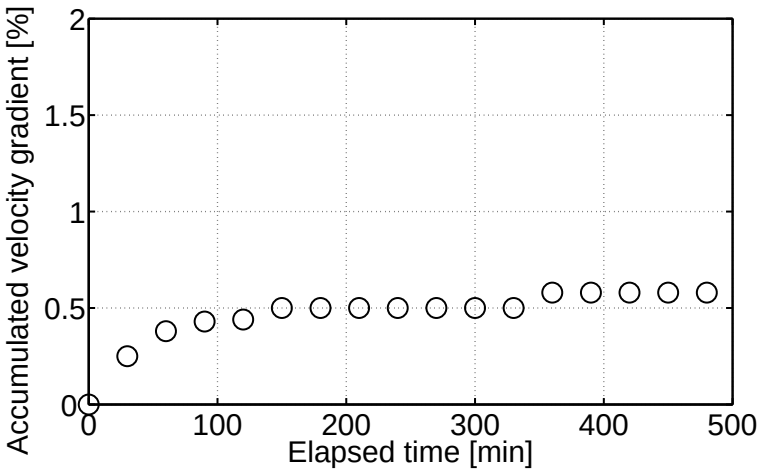

Figure 6.15: Accumulated velocity gradient during the 8-hour creep phase for Hostun sand with S=19.7 %

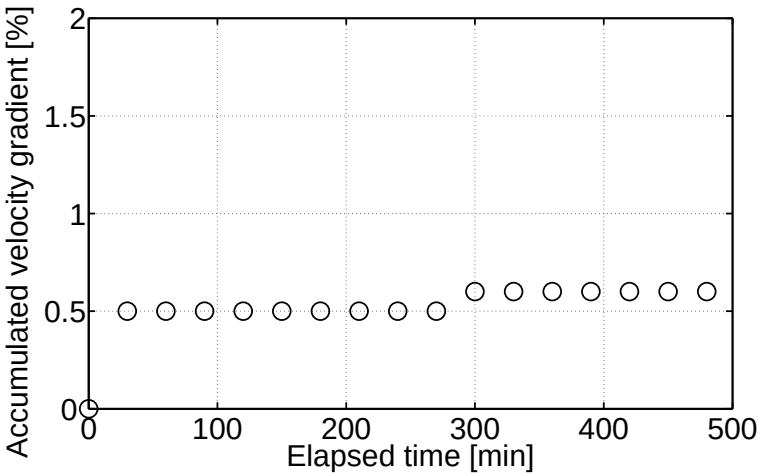

Figure 6.16: Accumulated velocity gradient during the 8-hour creep phase for Hostun sand with S=33.9 %

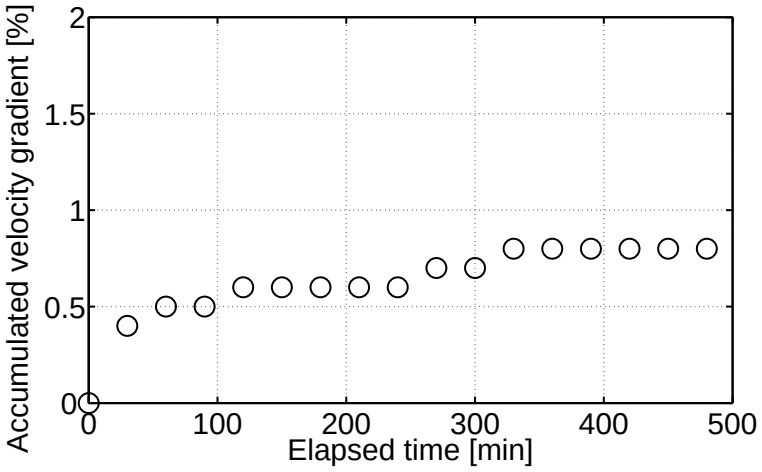

Figure 6.17: Accumulated velocity gradient during the 8-hour creep phase for Hostun sand with S=56.3 %

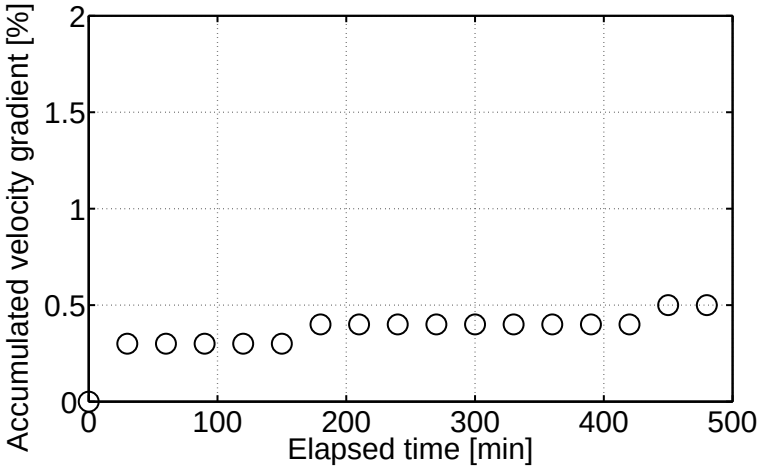

Figure 6.18: Accumulated velocity gradient during the 8-hour creep phase for Hostun sand with S=80.5 %

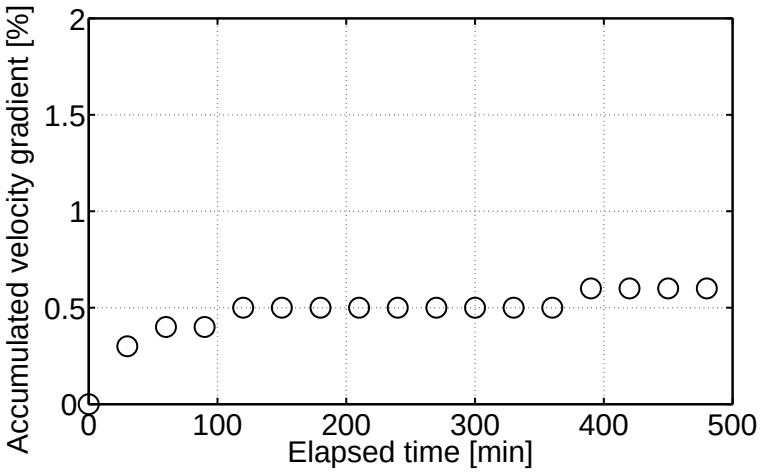

Figure 6.19: Accumulated velocity gradient during the 8-hour creep phase for Hostun sand with S=100 %

6.3 Theoretical modeling of creep in granular material

Values for different effects on shear stiffness are discussed in this section. Those effects are friction, angularity and packing (coordination number). In Chapter 5 a general discussion of these effects was presented, while in this chapter, numeral values are derived specifically for Hostun sand with an approach that is generally applicable to other sands. A model of shear modulus that includes the previous effects is developed, especially for the case at hand.

6.3.1 Effect of friction

Here values for the interparticle friction at the contact area specifically for Hostun sand will be discussed and derived. Two approaches are considered. The first one is to consider the experimental data on the friction of quartz, the mineral composing Hostun sand, and the second one is to derive interparticle friction from the macro scale shear strength.

First approach: Friction of quartz and its variables

The value of the coefficient of friction for a particle is dominated by the mineral component of that particle. Values for different minerals can be found in the literature (e.g., [Horn & Deere, 1962], [Procter & Barton, 1974] and [Skinner, 1969]). Since the dominant component of Hostun sand is quartz with $SiO_2 = 99.17$ % [Flavigny et al., 1990], the coefficient of friction of this mineral will be considered. Horn & Deere [1962] experimentally investigated the frictional characteristics of minerals. They carried out tests on different minerals to measure friction between a particle and another particle as well as between a particle and a surface of the same mineral. They measured the force required to pull a slider, which carries the particles, across a horizontal mineral surface. The effect of sliding velocity was found to be negligible. The values measured were 0.11 to 0.16 for dry quartz minerals and 0.42 to 0.51 for saturated quartz minerals. Bromwell [1966] did an extensive study on friction in quartz with different test conditions. She examined test conditions, surface roughness and a wide range of cleaning techniques. Only friction values for quartz minerals with a rough surface are considered here due to their similarity to sand particles. The friction values of dry and saturated minerals were found to be similar to each other, with 0.53 for dry and 0.48 for saturated minerals on average. Procter & Barton [1974] measured the particle-particle and particle-plane friction for quartz minerals using an interparticle friction device. The previous values of friction under saturated conditions were confirmed. They found the particle-particle friction to be 0.45 for saturated irregular quartz particles and the particle-plane friction 0.31 for dry ones. Measurements on Hostun sand, the sand used in this research, were not found in the literature. Lambe & Whitman [1979] reviewed the studies done on this topic and concluded that for practical applications, a value of $f = 0.50$ could be taken. Mitchell & Soga [2005] proposed the same value. The previous values of friction for different researchers are summarized in Table 6.1. For studies with multiple tests, an average value is presented.

It is to be noticed in Table 6.1 that friction values for dry minerals are lower than those of saturated ones in most studies. This is because the particles are contaminated with dust and organic compound when exposed to the atmosphere. These contaminating elements on the surface of the particle work as lubrication, significantly dropping the friction value. The existence of water disrupts these

Table 6.1: Summery of values of friction for quartz minerals

Researcher	*Remarks*	*Test condition*	*f*
[Horn & Deere, 1962]	No chemical cleaning on smooth surfaces	Dry	0.13
		Saturated	0.46
[Bromwell, 1966]	Normal and chemical cleaning on rough minerals	Dry	0.53
		Saturated	0.48
[Procter & Barton, 1974]	Chemical cleaning on smooth surfaces	Dry	0.31
		Saturated	0.45
[Lambe & Whitman, 1979]	Based on a literature review	-	0.50
[Mitchell & Soga, 2005]	Based on a literature review	-	0.50

contaminating elements, and thereby the friction increases. The explanation of this phenomenon was presented by Horn & Deere [1962] and adopted by many researchers, including Procter & Barton [1974], Bromwell [1966] and Cavarretta et al. [2011]. Bromwell [1966] presented evidence for this explanation by comparing friction in saturated minerals with the one in chemically cleaned, dry minerals. Both values were similar (see Table 6.1). Therefore she concluded that water does not change friction for chemically cleaned smooth surfaces. She also proves that cleaning becomes inefficient for rough particles leading to similar values of friction by dry and saturated conditions.

Procter & Barton [1974] argued that tested particles in the literature always contain some degree of contamination, and they hold molecules of water on their surface even when tested supposedly dry. This contamination and residual moisture depend on the cleaning technique, drying technique and surface roughness. Therefore, a rough surface is practically unaffected by cleaning [Bromwell, 1966] and contains remaining surface moisture, which results in friction values as if the particles were saturated. This explanation was also adopted by Lambe & Whitman [1979], who proposed using the same value of friction for quartz regardless of the presence of water. They pointed put that small friction values are produced by cleaning smooth quartz surfaces and have no significance for soils. The no-effect of water was also examined by Nascimento [1981], who detected an

antilubricating effect of water only on smooth surfaces. He suggested that the antilubricating effect of water on quartz would be produced by the orientation of water molecules at the surface, similar to what Horn & Deere [1962] previously suggested. This phenomenon cannot be generalized to other minerals and metals. For example, water has a lubricating effect on steel beads [Procter & Barton, 1974].

As the surfaces of two particles become rough, the interlocking between asperities increases the friction between these surfaces. A comparison between a smooth quartz surface and a rough one was done by Horn & Deere [1962]. They concluded that the friction increases with increasing roughness, as may be expected. This was also confirmed by Cavarretta et al. [2011]. Ivković et al. [2000] studied the influence of the contact surface roughness on the static friction coefficient and concluded that friction increases with increasing surface roughness. The values in Table 6.1 are measured values of friction on quartz minerals, which are much smoother than soil particles. It is reasonable then to expect values of friction of sand particles higher than the ones of the mineral from which they are composed. In fact, Bromwell [1966] recommended friction between 0.49 and 0.53 for quartz soil particles. Lambe & Whitman [1979] and Mitchell & Soga [2005] independently proposed the use of a friction value of $f = 0.50$ for quartz particles in natural soils since they have a rough surface. So the average value for quartz $f_{quartz} = 0.48$ obtained from Table 6.1 is considered here as the lower limit for a quartz sand like Hostun sand.

Furthermore, as the low of friction states, it was confirmed that the normal load has no influence on the friction [Bromwell, 1966; Nascimento, 1981]. Static and kinetic friction were found experimentally very similar [Horn & Deere, 1962]. In the case of kinetic friction, no influence was detected of friction velocity [Li et al., 2005]. This effect is important to eliminate for the present research since different exciting frequencies were performed, causing particles to vibrate with different particle velocities. Accordingly, if the relative movement of particles at the contact area is assumed, particles might move in respect to each other with different friction velocities, which have no influence on the friction coefficient. A summary of the effects of different variables is presented in Table 6.2.

Table 6.2: Summary of Effects on friction for quartz minerals

Variable	*Effect*
Water	- Has no effect on chemically cleaned or rough surfaces [Bromwell, 1966; Procter & Barton, 1974; Lambe & Whitman, 1979; Nascimento, 1981; Mitchell & Soga, 2005] - Increases friction on contaminated, smooth surfaces [Horn & Deere, 1962; Skinner, 1969; Procter & Barton, 1974; Nascimento, 1981]
Roughness	Increases friction [Bromwell, 1966; Ivković et al., 2000]
Cleaning	Increases friction of smooth particles [Bromwell, 1966]
Static vs. kinetic friction	No effect [Horn & Deere, 1962]
Friction velocity	No effect [Li et al., 2005]
Normal load	No effect [Bromwell, 1966; Procter & Barton, 1974; Nascimento, 1981; Li et al., 2005]

Second approach: Deriving micro scale interparticle friction from macro scale shear strength

The interparticle friction cab be linked to the macro scale strength of soil. The angle of shear resistance at constant volume, ϕ_{cv}, also known as critical state angle, was linked with friction angle ϕ_μ by many researchers. Soil during shear, regardless of its initial condition, will arrive eventually at a final void ratio, where the volume becomes constant. This state is called critical state or constant volume state. The critical state angle is a material property and independent of the conditions of the test, like initial void ratio and stress. This angle combines the interparticle friction and the interlocking between particles. Since the critical state angle and the interparticle friction angle are constant for a given material, a link between them is theoretically possible and has been suggested in the literature.

Caquot [1934] analyzed theoretically the relationship between friction angle and interparticle angle at the critical state. His relationship is given by:

$$tan\phi_{cv} = \frac{\pi}{2} f \tag{6.1}$$

Bishop [1954] presented the approximate expression to relate the critical state angle in a triaxial test to the interparticle friction angle:

$$sin\phi_{cv} = \frac{15f}{10+3f} \tag{6.2}$$

An extensive analytical study was done to investigate the influence of the interparticle friction angle on the macro scale shear strength of cohesionless materials [Horne, 1965a,b, 1969]. His equation cannot be simply expressed; therefore, the curve between ϕ_{cv} and f is derived from his work [Horne, 1969] and presented graphically in Figure 6.20. Lee [1966] found that the values predicted by Horne agree well with experimental data on feldspar, while the relationships of [Caquot, 1934] and Bishop [1954] are not supported by the results. This finding was also concluded by Bromwell [1966], who also found that for quartz $f = 0.53$ and $\phi_{cv} = 36°$ based on a shear box test. Moroto [1988] evaluated previous studies on the topic and proposed the following relationship as the best fit to the experimental and theoretical data:

$$sin\phi_{cv} = \frac{1.22f}{f+0.62} \tag{6.3}$$

As seen in Figure 6.20, which summarizes all the above-mentioned studies, experimental data from different researchers agree very well with the curve proposed by Horne [1969]. The equations of Caquot [1934] and Bishop [1954] overestimate the value of phi_cv for a given value of f. This was concluded by Bromwell [1966] and Lee [1966].

The critical state angle for Hostun sand has been studied in the literature. Schanz & Vermeer [1996] confirmed that this angle exists independently of strain and test conditions. For the case of Hostun sand under triaxial conditions, they found it to be $\phi_{cv} = 34.4° - 34.8°$. Alabdullah [2010] found it to be $\phi_{cv} = 36°$ under biaxial conditions. The average value of $\phi_{cv} = 35°$ is going to be considered here. For this value of ϕ_{cv}, the friction value of approximately 0.55 is derived from Figure 6.20. This value is slightly higher than the one of quartz obtained in Section 6.3.1, as expected due to the effect of particle roughness. The curves of Caquot [1934] and Bishop [1954] are not considered to be accurate, as discussed above. These two curves provide values of f of about $0.43 - 0.44$, which is lower than the value of friction obtained for quartz in Section 6.3.1, offering further evidence that these two curves are invalid at least for values of $f > 0.3$.

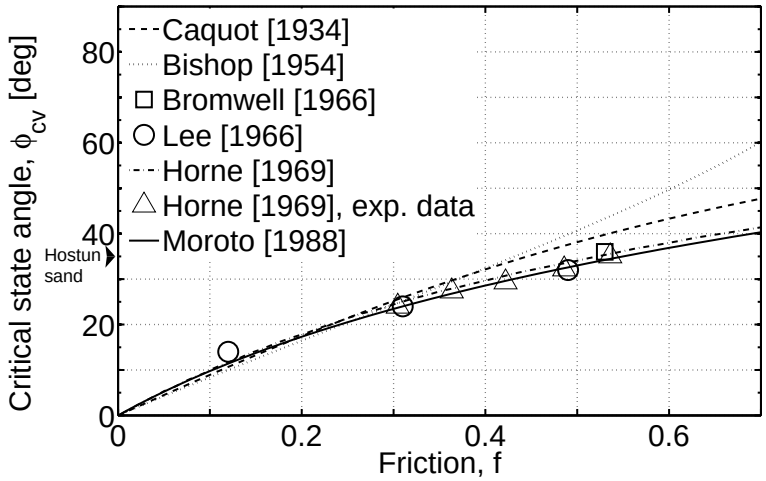

Figure 6.20: Relationship between friction, f, and critical state angle, ϕ_{cv}, from different researchers

Final remarks on friction

When the angle of the critical state, ϕ_{cv}, for a given sand is known, then Figure 6.20 or Equation 6.3 can be used to derive the value of interparticle friction. However, ϕ_{cv} is not necessarily known for all kinds of sand. In order to generalize this procedure to all the cases when the angle of friction at the peak, ϕ_p, and the dilatancy angle, ψ, are known, the following empirical equation is proposed by Alabdullah [2010] to relate these two angles with ϕ_{cv}:

$$\phi_p = 0.77\psi + \phi_{cv} \tag{6.4}$$

Alabdullah [2010] based this equation on experiments at different stress values and on a literature review. It is very close to the previously suggested equation $\phi_p = 0.8\psi + \phi_{cv}$ by Bolton [1986]. Accordingly, for any sand, when the angle of friction at the peak, ϕ_p, and the dilatancy angle, ψ, are known, angle of the critical state, ϕ_{cv}, can be calculated, and friction value, f, can be determined using Figure 6.20. It is worth pointing out here also that values of ϕ_{cv} should not be far from 33° for quartz sand and 40° for felspathic sand [Bolton, 1986].

Direct Relationships between ϕ_p and f exist in the literature [Scott, 1963; Rowe, 1962]. However, those relationships were derived for a certain packing, i.e., void ratio and density, and do not have the general applicability of the above-mentioned relations.

The previous two approaches, considering the chemical component and the shear strength, can be used to estimate interparticle friction in sand. The latter is preferred since it takes into account the roughness of the particle, which affects the macro shear strength. The first one can be considered as a lower limit for friction in a natural soil.

6.3.2 Effect of angularity

As explained in Chapter 5, neglecting the effect of angularity can lead to a significant overestimation of the shear wave velocities. Here that effect will be implemented into stiffness equations in terms of the contact curvature radius, R_c, and grain radius, R_g. The contact radius r_c is given as:

$$r_c = \left[\frac{3NR_c(1-\nu_g)}{8G_g}\right]^{1/3} \tag{6.5}$$

where N is the normal force and ν_g and G_g are Poisson's ration and shear stiffness of the particles, respectively. From the Hertzian theory, N is given in terms of the average confining pressure σ and cn the coordination number:

$$N = \frac{4\pi R^2 \sigma}{cn(1-n)} \tag{6.6}$$

This results in r_c being a function of the curvature radius, R_c, and the grain radius, R_g:

$$r_c = \left[\frac{3\pi(1-\nu_g)\sigma R_c R_g^2}{2cn(1-n)G_g}\right]^{1/3} \tag{6.7}$$

For the case of perfect spheres, $R_c = R_g$. While for angular particles, R_c may be considerably smaller than R_g.

The effective shear modulus can be rewritten to include the effect of angularity:

$$G_{eff} = \frac{2+3f-\nu_g(1+3f)}{5(2-\nu_g)}\left[\frac{3cn^2(1-n)^2G_g^2R_c}{2\pi^2(1-\nu_g)^2R_g}\sigma\right]^{1/3} \tag{6.8}$$

where f is the friction coefficient.

In order to determine the $R_c - to - R_g$ ratio, the roundness R_W is measured as explained in Chapter 5 [Wadell, 1932; Boggs, 2006]. The degree of roundness

R_W is expressed as:

$$R_W = \frac{\sum_{i=1}^{K} R_{ci}}{R_g K} \tag{6.9}$$

where R_{ci} is the local radius of curvature of individual corners, R_g is the radius of the maximum inscribed circle and K is the number of corners (Figure 5.2). A microscopic photo of Hostun sand was taken to examine the geometrical properties of particles (Figure 6.21). The angularity of this sand is distinct in this photo. Figure 6.22 describes the procedure carried out to determine the angularity of Hostun sand. In the microscopic photo, 117 grains that have all their corners exposed were selected and inspected. For each individual grain the radius of the maximum inscribed circle, R_g, and local radii of curvature of individual corners, R_{ci}, were measured, and consequently $R_c - to - R_g$ ratio, or R_W, was determined. These measurements are presented in Figure 6.23. It can be seen that the majority of grains have roundness value around 0.30. The mean for the whole sample and its standard deviation were found to be $\overline{R_W} \mp s = 0.31 \mp 0.08$. This value is in consistency with another scale of roundness proposed by Powers [1953], in which particles are divided into six roundness classes. This scale defines a roundness range for each class. Hostun sand is considered to be subangular to angular in the literature (e.g., [Sadek et al., 2007] and [Goudarzy, 2015]). For subangular to angular particles, Powers's scale defines roundness range between 0.17 and 0.35. Consequently, the value determined by measuring the geometrical properties based on Wadell's method, Equation 6.9, lies within the proposed range of Powers's scale.

6.3.3 Effect of packing

The porosity of specimens used in the creep tests and the unsaturated tests in this research was around 0.41, very close to the minimum porosity for Hostun sand. Considering Figure 5.4, this matches the coordination number of 8. Therefore, the packing of specimens in this research corresponds to the regular packing of *Cubical Tetrahedral, CT*, also known in the literature as *Simple Hexagonal*.

The elastic constants that relate strains to stress were derived for the cubical tetrahedral array, CT, by Makhlouf & Stewart [1967]. The axial strain is given

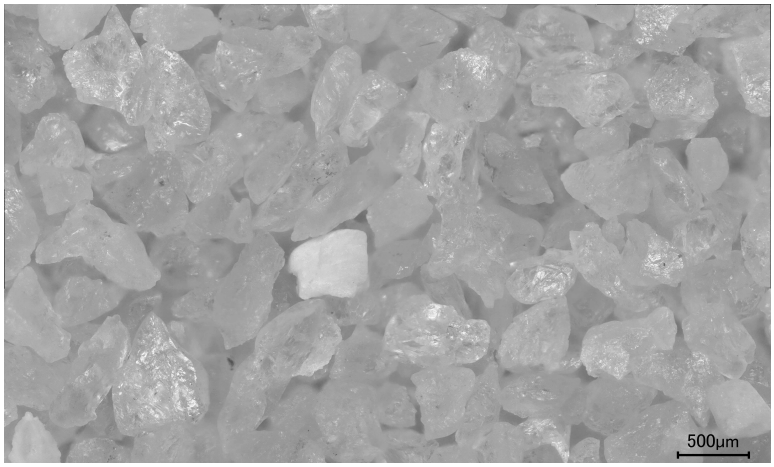

Figure 6.21: Microscope photo of Hostun sand

as:

$$\epsilon = \frac{2\sqrt{3}}{3} H R_g \sigma \tag{6.10}$$

where σ is the isotropic pressure, H is the normal compliance and R_g is the grain radius. The term HR_g is given as:

$$HR_g = \frac{3^{\frac{1}{6}}}{2} \left[\frac{2(1-\nu_g^2)}{3G_g^2 \sigma} \right]^{\frac{1}{3}} \tag{6.11}$$

Equation 6.10 can be rewritten as:

$$\epsilon = \left[\frac{2(1-\nu_g^2)}{9} \right]^{\frac{1}{3}} \left[\frac{\sigma}{G_g} \right]^{\frac{2}{3}} \tag{6.12}$$

The stress σ is then given as:

$$\sigma = \frac{3}{\sqrt{2}} \frac{G_g}{\sqrt{1-\nu_g^2}} \epsilon^{\frac{3}{2}} \tag{6.13}$$

The shear stiffness in Equation 6.8 can be specified for a cubical tetrahedral array of spheres and rewritten as a function of strain instead of stress:

$$G_{eff} = \frac{2+3f-\nu_g(1+3f)}{5(2-\nu_g)} \left[\frac{9cn^2(1-n)^2 R_c}{2\sqrt{2}\pi^2(1-\nu_g)\sqrt{1-\nu_g^2} R_g} \right]^{1/3} G_g \sqrt{\epsilon} \tag{6.14}$$

The strain rate is given as a function of pressure, σ, and time, t:

$$\dot{\epsilon} = A \left(\frac{\sigma}{\sigma_{ref}} \right)^{\alpha} \left(\frac{t_{ref}}{t} \right)^{\beta} \tag{6.15}$$

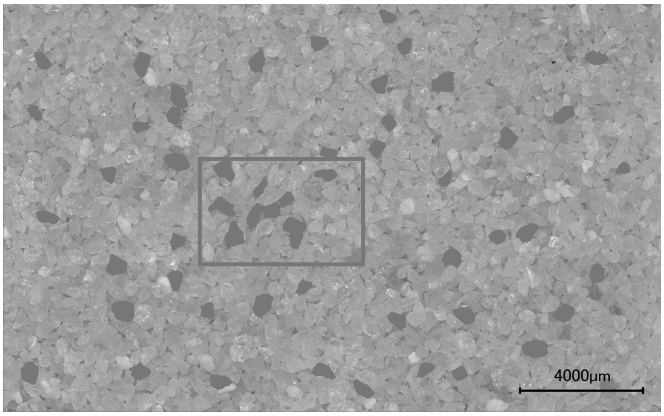

(a) Selecting sand grains to determine angularity

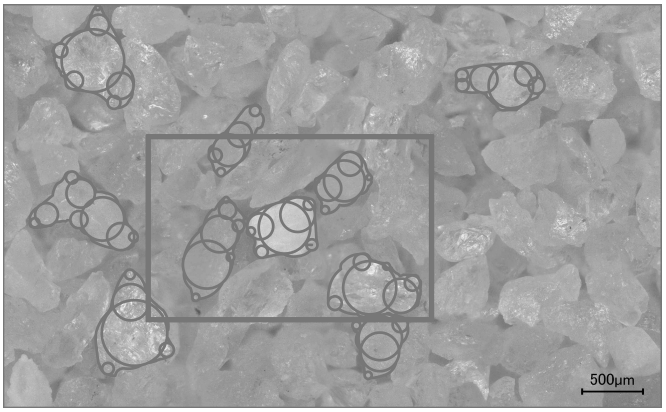

(b) Zoom-in of the box in subfigure (a)

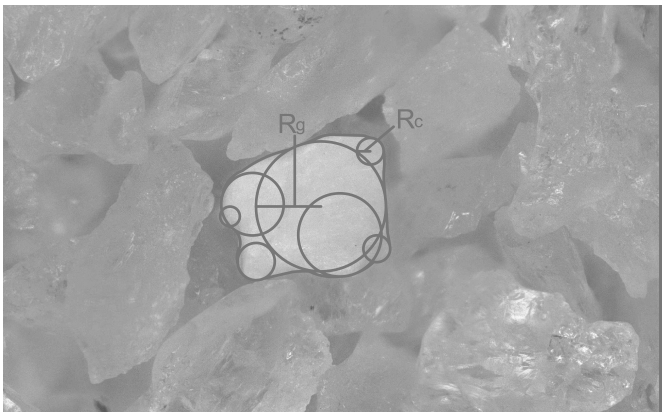

(c) Zoom-in of the box in subfigure (b). Measuring R_g and R_{ci} to determine R_W

Figure 6.22: Determining $\overline{R_W}$ for Hostun sand by measuring the radius of the maximum inscribed circle, R_g, and local radii of curvature of individual corners, R_{ci}, for numerous grains in a microscopic photo

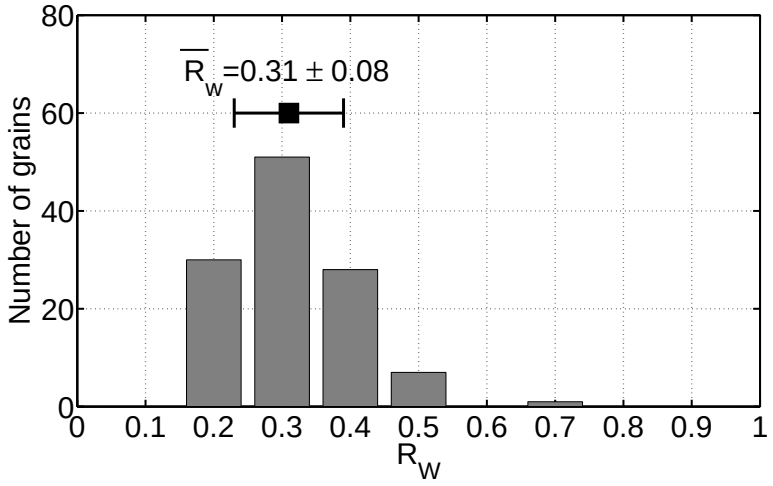

Figure 6.23: Roundness measurements of Hostun sand

where A, α and β are fitting parameters and σ_{ref} and t_{ref} are reference values for pressure and time with the following values $\sigma_{ref} = 1\ kPa$ and $t_{ref} = 1\ min$. β here represents time hardening. Since in creep the only variable here is t, the previous equation can be integrated with respect to t to obtain strain:

$$\epsilon = c + \frac{A}{1-\beta}\left(\frac{\sigma}{\sigma_{ref}}\right)^{\alpha} t_{ref}^{\beta} t^{1-\beta} \tag{6.16}$$

$\epsilon = 0$ at $t = 0\ min$, then $c = 0$. Then the previous equation can be rewritten to get the following:

$$\epsilon = \frac{A t_{ref}}{1-\beta}\left(\frac{\sigma}{\sigma_{ref}}\right)^{\alpha}\left(\frac{t}{t_{ref}}\right)^{1-\beta} \tag{6.17}$$

Substituting this expression into Equation 6.14:

$$\begin{aligned} G_{eff} =& \frac{2+3f-\nu_g(1+3f)}{5(2-\nu_g)}\left[\frac{9cn^2(1-n)^2R_c}{2\sqrt{2}\pi^2(1-\nu_g)\sqrt{1-\nu_g^2}R_g}\right]^{1/3} G_g \\ & \left[\frac{A t_{ref}}{1-\beta}\left(\frac{\sigma}{\sigma_{ref}}\right)^{\alpha}\left(\frac{t}{t_{ref}}\right)^{1-\beta}\right]^{1/2} \end{aligned} \tag{6.18}$$

During creep, where pressure is constant, the only variable here is time, t. This equation relates macro scale shear stiffness G_{eff} to particle parameters f, ν_g, R_c, R_g, G_g, to state parameters cn and σ and to time t. This allows studying the development of G_{eff} in the case of creep as a function of only time t.

6.3.4 Validation

In order to validate the model in Equation 6.8 and to verify the capability of the coda wave interferometry, the influence of confining pressure on shear wave velocity, v, was examined experimentally. For this purpose, an artificial material was used to study this effect with bender elements. This material is uniform glass beads with a diameter of 3.5 mm and a specific gravity of 2.5. Other properties of this material are described in Table 3.1. Since the glass beads are uniform, the redistribution that may take place while pressure increases is negligible. Figure 6.24 demonstrates the change in velocity for the range of confining pressure between 10 kPa and 400 kPa. The confining pressure was increased in 5 kPa intervals. At each pressure step, a sinus wave with a frequency of 3 kHz was excited in the specimen. This frequency was chosen because it gave the largest amplitudes, which means longer coda parts that improve the accuracy of the method. The velocity change was calculated between every two consecutive pressure steps and then accumulated over the whole pressure range. Velocities were normalized to the initial velocity at 10 kPa confining pressure. Each point in Figure 6.24 represents the normalized velocity at the end of that pressure step, i.e., $v_{norm} = 1 + (\delta v)_{acc}$, where v_{norm} is the normalized velocity and $(\delta v)_{acc}$ is the accumulated velocity change. The accumulated velocity change between 10 kPa and 400 kPa was 75.4 %. In a logarithmic scale, the change appears to be a straight line, which can be represented as a power function. The exponent of that power function was found to be 0.152. From Equation 6.8 and knowing that $G = \rho v^2$, where ρ is the medium density, the predicted theoretical exponent for the relationship between v and σ is 1/6=0.167. Therefore the exponent determined experimentally in this test came very close to the theoretical one. This confirms the assumptions made for the model and the coda wave interferometry.

The same test was done on Hostun sand to verify the previous findings for natural soil. A specimen of dry Hostun sand were tested in the same conditions as of glass beads. Figure 6.25 shows the normalized velocity of shear waves versus confining pressure for the range between 10 kPa and 400 kPa. The confining pressure was increased in 5 kPa intervals. Calculating normalized velocities at each pressure follows the procedure explained above. The accumulated velocity change between 10 kPa and 400 kPa was 76.2 %. Accordingly, the exponent relating velocity to confining pressure was 0.153 with coefficient of determination

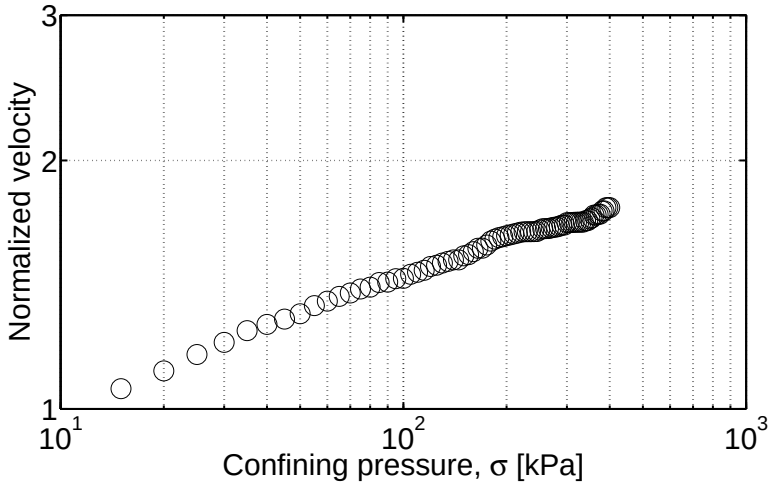

Figure 6.24: Normalized velocity for glass beads versus confining pressure

$R^2 = 99.9$ %. As with the glass beads, the relationship between velocity, or shear modulus, and confining pressure for this natural soil follows the predicted value in Equation 6.8 very closely.

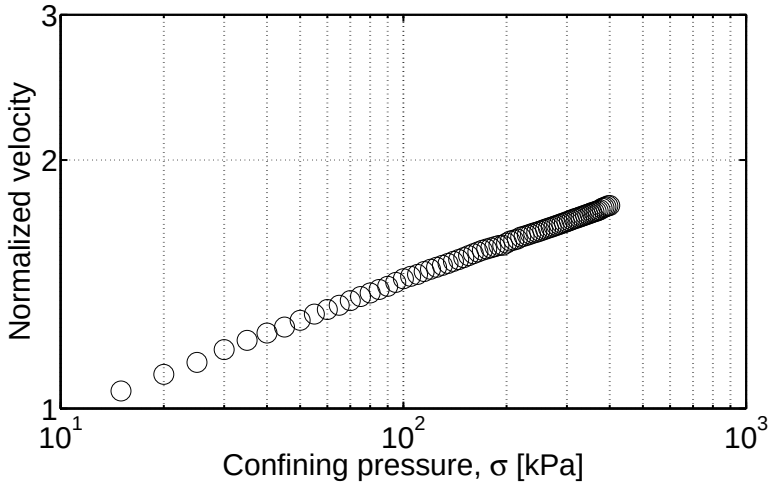

Figure 6.25: Normalized velocity for Hostun sand versus confining pressure

The arrival time of different parts of the signals recorded while loading the specimen of Hostun sand is demonstrated in Figure 6.26. Signals of 79 shear wave measurements between 10 kPa and 400 kPa were normalized to their highest amplitudes and stacked. It is readily seen in the figure that changes in waves are minimal in the main part, especially in high pressures. On the other hand, in the coda parts of the waves, certain peaks and troughs can be easily followed through

the whole pressure range. Such wave characteristics can be traced, for example, between the two solid lines in Figure 6.26. The solid lines represent arrival time change for that part of the wave. Their relationship with confining pressure, σ, appears to be a power function. Since the change in the specimen's length is considered negligible as discussed later in this section, the change in time equals the change in velocity. Therefore velocity change has a power relationship with pressure as suggested by the theory. This demonstration shows once more that the coda wave interferometry is a powerful tool to detect the slightest changes in a medium.

The changes in density and travel length need to be addressed. For the specimen of dry Hostun sand with an initial volume of 1589 cm^3, volume change over pressure range between 10 kPa and 400 kPa was 37.1 cm^3. Thus the total apparent volume strain measured is $\epsilon_{total} = 2.3$ %. This volume change was measured with a burette that is connected to cell water. This volume change includes two error sources: cell expansion and membrane penetration:

$$\epsilon_{total} = \epsilon_{specimen} + \epsilon_{cell} + \epsilon_{membrane} \tag{6.19}$$

where $\epsilon_{specimen}$ is volume strain of the specimen, ϵ_{cell} is volume strain in cell water due to cell expansion and $\epsilon_{membrane}$ is volume strain in cell water due to membrane penetration into the specimen. The used cell was calibrated for the range of pressure used in this research. During the calibration, the cell was filled with fresh de-aired water, and a steal dummy was used to fill the specimen volume. The volume change in the cell after applying a pressure of 400 kPa was $V_{cell} = 23\ cm^3$, therefore $\epsilon_{cell} = 1.4$ %. Cell expansion due to creep and water absorption into the cell wall can be neglected because test time was relatively short. Membrane penetration occurs when the flexible latex membrane penetrates in between sand particles when confining pressure rises. This causes an error in the reading of the water cell burette. To correct for this effect, Baldi & Nova [1984] proposed the following equation:

$$\epsilon_{membrane} = \frac{d_{50}}{2D}\left[\frac{d_{50}\sigma_3}{t_m E_m}\right]^{1/3} \tag{6.20}$$

where d_{50} is mean particle diameter, D is specimen diameter, σ_3 is lateral pressure, t_m is membrane thickness and E_m is Young's modulus of membrane material. For the test at hand, $d_{50} = 0.33\ mm$, $D = 100.2\ mm$, $t_m = 0.9\ mm$ and a typical value for E_m in the literature is 1350 kPa [Baldi & Nova, 1984;

Omar & Sadrekarimi, 2014]. As a result $\epsilon_{membrane} = 0.08$ %. Then $\epsilon_{specimen} = \epsilon_{total} - \epsilon_{cell} - \epsilon_{membrane} = 0.85$ %. This volume change is directly related to density change. Since $G = \rho v^2$, then $\Delta G \approx 0.85$ %. The approximation comes from the fact that density change affects velocity also. The velocity change during the test was found to be 76.2 %, as shown in Figure 6.25, consequently $\Delta G = 152.4$ %. This means that shear modulus change due to densifying of the specimen during the test is very small compared to shear modulus change due to interparticle pressure increase.

Assuming isotropic volume change, $\epsilon_z = \epsilon_{specimen}/3 = 0.28$ %, where ϵ_z is vertical strain. This results in velocity change due to travel length change equals to 0.28 %. This is also very small compared to the measured velocity change of 76.2 %. Conclusively, both effects are insignificant and can be neglected. Therefore, the assumption made for the coda wave interferometry that velocity change is caused only by fabric change is valid.

The coda wave interferometry helps determine the velocity change for a given fabric change in the medium, but it does not provide any information about the absolute velocity. To validate the model in Equation 6.8, absolute velocities and corresponding absolute shear moduli have to be known. Two methods of time domain analysis, first arrival and cross correlation, were considered. Shear moduli in both methods were calculated at different pressure steps for the Hostun sand specimen. Figure 6.27 shows shear moduli calculated with these two methods and theoretical modulus from Equation 6.8. For the theoretical G_{eff} the following values were considered as discussed previously: $f = 0.55$, R_c/R_g=0.31, $cn = 8$ and $n = 0.40$. Shear modulus for quartz is provided by Mavko et al. [2009] and Carmichael [1989], $G_g = 44\ GPa$. Carmichael [1989] also provided compression wave and shear wave velocities for quartz minerals, $v_p = 6.05\ km/s$ and $v_s = 4.09\ km/s$, from which Poisson's ratio, ν_g, can be calculated, $\nu_g = 0.5(v_p^2 - 2v_s^2)/(v_p^2 - v_s^2) = 0.08$. Values for G_{eff} range from 104 MPa at 10 kPa to 355 MPa at 400 kPa. Values obtained by means of first arrival method and cross correlation method are also shown in Figure 6.27. It is evident that first arrival method results in the closest values to the theoretical ones. Cross correlation provides very small values compared to the other two curves. Cross correlation measures the similarity between two signals. It is a measure of the part of the output signal that contains the highest energy, which

arrives significantly later that the first deviation from zero. Therefore it is merely an assessment of the presence of the input frequency in the output signal and does not necessarily represent travel time. It was shown in the literature that cross correlation between the input and output signals are theoretically inaccurate (e.g., [Arulnathan et al., 1998]).

The first arrival is also coupled with some problems. The main problem is the near field effect, which was first theoretically proposed by [Sanchez-Salinero, 1987] and experimentally proven by many researchers (e.g., [Brignoli et al., 1996] and [Jovičić et al., 1996]). Jovičić et al. [1996] recommended increasing the ratio of d/λ, where d is the distance traveled and λ is the wave length of the transmitted signal, to avoid the near field effect. Youn et al. [2008] showed that when $d/\lambda > 2$, the near field effect can be ignored. Low excitation frequencies of 1 kHz and 2 kHz were avoided for this reason. For the tests performed in this research, excitation frequencies between 3 kHz and 10 kHz were used, and the near field effect was not observed in this range. All excited frequencies gave very similar first arrival velocities. It was also found by many researchers that the first arrival method has very good agreement with resonant column and torsional shear tests [Dyvik & Madshus, 1985; Brignoli et al., 1996; Ferreira et al., 2007; Youn et al., 2008].

The starting point of the coda wave gradient can be taken as the velocity at 10 kPa by means of the first arrival method. This gradient can be added to the initial velocity to get the absolute velocity over the whole pressure range. Knowing the density of the sample, the shear modulus is calculated and presented in Figure 6.28. The theoretical shear modulus from Equation 6.8 is also shown in Figure 6.28. Both theoretical and measured values of shear moduli show very good agreement. Using this approach eliminates the instability of methods that depend on the main part of the signal. These methods, whether in time or frequency domain, rely on the firstly arrived vibrations that contain limited information. Whereas the coda wave extracts velocity variations from the scattering medium. When combining the coda wave interferometry with only one determined absolute velocity, velocities for the whole studied range can be specified.

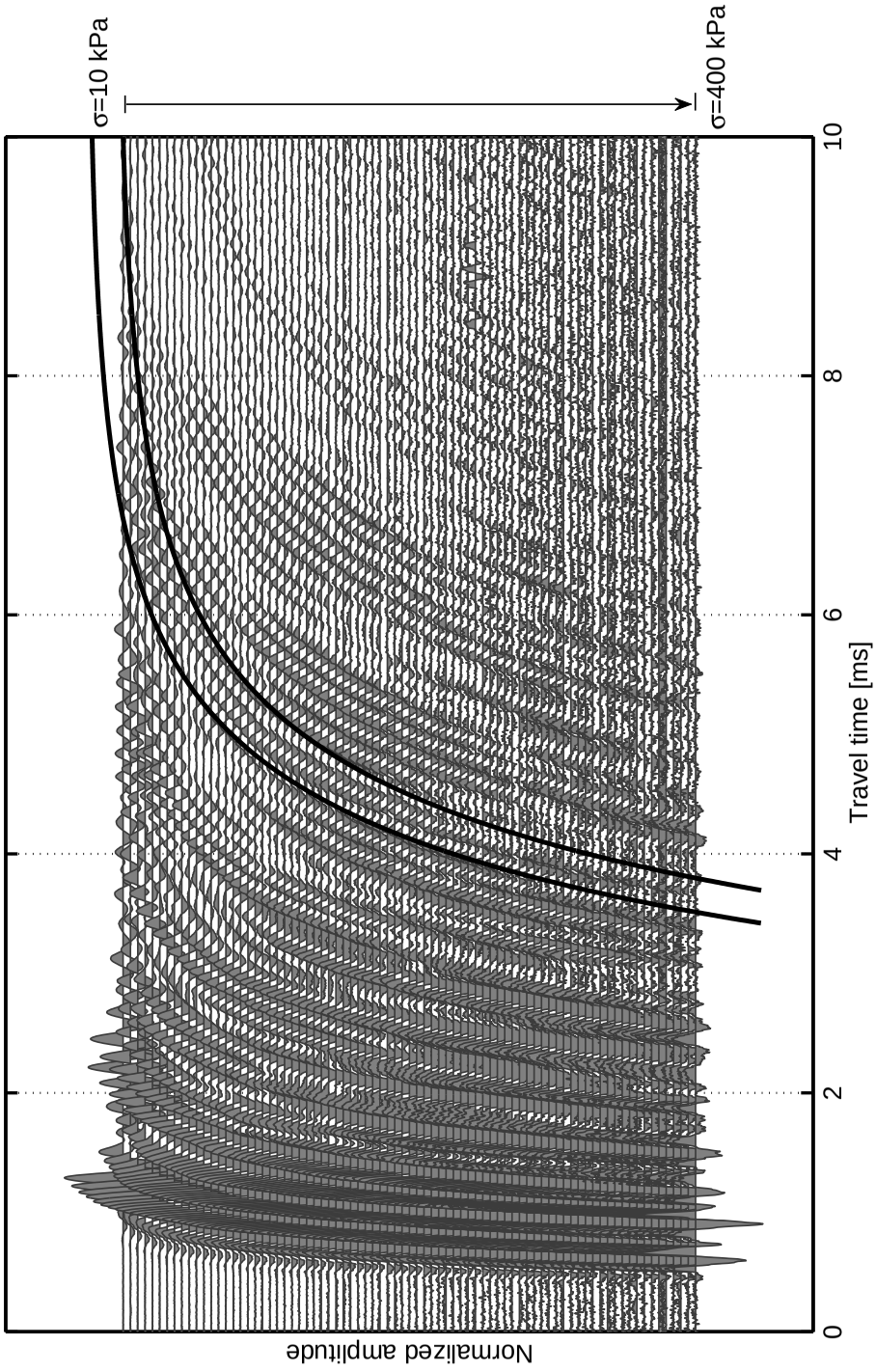

Figure 6.26: Cascade of 79 shear wave measurements on dry Hostun sand during loading from 10 kPa to 400 kPa

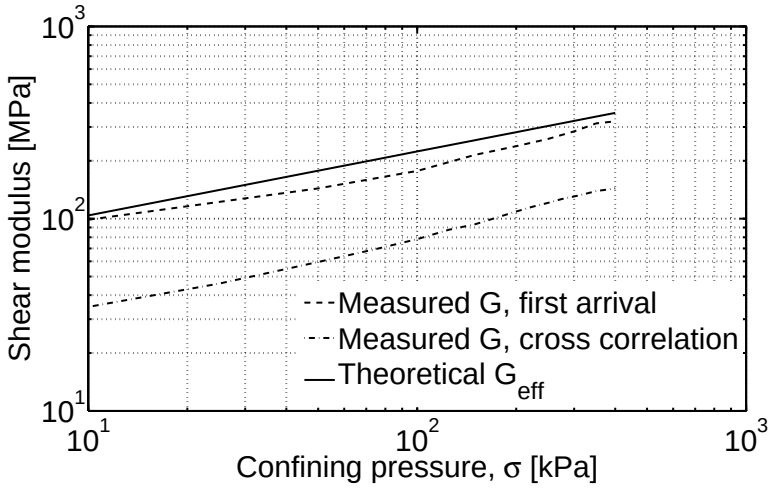

Figure 6.27: Theoretical and measured Shear moduli for Hostun sand

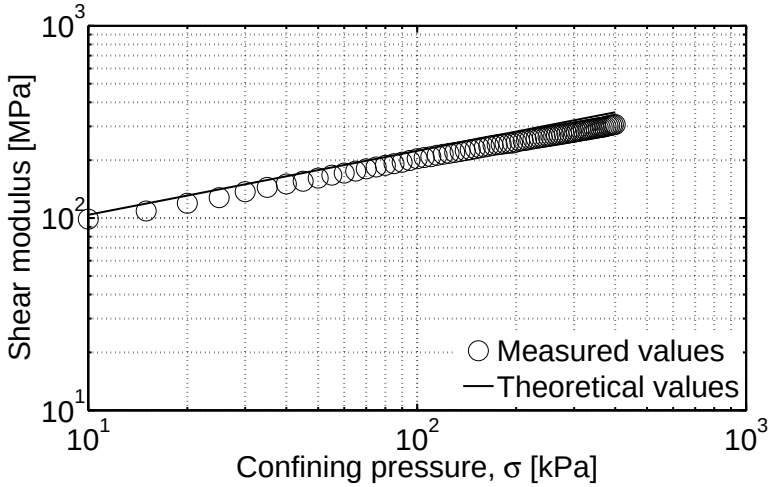

Figure 6.28: Measured Shear modulus based on velocity gradient and theoretical one for Hostun sand

The previous analysis demonstrates that the theoretical values of shear modulus from Equation 6.8, where friction, angularity and coordination number were taken into account, explain the experimental data very well. The coda wave interferometry provides a very precise method to monitor velocity change in the medium due to any perturbation, like pressure change. When combined with the first arrival method, coda wave is capable of determining velocity, and thus shear modulus caused by fabric changes due to perturbations in complex inhomogeneous media, such as pressure, moisture, temperature and creep.

6.4 Discussion and micromechanical explanation

Figure 6.29 compares the accumulated velocity gradient during the 8-hour creep phase for Hostun sand with all tested degrees of saturation. The velocity gradient for the degree of saturation $S = 0$ % is distinguishably higher than for all other degrees of saturation. The velocity change at the end of the creep phase was as high as 1.25 %. Shear modulus development during the creep phase is presented in Figure 6.30. The shear modulus is normalized to its initial value at $t = 0$. The curve follows the trend proposed by the model in Equation 6.14, i.e., it is proportional to $(t/t_{ref})^{(1-\beta)/2}$. The exponent $(1-\beta)/2$ was found to be 4.3x10^{-3} for this test. That means exponent $\beta = 0.9914$. The theoretical line in Figure 6.30 has a good agreement with the measured values with a coefficient of determination $R^2 = 92$ %. When $\beta = 1$, then $(1-\beta)/2 = 0$ and velocity and shear modulus are completely independent of time. The lower β (higher $(1-\beta)/2$) the stronger is the dependency.

Relationships between velocity change and time are examined in Figure 6.31. The trend for degrees of saturation between 19.7 % and 100 % looks very similar to the one of $S = 0$ % but less prominent, suggesting less dependency of velocity on time. β for these tests ranges from 0.9947 ($(1-\beta)/2 = 2.65$ x10^{-3}) to 0.9972 ($(1-\beta)/2 = 1.42$ x10^{-3}) with good to excellent agreement (88 % $< R^2 <$ 97 %). The results are listed in Table 6.3. Figure 6.33 demonstrates the relationship between exponent $(1-\beta)/2$ in Equation 6.18 and S. For $S = 0$ %, $(1-\beta)/2$ is more than double the average value for other S-levels. For values of S between 19.7 % and 100 %, $(1-\beta)/2$, and thus β does not change much.

After confining pressure is applied, the specimen starts to show creep immediately. The greatest amount of creep occurs at the beginning. After that, as time progresses, creep slows down, indicating a time strengthening behavior. Therefore the Model proposed in Equation 6.15 is valid. This slowing of creep rate with time agrees with the literature [Lade et al., 2009; Kang et al., 2012; Gao et al., 2013].

Aging effects in sands may be explained by chemical processes that involve interparticle cementation. Cementation may increase cohesion between particles. For Cementation, moisture is required as a solution for the reactions responsible

for creating the bonds between particle. This is why cementation is unlikely in dry sand. A chemical process needs a course of days or weeks to make measurable changes in the fabric of sand. Therefore, for the short period of time in experiments in this research, namely 8 hours, cementation does not have the required time to occur. This agrees with the literature that cementation is unlikely for short periods of time [Mitchell & Soga, 2005]. It was also stated by many researchers that in sands, a chemical processes, such as cementation, may not be responsible for increasing stiffness, and another mechanism might be involved [Mesri et al., 1990; Wang & Tsui, 2009].

The increase in stiffness cannot be attributed to a decrease in void ratio, as argued by Leonards & Altschaeffl [1964]. In fact, fabric change during creep may be different from that caused by increasing stress [Leroueil, 1996]. For two samples with identical void ratios, creep and stress result in different force chain distributions [Wang et al., 2008]. Creep redistributes the contact forces causing force chains to become more stable and homogenized. In their numerical simulation, Wang et al. [2008] found that both the magnitude and spatial distribution of force chains become more uniform. Wang et al. [2016] directly measured the distribution of force between weak and strong chains by means of a tactile pressure sensor that has thousands of micro load cells. They found that during creep redistribution of force occur by which weak force chains gradually gain force from stronger force chains resulting in a more homogeneous distribution. This new distribution strengthens the soil structure causing the stiffness to increase. The redistribution and rearrangement of soil structure involve also rolling and sliding of particles that lead to increased interlocking of particles and surface asperities [Mesri et al., 1990; Mitchell & Soga, 2005].

The presence of water appears to slow creep down in sand, as concluded from Figure 6.29 and Figure 6.31. Figure 6.32 demonstrates the influence of the degree of saturation on exponent $(1 - \beta)/2$ in Equation 6.18. A possible explanation is that lower water content corresponds to higher matric suction, which in return, signifies the stress concentration at the contacts. This is accompanied with a greater tendency for contact creep. This stress concentration at the contacts causes inequality in the distribution of force among different chains, i.e., the difference between strong and weak force chains in the magnitude of the carried force is larger. This leaves more space for redistribution and homogenization

that translates to more stiffness increase, i.e., more creep. The higher the initial inequality, the greater the stiffness gain, as proved by Wang et al. [2016] and Gao et al. [2013]. By comparing the dry and the saturated specimens in Figure 6.31, which have an identical dry density of 1.61 g/cm^3, it was found that creep in the dry specimen is greater than in the saturated one. This agrees with what Baxter [1999] found for silica sand. For these two specimens, the only changing factor is water. This shows that the presence of water decreases the creep rate significantly. The experimented specimens varied slightly in dry density between 1.51 g/cm^3 and 1.61 g/cm^3. This variation comes from the compactability of sand with different water contents during preparing the specimens and was inevitable. Although all wet specimens that have degrees of saturation between 19.7 % and 100 % vary a little in dry density, they show very similar creep rates. This means that the presence of water, even for low water contents, plays a bigger role than the experimented variation in density.

Strain rate during applying of confining pressure has no influence on the creep rate as proved by Augustesen et al. [2004] and Lade et al. [2009]. Baxter [1999] found very little effect of temperature between 25° and 40° on the time-dependent increase in small strain shear modulus. Although the temperature in the laboratory was not controlled in this research, the 8-hour creep experiments were assumably too short for any significant temperature change to take place. The range of changing temperature was certainly less than the above-mentioned 15° range and, therefore, the influence of temperature can be neglected.

The previous analysis shows that the experimental data of pressure and creep can be modeled using Equation 6.18. The development of small strain stiffness due to an increase in confining pressure and time for dry Hostun sand is demonstrated in Figure 6.33.

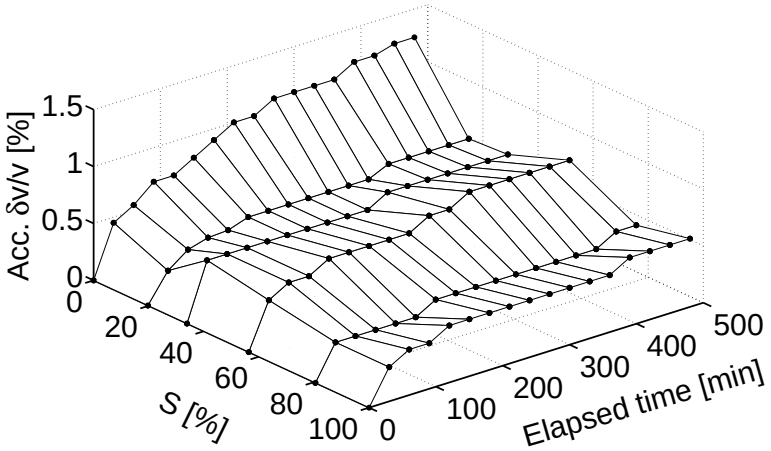

Figure 6.29: Accumulated velocity gradient during the 8-hour creep phase for Hostun sand with different degrees of saturation

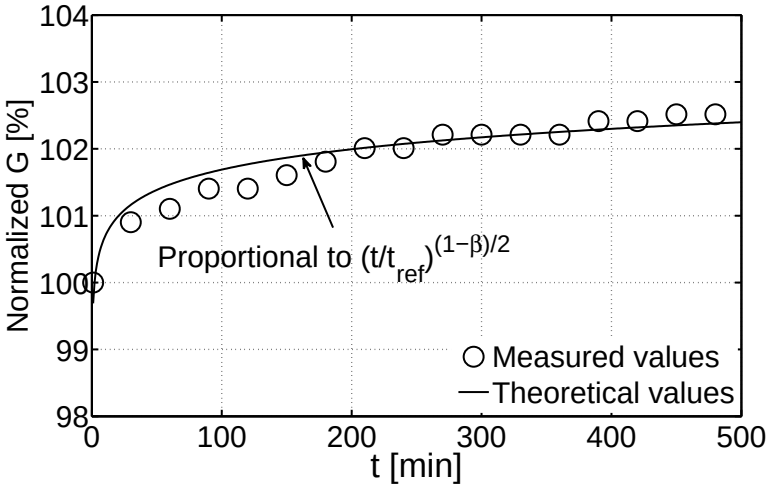

Figure 6.30: Measured Shear modulus and theoretical one after Equation 6.18 during creep for dry Hostun sand

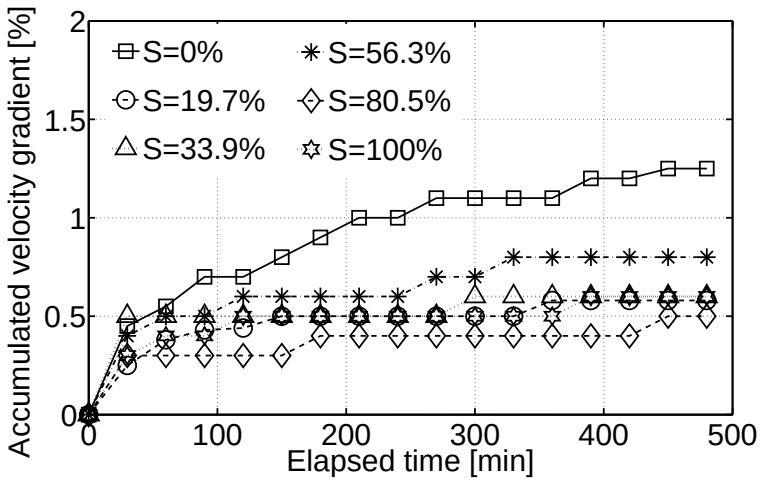

Figure 6.31: Accumulated velocity gradient during 480 min creep for different degrees of saturation

Table 6.3: Modeling parameter β in Equation 6.14 and coefficient of determination R^2 for all creep tests

S	$(1-\beta)/2$ x10^{-3}	β	R^2
0 %	4.298	0.9914	92 %
19.7 %	1.926	0.9962	97 %
33.9 %	1.754	0.9965	88 %
56.3 %	2.650	0.9947	95 %
80.5 %	1.416	0.9972	90 %
100 %	1.881	0.9962	95 %

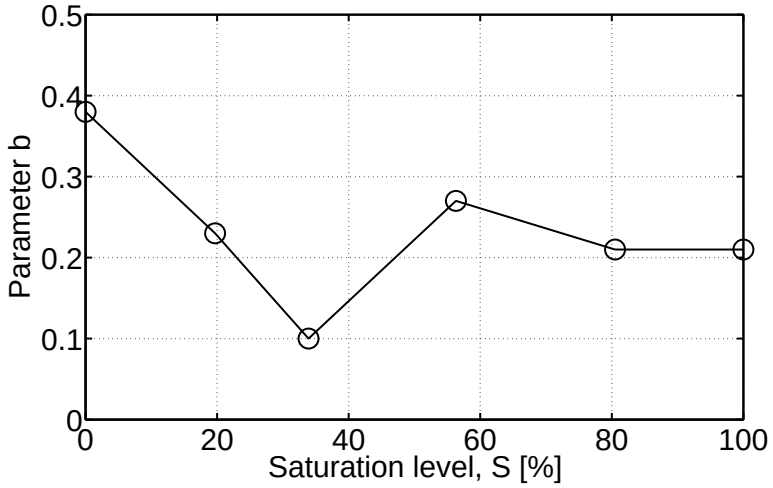

Figure 6.32: Exponent $(1-\beta)/2$ in Equation 6.18 versus degree of saturation

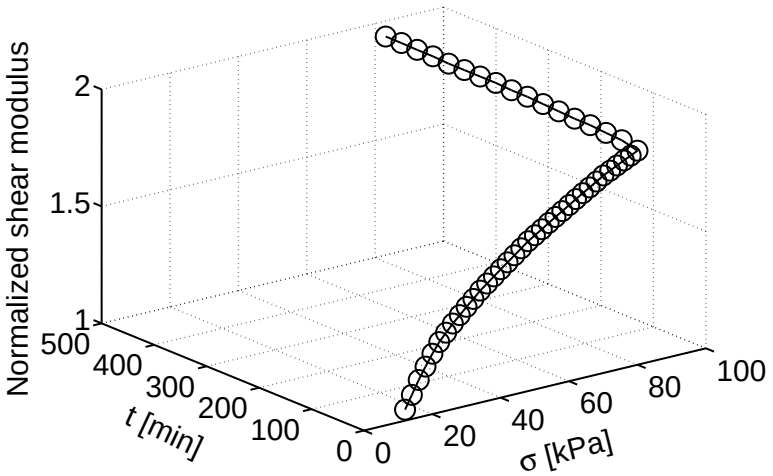

Figure 6.33: Normalized measured Shear modulus during pressure and creep for dry Hostun sand

6.5 Summary

An experimental and theoretical study has been presented to investigate creep behavior in Hostun sand. The influences of friction, angularity and packing were investigated. Finally, a model was introduced that includes a variable for time. The experimental data were explained by the model well. The findings of this chapter can be summarized as follows:

- Interparticle friction value can be derived from macro scale shear strength. Friction, f, is directly linked to critical state angle, Φ_{cv}. Value of friction of 0.55 was calculated for Hostun sand. For a different sand, two approaches to estimate friction are suggested in Section 6.3.1.
- The angularity of the particles is considered in the model and calculated for Hostun sand. It was found to be 0.31. Neglecting angularity will result in an overestimation of the velocity of 22 % and of the shear modulus of 48 % for this sand.
- For a cubical tetrahedral array of packing, a model that relates macro scale shear stiffness G_{eff} to particle parameters f, ν_g, R_c, R_g, G_g, to state parameters cn and σ and to time t. This allows studying the development of G_{eff} in the case of creep as a function of only time t (Equation 6.18).
- Coda wave interferometry was proved to be a powerful tool in detecting the slightest changes in a medium, such as a velocity increase due to creep.
- It was found that velocity values obtained by the first arrival method fit theoretical values very well.
- Creep has the highest rate in the dry specimen. The presence of water appears to slow creep down. The micromechanical explanation for creep and for the effect of water is presented in Section 6.4.

Chapter 7

Evolution and Predicting of Shear Stiffness in Unsaturated Soils

7.1 Introduction

This chapter presents an experimental and theoretical investigation of the shear wave velocity in unsaturated soils. Bender elements were used to excite and receive shear waves in controlled unsaturated conditions to determine the dependency of shear wave velocity on matric suction. The modified unsaturated cell, specially designed for this research, was used to control two stress state variables, the net confining pressure and the matric suction, and to excite signals with installed bender elements. The specimen starts at full saturation then it dries gradually while matric suction increases. In each test, the net stress was kept constant, and time histories of shear waves were saved for each matric suction step. Coda wave interferometry was used to detect fabric change in the soil. A predictive relationship based on semi-empirical or alternatively numerical approaches that describes the change in shear wave velocity with matric suction or degree of saturation is presented. In the semi-empirical approach proposed here, analytical models that link shear wave velocity to matric suction or degree of saturation based on experimental data are derived. Additionally, a more general numerical approach that generates a medium based on the grain size distribution and the void ratio is described and used in the absence of experimental data. The analytical models associated with the numerical approach allow predicting

change in shear wave velocity based on easy to obtain soil properties. The validation of these approaches with new data from this research and data from the literature shows good agreement.

7.2 Results and analysis

Shear wave measurements were taken at each step of matric suction, $u_a - u_w$, during the tests. For Hostun sand under net stress, $\sigma - u_a$, of 100 kPa, measurements were taken after applying matric suction steps, 0, 1, 2, 4, 8, 10 and 20 kPa. These measurements are normalized to their maximum amplitude and cascaded in Figure 7.1. This cascade includes 18 signals throughout the test. After applying a matric suction step, shear wave measurements were taken regularly until equilibrium was reached. In Figure 7.1, post-equilibrium and intermediate signals are demonstrated. It is clear that signals do not show almost any change in the main part of the signal indicated by window *i*. Signals in that part are almost identical and coincide with each other. No change in time arrival can be detected. On the other hand, in the coda part, indicated by window *ii*, the signals arrive earlier as the test progresses, suggesting an increase in shear wave velocity. This change increases as later parts of the coda arrive. Such a small change in velocity can be accurately determined by using the coda wave interferometry method. By having clear and long time histories, any change that is detected in the latter parts of the coda component indicates a velocity change in the medium. All measurements were repeated and stacked in order to increase the signal-to-noise ratio.

After applying a matric suction step, a period of time passed before equilibrium was reached. During this time, shear wave measurements were taken regularly. In Figure 7.2, 9 shear wave measurements were taken after increasing matric suction from 2 kPa to 4 kPa on Hostun sand with net stress of 100 kPa. In the main part of the signals, indicated by window *i*, no change in arrival time can be detected. By moving to the right on the x-axis, a slight shift between signals can be recognized, as in window *ii*. This cascade shows once again that the coda wave interferometry method can detect even such small changes within one suction step in these tests. Figure 7.3 shows two consecutive measurements after 4 and 5 days of applying matric suction of 2 kPa to Hostun sand under net

stress of 100 kPa. The figure shows almost identical signals in the main part. Any change in shear wave velocity cannot be determined in any conventional method that deals with this part of the signal.

In the doublet technique of the coda wave interferometry, the time history is divided into a number of windows, in which time shift between two signals, before and after perturbation, can be calculated. Figure 7.4 shows a time shift for each window over time history for Hostun sand with net stress of 100 kPa after increasing matric suction from 4 to 6 kPa. The width of the windows was adjusted carefully to have optimal results. Using narrow windows results into instability in the cross correlation calculations, while using wide windows involves more averaging of time shift inside the window in addition to having fewer values to calculate the slope inclination from. Typically in this research, 7 to 10 time windows, each about 2 ms wide, were used to analyze a time history.

The inclination of the slope $\theta = -\delta t/t$ in Figure 7.4 can be calculated by dividing time shift over the central time of each window. The inclination θ represents velocity gradient $\delta v/v$. Figure 7.5 demonstrates the value of inclinations for all considered windows, which is averaged over the whole travel time. For this example of Hostun sand with 100 kPa net stress, increasing matric suction from 4 kPa to 6 kPa caused velocity to increase by $\theta = 0.00357 = 0.357$ %. So if shear wave velocity was 200 m/s at matric suction 4 kPa, for instance, an increase of about 0.7 m/s was determined at 6 kPa. This exhibits clearly the high accuracy of the coda wave interferometry method in detecting such minute change in the studied medium.

Figure 7.6 shows the velocity gradient and its accumulated value for Hostun sand at net stress of 100 kPa throughout the test, where matric suction increased from 0 kPa to 20 kPa. The standard deviations resulted from averaging the slope inclination $\theta = \delta v/v$ in Figure 7.4 are shown in Figure 7.6 as error bars. Shear wave velocity starts to increase at 2 kPa showing an increase of 1 %. At 4 kPa, the velocity gradient reaches its peak with 3.6 % then it decreases dramatically till reaching 0 % at 10 kPa. The accumulated gradient shows clearly that all the change takes place between 2 kPa and 8 kPa.

The stretch technique of the coda wave interferometry considers another ap-

proach to calculate the change in compared signals, as explained in Section 4.4. The faster signal is stretched gradually and cross correlated with the slower signal. For each $\theta - value$, cross correlation is calculated. The $\theta - value$ that returns the highest correlation is considered the velocity gradient between these two signals. The signals are multiplied with the amplification function $e^{\alpha t}$ to over come the bias in cross correlation towards the higher amplitudes at the beginning of the signal. Figure 7.7 demonstrates velocity gradients $\delta v/v$ for Hostun sand at net stress 100 kPa with and without amplification after increasing the matric suction from 1 kPa to 2 kPa using this technique. The figure signifies the help amplification offers in finding the peak of the curve since the stretching curve without amplification is more flat. The factor α was typically in the range of 0.3 to 0.5 for the tests in this research. Both curves have peaks that are typically close to each other. In this example, the peaks coincide with each other. Using amplification is more accurate, and the peak of its curve is easier to locate.

Figure 7.8 compares the stretch technique and the doublet technique of the coda wave interferometry after increasing the matric suction from 1 kPa to 2 kPa. The cross correlation of the stretch technique is plotted against values of $\theta = \delta v/v$ between 0 % and 4 %, while the velocity gradient of the doublet technique is presented with its standard deviation. Both techniques result in very similar values.

The sliding window technique, as explained in Section 4.5, was considered here to avoid the problems associated with existing techniques in calculating the interferometry, as discussed in Chapter 4. This technique can detect a time shift between two signals in a reliable, stable way (see Section 4.6). A single window is considered. This window should be wide enough to have a good representation of the correlation within it. The window is then slidden along the time history. For each slide, the time shift from cross correlation is obtained. As a result, time shifts for all slidden windows along the time history are presented as in Figure 7.9. The number of time shifts is large enough to make deriving the inclination line more stable. A window width of about 2 ms and a slide step of about 50 μs gave satisfying results for the data in this research.

Accumulated velocity gradient for the whole matric suction range of the test on Hostun sand with net stress of 100 kPa is illustrated in Figure 7.10. It is evident that stretch, doublet and sliding window techniques reveal very similar

values over the whole test, 5.00 %, 5.13 % and 5.20 %, respectively. This similarity in results was confirmed in all tests in this research. The sliding window technique was found to be very stable and reliable, even at the presence of noise, as explained previously in Section 4.6. However, all techniques were cooperatively used to evaluate signals in this research, and they led to the same value most of the time. Whenever they delivered slightly different values, an average mean was calculated. Normalized shear wave velocities for Hostun sand at two net stress levels, 50 kPa and 100 kPa are plotted against matric suction in Figure 7.11. The velocities are normalized to their initial value at full saturation, i.e., zero matric suction. The figure indicates that most of the increase in velocity for Hostun sand occurs between 2 kPa and 4 kPa. After that, shear wave velocity shows a very slow increase.

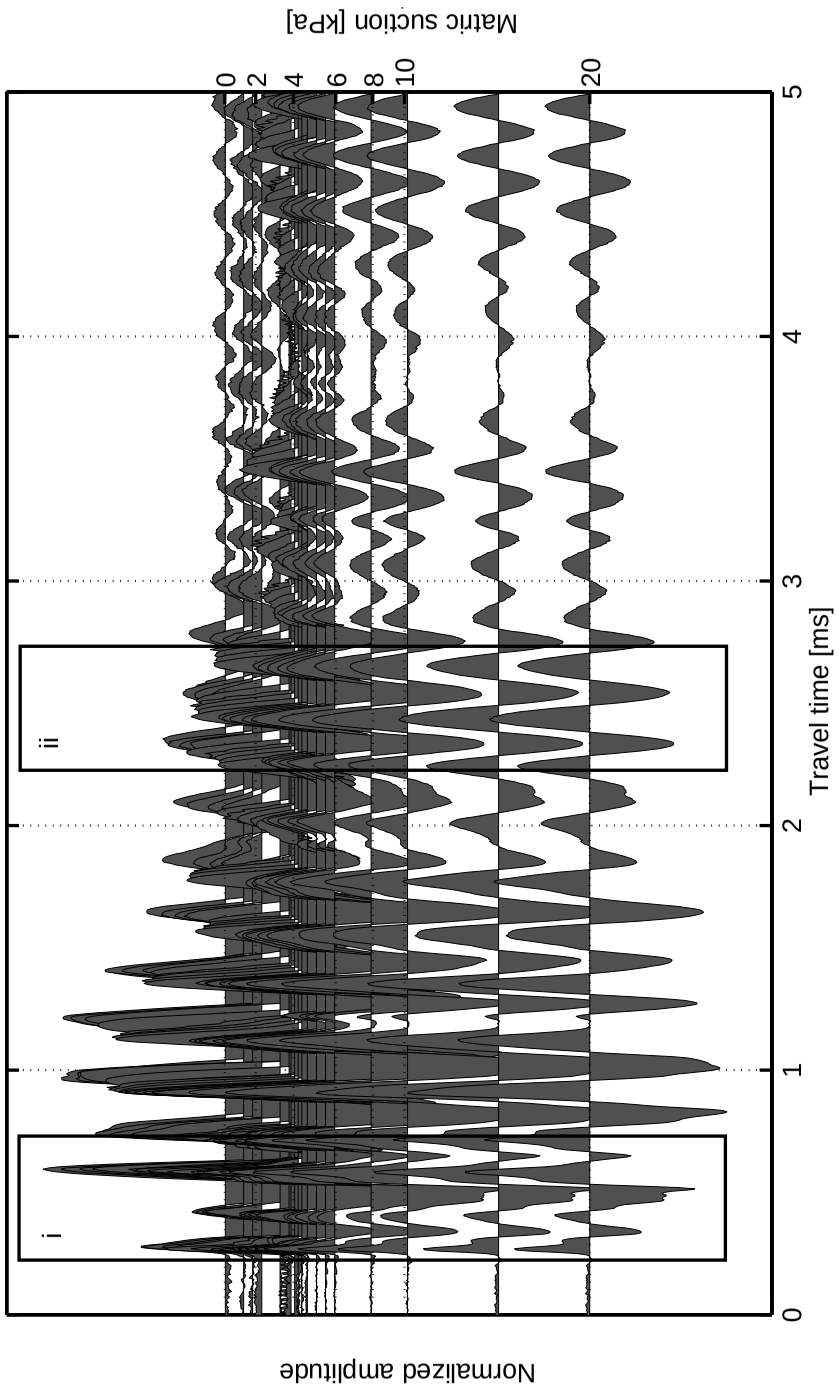

Figure 7.1: Cascade of 18 shear wave measurements on Hostun sand with net stress of 100 kPa with increasing matric suction

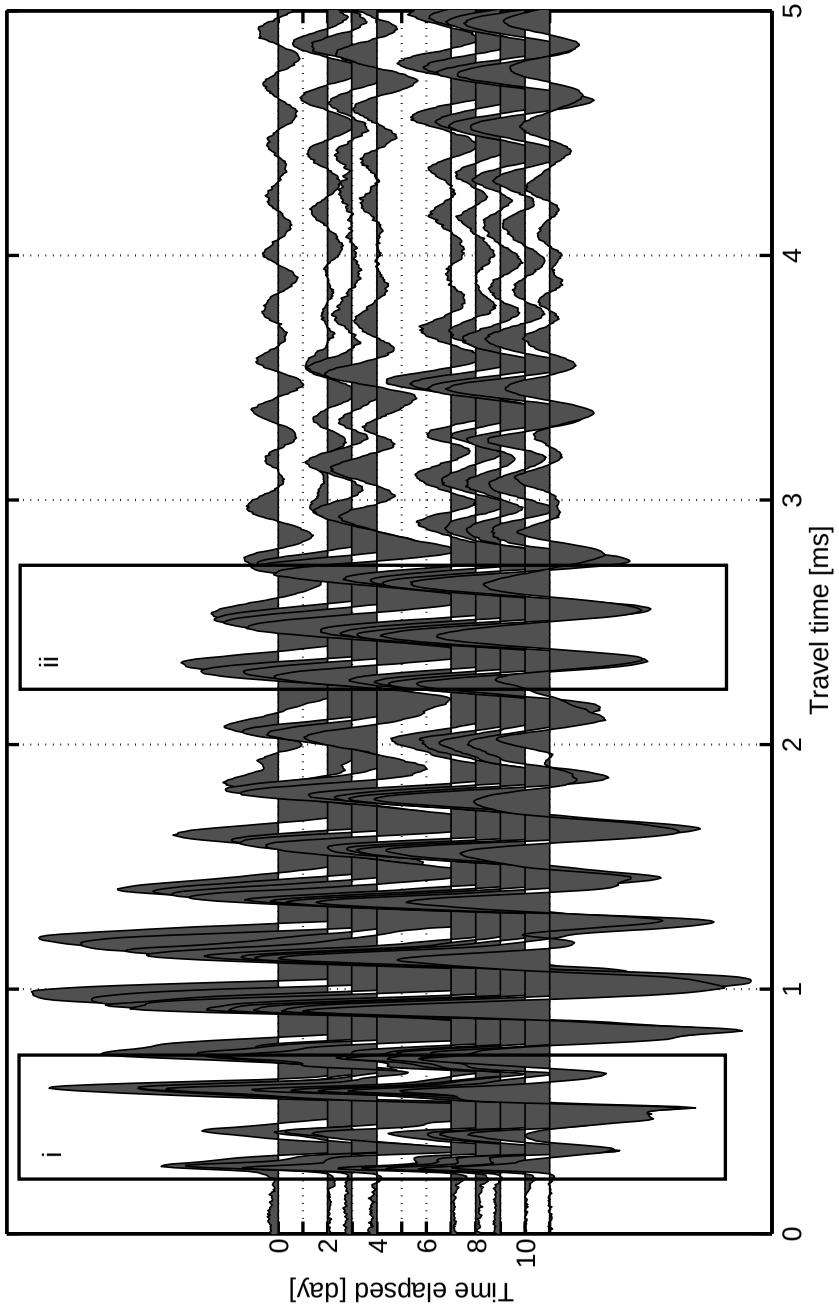

Figure 7.2: Cascade of 9 shear wave measurements on Hostun sand with net stress of 100 kPa after increasing matric suction from 2 kPa to 4 kPa during 11 days

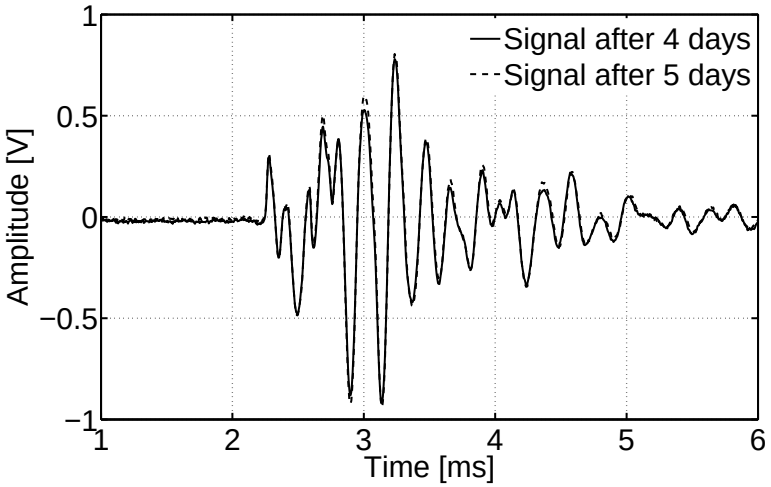

Figure 7.3: Signals after 4 and 5 days of applying a new matric suction step

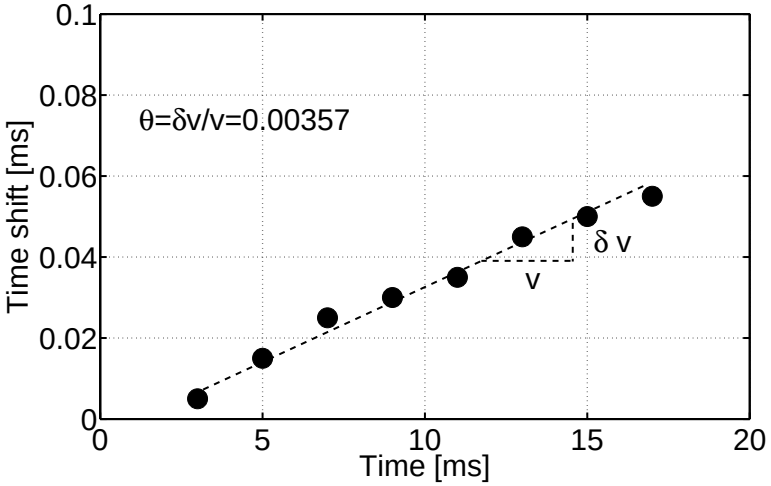

Figure 7.4: Time shift for each time window over time history for Hostun sand with net stress of 100 kPa after increasing suction pressure from 4 kPa to 6 kPa

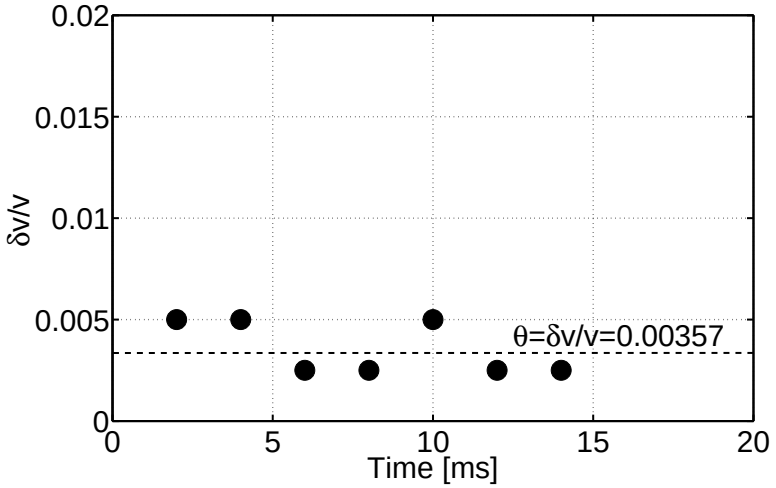

Figure 7.5: Velocity gradient for each time window over time history for Hostun sand with net stress of 100 kPa after increasing suction pressure from 4 kPa to 6 kPa

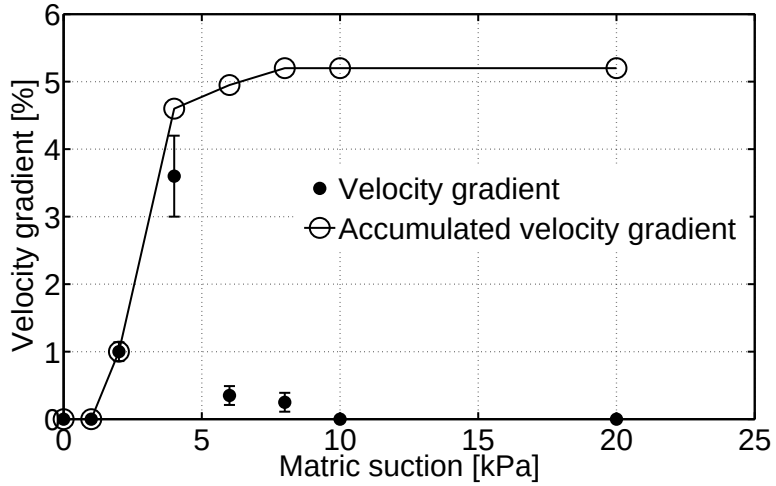

Figure 7.6: Velocity gradient with standard deviation and accumulated velocity gradient versus matric suction for Hostun sand at net stress 100 kPa

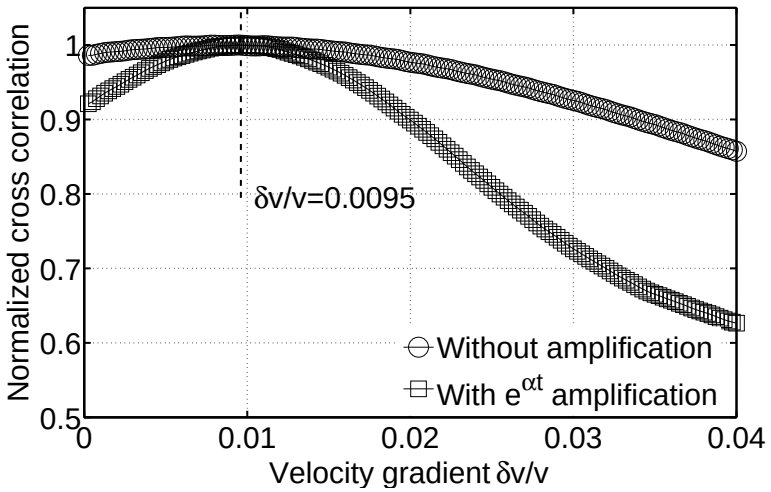

Figure 7.7: Velocity gradient $\delta v/v$ for Hostun sand at net stress 100 kPa with and without amplification after increasing the matric suction from 1 kPa to 2 kPa

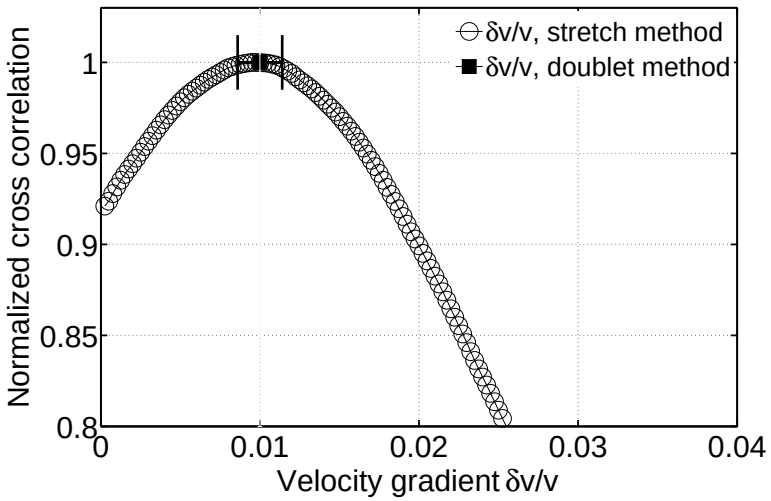

Figure 7.8: Velocity gradient $\delta v/v$ calculated with stretch technique and doublet technique with the standard deviation

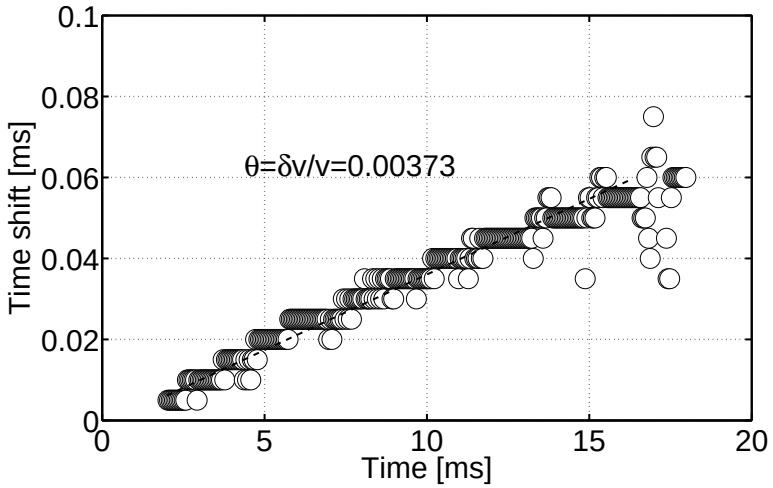

Figure 7.9: Time shift for slidden windows over time history for Hostun sand with net stress of 100 kPa after increasing suction pressure from 4 kPa to 6 kPa

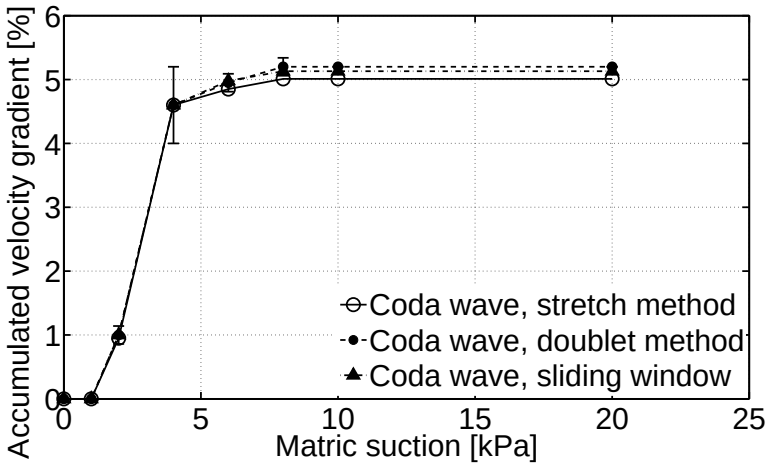

Figure 7.10: Comparison among different techniques for Hostun sand at net stress 100 kPa

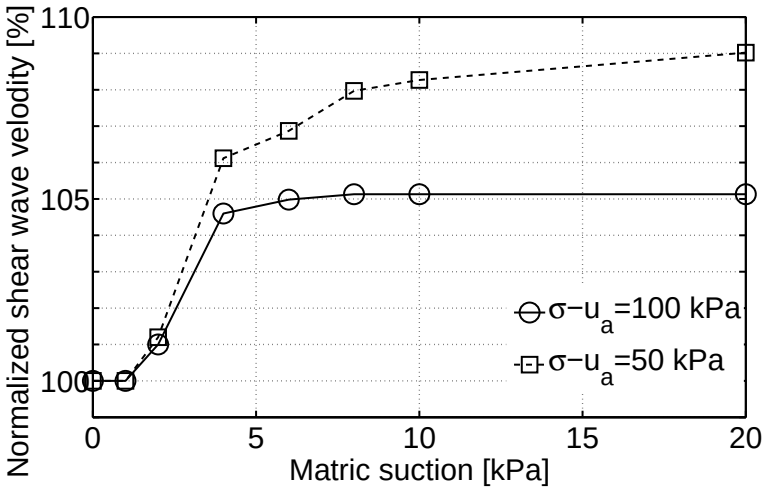

Figure 7.11: Normalized shear wave velocity versus matric suction for Hostun sand at two net stress levels, 50 and 100 kPa

7.3 Discussion

As demonstrated in the previous section, the maximum increase of shear wave velocity takes place between 2 kPa and 4 kPa. It is interesting to know that this occurs right after the air entry value (AEV), which is 1.8 kPa for Hostun sand. This observation is explicit in Figure 7.12, where the soil-water characteristic curve, SWCC, for Hostun sand is shown together with normalized shear wave velocity at 50 kPa and 100 kPa net stress. One can notice that velocity starts to rise around the air entry value. As the degree of saturation rapidly decreases, the velocity has its highest increment. Between 2 kPa and 4 kPa, where saturation drops from 92 % to 15 %, shear wave velocity increases 4-6 %, i.e., shear modulus increases 8-12 %. After this phase, the degree of saturation and shear wave velocity are relatively stable. It is evident that shear wave velocity increases with matric suction until residual water content, and it does not have a peak point at optimum water content. The optimum water content for this sand is 10 % that corresponds to about 40 % saturation. It is apparent in Figure 7.12 that shear wave velocity increases beyond the optimum water content. This is in agreement with many findings from the literature (e.g., Alramahi et al. [2010]; Hoyos et al. [2008] and Picornell & Nazarian [1998]).

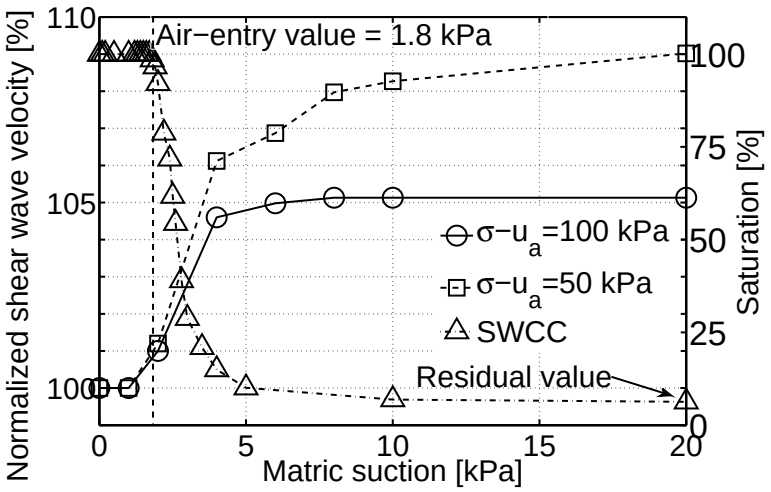

Figure 7.12: Normalized velocity at two net stress levels together with SWCC

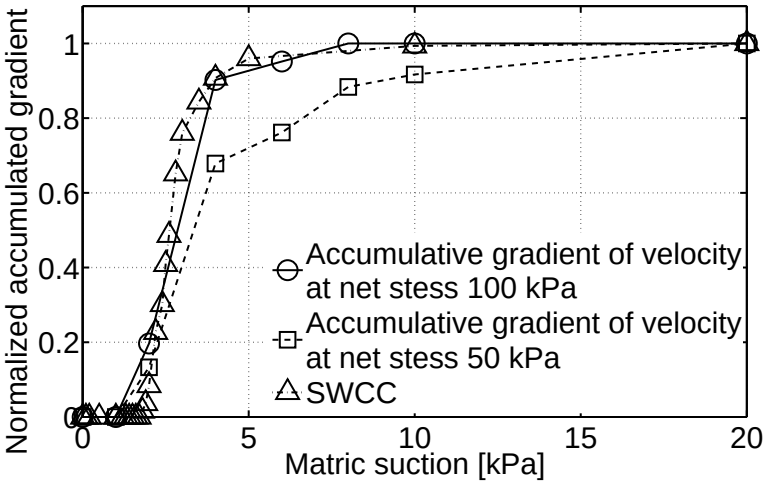

Figure 7.13: Normalized accumulative gradient of velocity and saturation

Accumulated normalized change in velocity, $\delta v_{acc}/v_{residual}$, for Hostun sand under both net stress levels is illustrated in Figure 7.13. It is normalized to its value at 20 kPa matric suction, $v_{residual}$. Additionally, change in the degree of saturation was derived from SWCC, then accumulated and normalized to its residual value, $\delta S_{acc}/S_{residual}$. Both curves display uniformity in shape and compare well to each other. This similarity suggests that the degree of saturation and velocity change with the same rate for a given change in suction. This means that the degree of saturation can be directly related to velocity as their accumulative changes with suction are similar.

7.4 Semi-empirical approach

7.4.1 Predicting shear wave velocity from SWCC

The increase in shear wave velocity depends on the soil-water characteristic curve, SWCC, as described in the previous section. The volume change during drying or wetting of soil is negligible for sand soils [Fredlund et al., 2012]. That means that the change in the void ratio can be ignored in investigating the variation of shear wave velocity. Velocity can then be linked to SWCC, which can be represented as an equation that describes specific characteristic values, like air entry value and residual water content. The objective here is to represent shear wave velocity by these characteristic values.

The curve of SWCC can be modeled with empirical equations. Van Genuchten [1980] provided a three-parameter equation to model the SWCC. The parameters can be obtained by fitting experimental data. This equation offers great flexibility to match a wide range of SWCC curves. The Van Genuchten equation is given as follows:

$$\theta = \theta_r + \frac{\theta_s - \theta_r}{[1 + (a_{vg}\psi)^{b_{vg}}]^{c_{vg}}} \tag{7.1}$$

where θ is volumetric water content at any soil suction, θ_s is saturated volumetric water content, θ_r is residual volumetric water content, ψ is soil suction and a_{vg}, b_{vg} and c_{vg} are fitting parameters. The residual volumetric water content, θ_r, is the water content where great suction change is necessary to remove additional water from soil. a_{vg} is related to air entry value and has the unit of kPa^{-1}. b_{vg} describes the slope of SWCC as soon as the air entry value is exceeded. c_{vg} is related to the residual value. Therefore all three parameters have a physical meaning related to properties in the unsaturated soil. Total soil suction, ψ, is considered equal to matric suction, i.e., $\psi = u_a - u_w$ because osmotic suction can be neglected in most geotechnical applications [Fredlund & Rahardjo, 1993]. Van Genuchten [1980] proposed that c_{vg} and b_{vg} are related, where $c_{vg} = 1 - 1/b_{vg}$, based on the model of Mualem [Mualem, 1976]. However, this dependency reduces the flexibility of Equation 7.1. It was found in this research that when c_{vg} and b_{vg} are independent of each other better results were obtained. Fredlund et al. [2012] also recommended considering independent parameters. Therefore, the independent-parameter version of the Van Genuchten equation is considered in this research.

Fredlund & Xing [1994] proposed a three-parameter equation to fit laboratory data of SWCC, that provides a correction for high suction values that gives a zero water content for suction of 10^6 kPa. This value is considered the upper limit for soil suction [Fredlund et al., 2012]. The Fredlund and Xing equation is given as follows:

$$\theta = C(\psi)\frac{\theta_s}{\{ln\,[e + (\psi/a_f)^{b_f}]\}^{c_f}} \tag{7.2}$$

where

$$C(\psi) = 1 - \frac{ln(1 + \psi/\psi_r)}{ln(1 + 10^6/\psi_r)} \tag{7.3}$$

where θ is volumetric water content at any soil suction, θ_s is saturated volumetric water content, e is the base of the natural logarithm and equals to 2.718, ψ is soil suction, a_f, b_f and c_f are fitting parameters and ψ_r is soil suction corresponding to the residual water content θ_r. Similar to Equation 7.1, a_f is related to air entry value and has the unit of kPa^{-1}, b_f describes the slope of SWCC as soon as the air entry value is exceeded and c_f is related to the residual value. The equation was used extensively in the literature, and it provides a good fit for a wide range of soils over the complete suction range from 0 kPa to 10^6 kPa.

Other equations to model the SWCC have been proposed in the literature, such as [Brooks & Corey, 1964] and [McKee & Bumb, 1987]. Both equations are two-parameter equations. Tinjum et al. [1997] measured SWCC in laboratory for four compacted clays. Using the least-square method to fit the data, they found that the Van Genuchten equation provided a better fit to the data than the Brooks and Corey equation because it is inherently more flexible. In their review of soil-water characteristic curves equations, Leong & Rahardjo [1997] examined the most popular equations to estimate SWCC. They concluded that the Fredlund and Xing equation gave the best fit to data. Based on this, only the Van Genuchten equation and the Fredlund and Xing equation are considered for further analysis in this research.

For better visualization of the SWCC, the degree of saturation, S, is used instead of volumetric water content, θ. If one divides both sides of Equation 7.1 by saturated volumetric water content, θ_s, one gets the Van Genuchten equation

in terms of the degree of saturation:

$$S = S_r + \frac{1 - S_r}{[1 + (a_{vg}\psi)^{b_{vg}}]^{c_{vg}}} \tag{7.4}$$

where S is the degree of saturation at any soil suction and is equal to θ/θ_s, S_r is the residual degree of saturation and fitting parameters a_{vg}, b_{vg} and c_{vg} are as described in Equation 7.1. Similarly, Equation 7.2 can be rewritten as follows:

$$S = \frac{C(\psi)}{\{ln\,[e + (\psi/a_f)^{b_f}]\}^{c_f}} \tag{7.5}$$

where $C(\psi)$, a_f, b_f and c_f are as described in Equation 7.2.

For the sand used in this research, Hostun sand, SWCC was determined experimentally by Alabdullah [2010] and is presented in Figure 7.14. Both the Van Genuchten equation and Fredlund and Xing equation are utilized to fit the experimental data by means of a statistical nonlinear regression analysis. As demonstrated in Figure 7.14, the agreement of both equations with the data is excellent. R^2 was found to be 99.8 %. It was found that the fitting parameter ψ_r in Fredlund and Xing equation equals 78430. Then $C(\psi) = 0.9999 \approx 1$. The $C(\psi)$ correction is designed to give a better fitting for high suctions, and therefore, can be neglected for the low suctions of sand, and it is no longer considered in this analysis. Table 7.1 summarizes the results of this analysis for both equations.

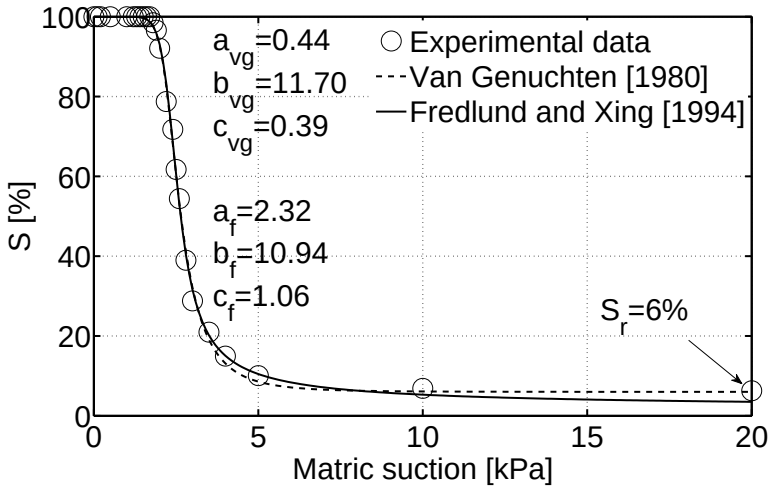

Figure 7.14: Experimental data of SWCC and fitting with Equations 7.4 and 7.5

Table 7.1: Modeling parameters of Van Genuchten equation and Fredlund and Xing equation for SWCC

Equation	*Fitting parameters*	R^2
Van Genuchten, Eq. 7.4	$a_{vg} = 0.44$, $b_{vg} = 11.70$, $c_{vg} = 0.39$	99.8 %
Fredlund and Xing, Eq. 7.5	$a_f = 2.32$, $b_f = 10.94$, $c_f = 1.06$	99.8 %

It is noticed in Figure 7.13 that change of velocity with suction and absolute change of degree of saturation with suction have the same shape. This indicates that velocity and degree of saturation change at the same rate. A direct relationship between velocity and degree of saturation can then be suggested as follows:

$$v_S = v_{sat}\left[1 + \Gamma(1 - \Theta)\right] \tag{7.6}$$

where v_S is velocity as a function of saturation, v_{sat} is velocity in saturated condition, Θ is called effective saturation or normalized water content which is defined as:

$$\Theta = \frac{\theta - \theta_r}{\theta_s - \theta_r} = \frac{S - S_r}{1 - S_r} \tag{7.7}$$

and Γ is a suggested parameter that represents the normalized velocity change between saturated and residual conditions, which is defined as:

$$\Gamma = \frac{v_r - v_{sat}}{v_{sat}} \tag{7.8}$$

where v_r is velocity in the residual condition. Equation 7.6 describes the velocity change between saturation and residual value in terms of effective saturation, Θ. If $\theta_r = 0$, then $\Theta = S$. Equation 7.6 can be written in terms of volumetric water content or saturation as:

$$v_S = v_{sat}(1 + \Gamma\frac{\theta_s - \theta}{\theta_s - \theta_r}) = v_{sat}(1 + \Gamma\frac{1 - S}{1 - S_r}) \tag{7.9}$$

A direct relationship between velocity and suction is still needed. Such a relationship can be derived from the previous equations. From Equation 7.1, the value of Θ can be written as:

$$\Theta = \frac{\theta - \theta_r}{\theta_s - \theta_r} = \frac{1}{\left[1 + (a_{vg}\psi)^{b_{vg}}\right]^{c_{vg}}} \tag{7.10}$$

By substituting Θ into Equation 7.6, one gets:

$$v_\psi = v_{sat}\left[1+\Gamma(1-\frac{1}{[1+(a_{vg}\psi)^{b_{vg}}]^{c_{vg}}})\right] \tag{7.11}$$

where v_ψ is velocity as a function of suction, v_{sat} is velocity in the saturated condition and parameters a_{vg}, b_{vg} and c_{vg} are fitting parameters as described in Equation 7.1. Similarly, a relationship between velocity and suction can be derived based on Equation 7.2 of Fredlund and Xing. By substituting S from Equation 7.5 into Equation 7.9, one gets:

$$v_\psi = v_{sat}\left[1+\frac{\Gamma}{1-S_r}(1-\frac{C(\psi)}{\{ln\,[e+(\psi/a_f)^{b_f}]\}^{c_f}})\right] \tag{7.12}$$

where $C(\psi)=1$ for low suctions and parameters a_f, b_f and c_f are fitting parameters as described in Equation 7.2. The main difference between Equation 7.11 and Equation 7.12 is that the former describes velocity change between saturation and residual value, while the latter describes the velocity change between saturation and dry conditions. In both equations, when $\psi=0$, then $v_\psi = v_{sat}$. In Equation 7.11, when $\psi\to\infty$, then $v_\psi = v_{sat}(1+\Gamma)$, while in Equation 7.12, when $\psi\to\infty$, then $v_\psi = v_{sat}\,[1+\Gamma/(1-S_r)]$.

Equations 7.11 and 7.12 are compared with experimental data of this research. Figure 7.15 demonstrates the results of fitting models of data for Hostun sand at 100 kPa net stress. Model 1 in the figure is Equations 7.11, and model 2 is Equations 7.12. In model 2, $C(\psi)$ was considered 1, as discussed before. Parameters a, b and c have the same values as the fitting of the SWCC in Figure 7.14. The normalized velocity change between saturated and residual values was found to be $\Gamma=0.05$. $S_r=0.06$ from the SWCC. Velocity is normalized to the initial value at saturation. Models fit data with excellent agreement. For both models $R^2=99.3$ %. Figure 7.16 demonstrates the results of fitting models to data for Hostun sand at 50 kPa net stress. Γ for this test is 0.09. The models have less agreement with the data than in Figure 7.15. As seen in Figure 7.13, the velocity change is less smooth than of the test with 100 kPa net stress. Between 4 kPa and 10 kPa, the models seem to overestimate velocity change. This is probably because the amount of water extracted from the specimen for a given matric suction is not always identical to the SWCC and might slightly change due to imperfections in the experimental system, such as imperfect contact between the specimen and the ceramic disk. This causes the saturation-suction relationship

to deviate from the average SWCC. The measured SWCC of any soil has its own variability and uncertainty [Zapata et al., 2000]. Therefore, any prediction to relate a certain property to the SWCC cannot exceed that inherent measurement uncertainty of the SWCC. However, this difference is handled in Section 7.4.3, where more general models are proposed. Model 2 (Equation 7.12) fits data with $R^2 = 97.0$ % slightly better than model 1 (Equation 7.11) with $R^2 = 96.1$ %.

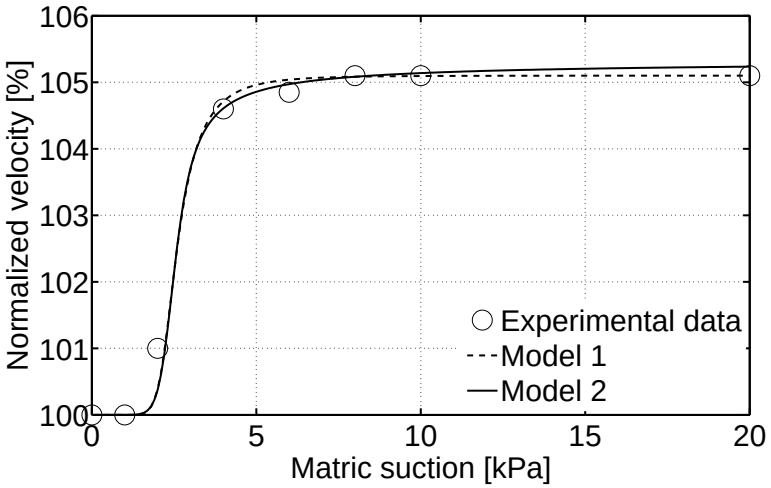

Figure 7.15: Model 1 (Equation 7.11) and model 2 (Equation 7.12) to predict velocity change versus experimental data of Hostun sand at 100 kPa net stress

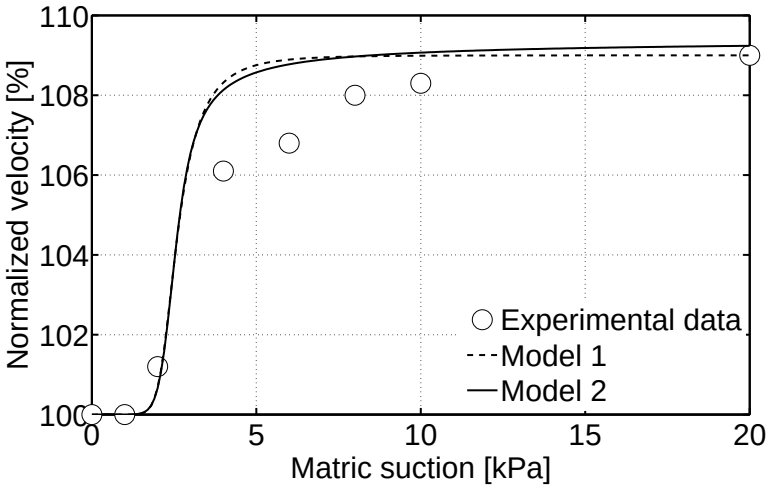

Figure 7.16: Model 1 (Equation 7.11) and model 2 (Equation 7.12) to predict velocity change versus experimental data of Hostun sand at 50 kPa net stress

It is shown here that the models presented in this section, which are based on the SWCC, can reasonably well predict velocity change of shear waves between saturation and residual values. Agreement ranges from $R^2 = 96.1$ % to $R^2 = 99.3$ % for data in this research.

7.4.2 Predicting shear wave velocity from GSD

It is well known that the soil-water characteristic curve is difficult to obtain experimentally. Its experiments are expensive and very time consuming. For clays, this may take many months. For practical geotechnical applications, a better, easier way is necessary. For this reason, more basic models that depend on easily obtained properties of soil are derived in this section.

The SWCC describes the amount of water in the voids, while the grain size distribution (GSD) describes the sizes of solids. Many researchers proposed models to link both curves. Torres Hernandez [2011] did an extensive study on more than 31000 data points for plastic soils and 4500 data points for non-plastic soils. He proposed a set of models to estimate the parameters of SWCC in the Fredlund and Xing equation from the grain size distribution. The parameters are functions of certain characteristics of the GSD curve. The fitting parameters of the SWCC equation of Fredlund and Xing are estimated as follows:

$$a_f = -967.21 D_{10}^2 + 218.37 D_{10} - 2.7 \tag{7.13}$$

$$b_f = 10^{-0.0075 a_f^3 + 0.1133 a_f^2 - 0.3577 a_f + 0.3061} \tag{7.14}$$

$$c_f = 0.0058 a_f^3 - 0.0933 a_f^3 + 0.4069 a_f + 0.3481 \tag{7.15}$$

$$\psi_r = 100 \tag{7.16}$$

where D_{10} is grain diameter in mm corresponding to 10 % passing by weight, a_f, b_f, c_f and ψ_r are fitting parameters in Equation 7.4 or Equation 7.5. D_{10} has a constraint, that is when $D_{10} < 0.02$, then $a_f = 1.28$.

Zapata et al. [2000] analyzed grain size distribution for three types of soil and compared it with corresponding SWCC. They proposed a model that predicts the parameters of Fredlund and Xing equation based on properties of the grain size distribution. They chose D_{60}, grain diameter in mm corresponding to 60 % passing by weight, to estimate a_f, b_f, c_f and $C(\psi)$. For granular material with plasticity index equal to zero, the model is as follows:

$$a_f = 0.8627 D_{60}^{-0.751} \tag{7.17}$$

$$b_f = 7.5 \tag{7.18}$$

$$c_f = 0.1772\, lnD_{60} + 0.7734 \tag{7.19}$$

$$\psi_r = \frac{a_f}{D_{60} + 9.7e^{-4}} \tag{7.20}$$

They found no correlation between parameter b_f and D_{60}. Therefore, they suggested an average value of 7.5. Furthermore, all parameters a_f, b_f, c_f and ψ_r had relatively low R^2 values when correlated with D_{60}.

Houston et al. [2006] obtained D_{10} through D_{90} from the GSD and attempted to correlate different combinations to the SWCC as a part of the Mechanistic-Empirical Pavement Design Guide (MEPDG). They included the data used by Zapata [1999] as well as their own data. They also introduced the parameters D_0 and D_{100}, which are estimated by projecting the two extremes of the GSD curve on to Percent Passing 0 % and 100 % lines, respectively. Then they tried to find a link to the parameters of the Fredlund and Xing equation by means of a statistical nonlinear regression analysis. Their functions are as follows:

$$a_f = 1.14a - 0.5 \tag{7.21}$$

where

$$a = -2.79 - 14.1\, logD_{20} - 1.9 * 10^{-6}\, P_{200}^{4.34} + 7\, logD_{30} + 0.055 D_{100} \tag{7.22}$$

$$D_{100} = 10^{\frac{40}{m_1} + logD_{60}} \tag{7.23}$$

$$m_1 = \frac{30}{logD_{90} - logD_{60}} \tag{7.24}$$

$$b_f = 0.936b - 3.8 \tag{7.25}$$

where

$$b = \left[5.39 - 0.29\, ln(P_{200}\frac{D_{90}}{D_{10}}) + 3D_0^{0.57} + 0.021P_{200}^{1.19}\right] m_1^{0.1} \tag{7.26}$$

$$D_0 = 10^{\frac{-30}{m_2} + logD_{30}} \tag{7.27}$$

$$m_2 = \frac{20}{logD_{30} - logD_{10}} \tag{7.28}$$

$$c_f = 0.26e^{0.758c} + 1.4D_{10} \tag{7.29}$$

where

$$c = logm_2^{1.15} - (1 - \frac{1}{b_f}) \tag{7.30}$$

$$\psi_r = 100 \tag{7.31}$$

where D_{10}, D_{20}, D_{30}, D_{60} and D_{90} are the grain diameter in mm corresponding to 10 %, 20 %, 30 %, 60 % and 90 % passing by weight, respectively, D_0 and D_{100} are a projection of the two extremes of the GSD curve on to Percent Passing 0 % and 100 % lines, respectively, and P_{200} is the material passing U.S. standard sieve #200 (diameter 74 μm) in percentage.

The previously explained models, Torres Hernandez model, Zapata model and MEPDG model are examined by deriving the corresponding parameters a_f, b_f, c_f and ψ_r for each model and attempting to fit the SWCC of the sand used in this research, Hostun sand. The grain size distribution of Hostun sand is shown in Figure 7.17. The parameters required for the models are obtained from the curve and listed in Table 7.2. The parameters a_f, b_f, c_f and ψ_r of all three models are calculated after the above-mentioned functions and listed in Table 7.3. The predicted SWCCs of these models are compared with the measured SWCC of Hostun sand in order to validate the models. Figure 7.18 demonstrates the comparison. It is evident that the MEPDG model appears very close to the SWCC. It can also be noticed that in Table 7.3 the parameters of MEPDG model are

close to the ones of the best fit of Fredlund and Xing equation (see Table 7.1). The agreement is excellent, with $R^2 = 99.4$ %. The Torres Hernandez model provides a very poor prediction. The Zapata model gives unsatisfactory prediction as well, especially at high suctions. This is because both models are derived from solely one indicator of the grain size distribution, that is D_{10} for the Torres Hernandez model and D_{60} for the Zapata model. While the MEPDG model derives the required parameters from a variety of indicators of the GSD (see Table 7.2). Therefore, the MEPDG model is the one considered to predict velocity change.

Parameters calculated from the MEPDG model are used in Equation 7.12 to predict velocity change for Hostun sand. As stated previously, $S_r = 0.06$, $\Gamma = 0.05$ for net stress at 100 kPa and $\Gamma = 0.09$ for net stress at 50 kPa. Parameters a_f, b_f, c_f and ψ_r are as listed in Table 7.3. Results are demonstrated in Figure 7.19 and Figure 7.20. The agreement for net stress at 100 kPa is excellent. R^2 was found to be 100.0 %. For net stress at 50 kPa, the agreement is less satisfactory with $R^2 = 96.9$ %. The two Figures, 7.19 and 7.20, are in their agreements very similar to Figures 7.15 and 7.16. The slight deviation in Figure 7.20 can be explained similar to Figure 7.16 in Section 7.4.1.

It can be concluded here that the SWCC, although it delivers very valuable information about soil behavior, is not necessary to predict velocity change with suction. Grain size distribution, which is an easy, fast and cheap test, is enough to derive the fitting parameters of Equation 7.12. Velocity measurements are necessary at saturated and residual conditions to establish the parameters Γ and S_r. All relative velocities in between can be then predicted using this approach.

7.4.3 General prediction of shear wave velocity

The proposed models so far are dependent on determining SWCC of the soil, which is a very time-consuming procedure, or on GSD. Here, more general models independent of the previously mentioned curves are presented. For these models, knowing a few points is enough to derive the whole gradient curve of velocity between saturation and residual values. In the previous Sections, 7.4.1 and 7.4.2, parameters a, b and c are derived from characteristics of the SWCC or the GSD. In this general approach, these parameters are considered free to take

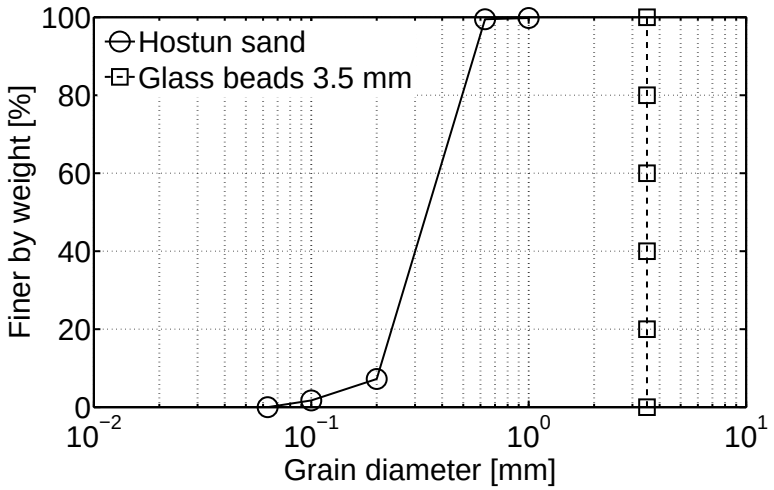

Figure 7.17: Grain size distribution of Hostun sand

Table 7.2: Parameters obtained from the grain size distribution of Hostun sand

Parameter	*Value*
D_{10}	0.208 mm
D_{20}	0.235 mm
D_{30}	0.266 mm
D_{60}	0.386 mm
D_{90}	0.560 mm
P_{200}	0.65 %

Table 7.3: Parameters a_f, b_f, c_f and ψ_r for Torres Hernandez model, Zapata model and MEPDG model

Parameter	*Torres Hernandez model*	*Zapata model*	*MEPDG model*
a_f [kPa^{-1}]	0.876	1.763	2.087
b_f	1.159	7.500	10.763
c_f	0.646	0.605	1.060
ψ_r [kPa]	100	3.128	100

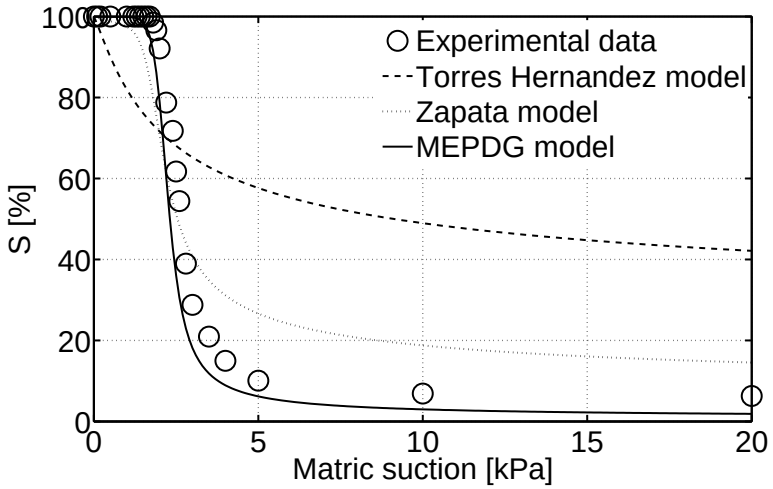

Figure 7.18: Torres Hernandez model, Zapata model and MEPDG model to predict the SWCC

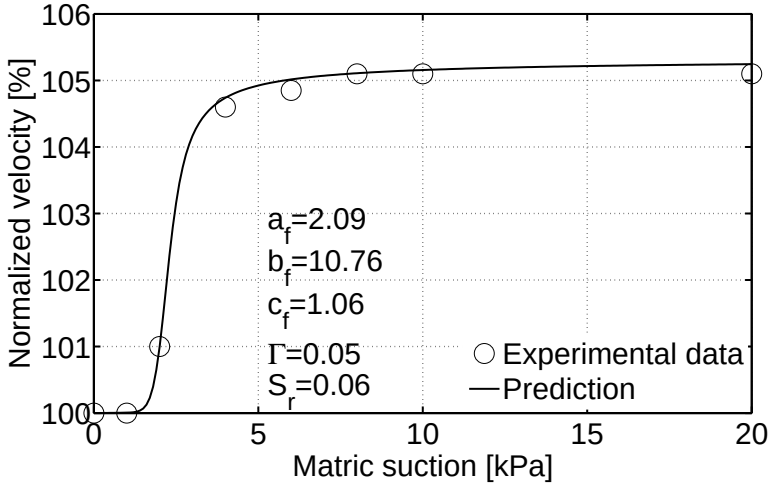

Figure 7.19: Experimental data of velocity change versus predicted values based on parameters derived from the MEPDG model of Hostun sand at 100 kPa net stress

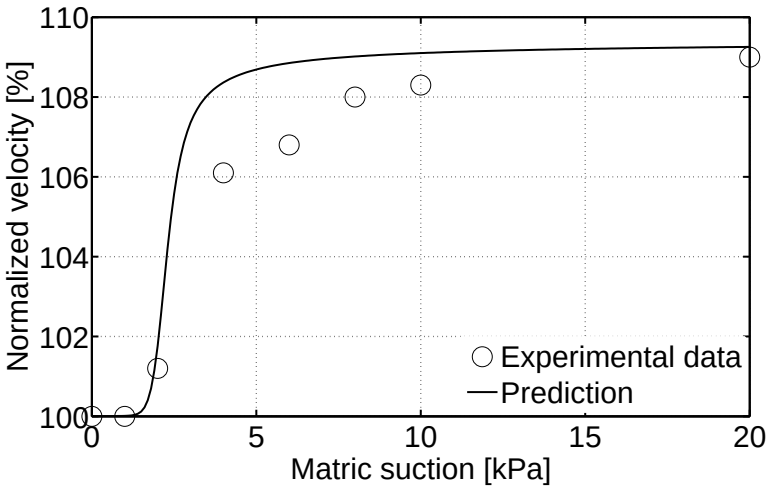

Figure 7.20: Experimental data of velocity change versus predicted values based on parameters derived from the MEPDG model of Hostun sand at 50 kPa net stress

any value to fit the data regardless of the SWCC and the GSD. Data of Hostun sand are fitted with Equation 7.11 and Equation 7.12 using the statistical non-linear regression analysis. Figures 7.21 and 7.22 show the results of this fitting. Table 7.4 summarizes the resulting parameters for both models. Γ is fixed at 0.05 and 0.09 and S_r at 0.06, as in the previous sections. For that reason, velocity measurements at full saturation and residual condition are necessary. For Hostun sand at 100 kPa net stress, Figure 7.21 shows excellent agreement between both models and experimental data with $R^2 = 100.0$ %. This agreement holds also for Hostun sand at 50 kPa net stress in Figure 7.22 with $R^2 = 99.6$ % for model 1 (Equation 7.11) and $R^2 = 99.5$ % for model 2 (Equation 7.12). By comparing Figure 7.22 with Figures 7.16 and 7.20, it can be concluded that data from the test with net stress of 50 kPa are modeled much better when parameters are freed than when derived from SWCC or GSD.

The advantage of this approach is that in the absence of SWCC or GSD, a few data points of velocity, ideally at saturation condition, shortly after the AEV and residual condition, are enough to estimate the whole suction-velocity curve with Equations 7.11 and 7.12 or the saturation-velocity curve with Equation 7.9.

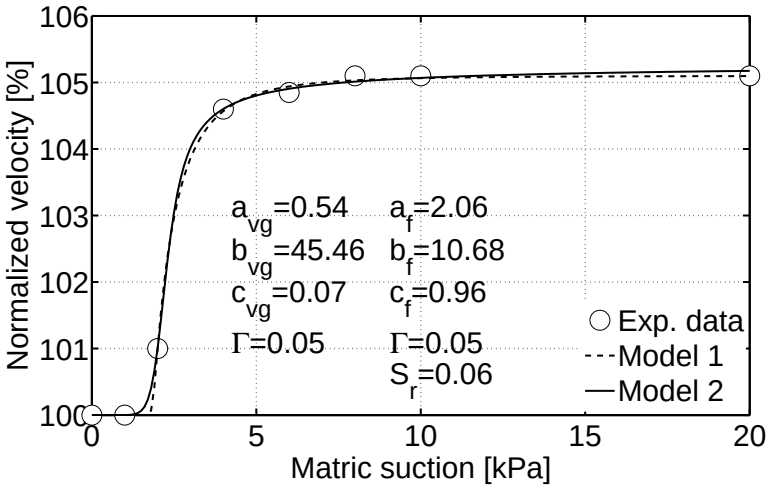

Figure 7.21: Model 1 (Equation 7.11) and model 2 (Equation 7.12) with free parameters to predict velocity change versus experimental data of Hostun sand at 100 kPa net stress

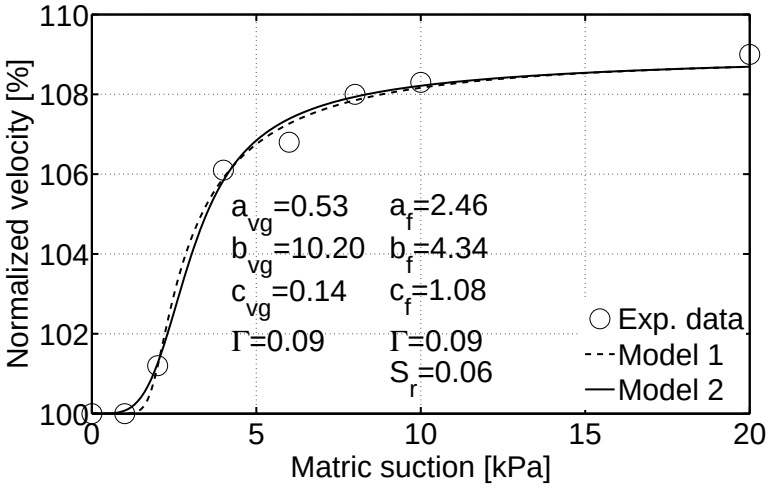

Figure 7.22: Model 1 (Equation 7.11) and model 2 (Equation 7.12) with free parameters to predict velocity change versus experimental data of Hostun sand at 50 kPa net stress

Table 7.4: Parameters of model 1 (Equation 7.11) and model 2 (Equation 7.12)

Net stress	*Equation*	*Fitting parameters*	R^2
100 kPa	Model 1, Eq. 7.11	$a_{vg} = 0.54$, $b_{vg} = 45.46$, $c_{vg} = 0.07$	100.0 %
100 kPa	Model 2, Eq. 7.12	$a_f = 2.06$, $b_f = 10.68$, $c_f = 0.96$	100.0 %
50 kPa	Model 1, Eq. 7.11	$a_{vg} = 0.53$, $b_{vg} = 10.20$, $c_{vg} = 0.14$	99.6 %
50 kPa	Model 2, Eq. 7.12	$a_f = 2.46$, $b_f = 4.34$, $c_f = 1.08$	99.5 %

7.4.4 Validation with previous studies

The range of suction for Hostun sand is limited. Although many data points of velocity were measured along this curve, it would be interesting to validate the models in a higher suction range. An intensive study was done by Sawangsuriya et al. [2009] to investigate the unsaturated small strain shear stiffness of five fine grained soils. This study was chosen because it contains five soils, complete SWCCs and shear modulus values based on bender elements measurements. Other studies lack one or another of the necessary measurements to validate the models proposed here. The soils used are clayey sand (SC), silt (ML), lean clay-1 (CL-1), lean clay-2 (CL-2) and fat clay (CH). The same abbreviations are maintained for ease of comparison with the original study. Properties of these soils are listed in Sawangsuriya [2006] and Sawangsuriya et al. [2009]. Figures. 7.23 and 7.24 show the SWCCs of the tested soils. The five soils are split into two figures for better visualization. It is worth noticing that the SWCCs are presented in volumetric water content, θ, not degree of saturation, S. The data points of these curves at high suctions lie beyond θ_r, the residual value of volumetric water content, which is determined according to the graphical definition proposed by Fredlund & Xing [1994] (explained later in this section). This makes the SWCC-equation of Fredlund and Xing (Equation 7.2) more suitable to fit the curves since it describes volumetric water content between saturation and dry conditions, unlike the SWCC-equation of Van Genuchten (Equation 7.1) that describes volumetric water content between saturation and residual value. Therefore, for this section, only Equation 7.2 and subsequently, model 2 (Equation 7.12) are considered. Following the steps of the previous sections, first, the SWCC is fit using Equation 7.2 of Fredlund and Xing, then the fitting parameters are used to model the relationship between shear modulus and suction. Saturation volumetric water content, θ_s, was not given by the original study; rather, it remains

as another fitting parameter. The fitting curves match the measured data with excellent agreement. Table 7.5 shows the fitting parameters a_f, b_f, c_f, ψ_r and θ_s using the statistical nonlinear regression analysis. Parameter ψ_r is not neglected here because the SWCCs extend into very high suctions. It can be noticed that a_f has high values compared to its value for Hostun sand. This comes from the high amount of fine content in the tested soils that pushes the AEV further to the right in the SWCC, which is reflected in return in higher a_f values. The R^2 values are very high, ranging from 99.2 % to 99.9 %.

In Figures 7.25 and 7.26, the measured shear moduli from Sawangsuriya et al. [2009] are plotted against matric suction. The five soils are split into two figures here as well for better visualization. The fitting parameters of Fredlund and Xing are used to model and predict the value of shear modulus. Model 2 (Equation 7.12) was developed to estimate velocity change in unsaturated soils, but it is equally valid for shear modulus, since $G = \rho v^2$, where ρ is density. So Equation 7.12 can be written in term of shear modulus as follows:

$$G_\psi = G_{sat}\left[1 + \frac{\Gamma}{1 - S_r}\left(1 - \frac{C(\psi)}{\{ln\,[e + (\psi/a_f)^{b_f}]\}^{c_f}}\right)\right] \tag{7.32}$$

where G_ψ is shear modulus at small strain as a function of matric suction, G_{sat} is shear modulus at small strain in saturation condition and other parameters are as described in Equation 7.12. Since $S_r = \theta_r/\theta_s$, then θ_r, the residual value of volumetric water content, is required. To estimate θ_r, the graphical definition proposed by Fredlund & Xing [1994] is considered. A tangent line is drawn from the desorption curve. Another tangent line is drawn from the high suction range. The intersection of the two lines represents the residual water content, θ_r. Figure 7.23 demonstrates the estimation of θ_r for SC. For the other soils, the same steps were followed. θ_s has already been estimated in Table 7.5, $S_r = \theta_r/\theta_s$ can then be calculated for all soils. Figures 7.25 and 7.26 show the agreement between the model of Equation 7.32 and the experimental data. Fitting parameters are listed in Table 7.6. The predictions for the soils SC, CL1, CL2 and CH show very good to excellent agreement with R^2 ranging from 92.8 % to 99.7 %. The prediction for ML had a less satisfactory result with experimental data with $R^2 = 72.2$ %. Considering the properties of the tested soils, no specific extreme value of ML compared to the other soils was found to be the potential reason for this difference. It can be theorized, that the assumption of constant

volume considered in deriving the model of Equation 7.32 in previous sections is not valid for the test of ML. That means that the volume change was larger than the acceptable error margin for this model. Volume change through the tests was not given in [Sawangsuriya et al., 2009]. Therefore, this hypothesis could not be verified or falsified, and the reason for the unsatisfactory agreement between model and experimental data for the soil ML remains unrevealed. However, the overall comparison shows a good agreement for higher suctions, and the model seems to be valid.

The advantage of the model proposed in this research over the ones of [Sawangsuriya et al., 2009], the one of [Oh & Vanapalli, 2014] and similar models is that the current model relates velocity or shear modulus to only suction or to only degree of saturation, while in other models the relation is with both of them. This is logical since the degree of saturation and suction are related to each other in the SWCC, and thus these models do not contain independent parameters. There is no need to include both suction and saturation (or water content) in a model since the SWCC can be modeled very well, as shown in Section 7.4.1, and a relationship between the two quantities can be derived from such a model. Furthermore, the current model is a predictive one that allows estimating velocity or shear modulus of unsaturated soils based on their SWCC with only a very few measurements. The parameters of the model are not merely fitting parameters; rather, they have physical meanings. The other approach of the model, predicting shear wave velocity from GSD, can be of greater importance because it is based on a more basic, simple test. Studies in the literature that deal with velocity measurements with different suctions for a given GSD are scarce. No complete set of tests could be found to validate this approach for higher suctions. In the case of absence of SWCC or GSD of a certain soil, a few data points of velocity, ideally at saturation condition, shortly after the AEV and residual condition, are enough to estimate the whole suction-velocity curve using the approach in Section 7.4.3.

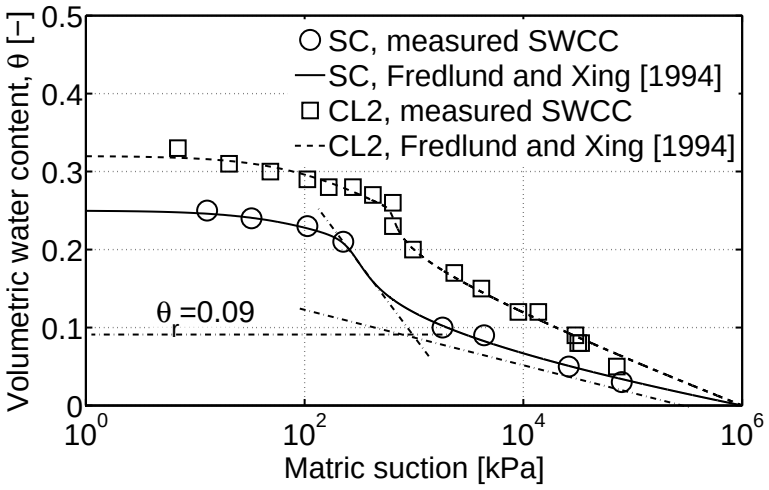

Figure 7.23: Measured SWCC and fitting Equation 7.2 of soils SC and CL2

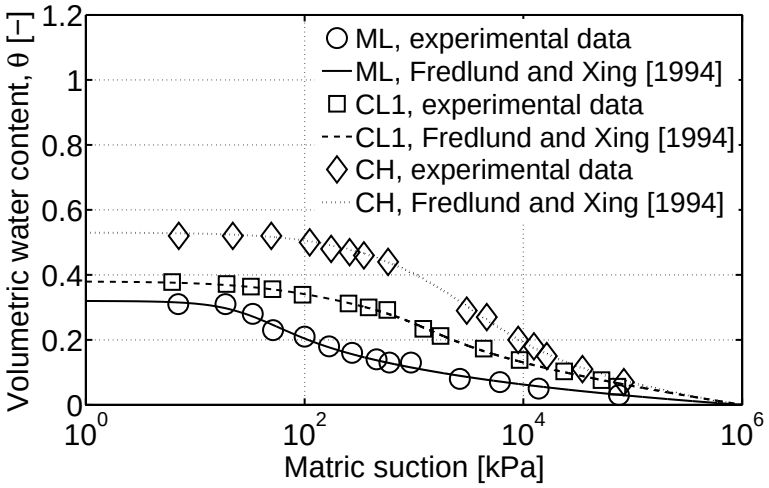

Figure 7.24: Measured SWCC and fitting Equation 7.2 of soils ML, CL1 and CH

Table 7.5: Parameters a_f, b_f, c_f, ψ_r and θ_s for fitting the SWCCs in [Sawangsuriya et al., 2009]

Parameter	*SC*	*ML*	*CL1*	*CL2*	*CH*
a_f [kPa^{-1}]	252.30	28.58	858.40	611.60	2170.00
b_f	6.69	1.83	2.36	23.07	1.43
c_f	0.19	0.44	0.18	0.07	0.45
ψ_r [kPa]	77.13	258.80	57.70	100.80	223.60
θ_s	0.25	0.32	0.38	0.32	0.53
R^2	99.9 %	99.2 %	99.8 %	99.3 %	99.9 %

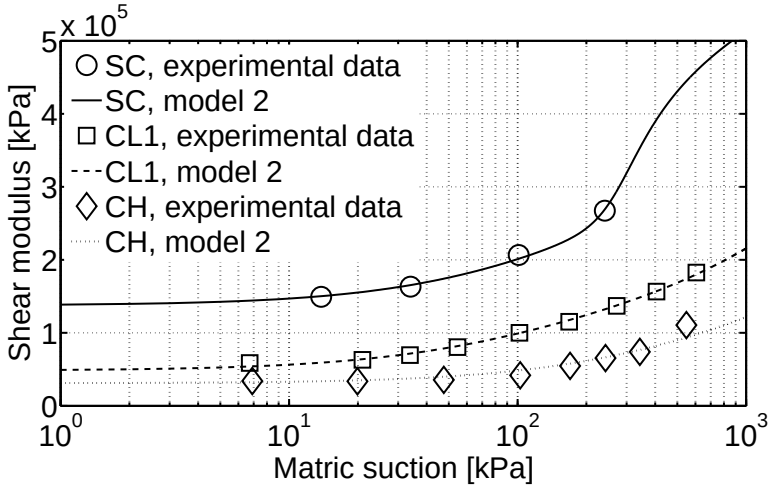

Figure 7.25: Measured shear modulus and prediction model 2 (Equation 7.32) of soils SC, CL1 and CH

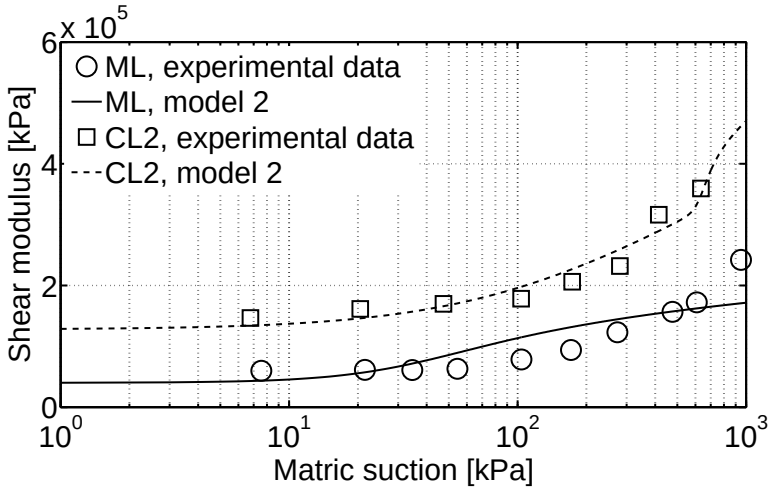

Figure 7.26: Measured shear modulus and prediction model 2 (Equation 7.32) of soils ML and CL2

Table 7.6: Parameters G_{sat}, Γ and S_r for fitting the shear modulus values in [Sawangsuriya et al., 2009]

Parameter	*SC*	*ML*	*CL1*	*CL2*	*CH*
G_{sat} [kPa]	13.77 x10^4	4.00 x10^4	4.84 x10^4	12.77 x10^4	3.16 x10^4
Γ	3.24	3.64	6.79	3.01	10.00
S_r	0.38	0.29	0.33	0.58	0.18
R^2	99.6 %	72.2 %	99.7 %	93.3 %	92.8 %

7.5 Numerical approach

7.5.1 Introduction

In order to make predicting shear wave velocity achievable in the absence of experimental data for the SWCC, a numerical method is utilized to estimate the SWCC from grain size distribution and void ratio based on theoretical assumptions. This method avoids the time and costs associated with obtaining the SWCC. Sattari [2014] and Sattari & Toker [2016] successfully applied this method to simulate the SWCC. Using a MATLAB code, they were able to model drainage in a soil medium along the drying path of the SWCC. The parameters a, b and c can then be derived from the simulated SWCC using Equations 7.4 and 7.5 and be implemented in Equations 7.11 and 7.12 to get the shear wave velocity. Merging the analytical models from the semi-empirical approach and the numerical simulation this way allows predicting shear wave velocity from grain size distribution and void ratio without conducting the time-consuming test to obtain SWCC.

7.5.2 Methodology

Soil grains are considered spherical particles that are packed, taking into consideration the grain size distribution. The particles are arranged inside a predefined medium, where solid phase is generated. The water in the pores is divided into bulk water, which is among particles, and water bridges, which is formed after drainage and have the shape of pendular rings. The volume of pore bodies and pendular rings can then be calculated. The air entry value at the micro scale, for each pore throat, is determined. Finally, the drainage of the saturated medium is simulated, and the volume of drained pore bodies and pendular rings for a specific suction is determined. Volumetric and gravimetric water content, as well as saturation level, can then be computed using soil phase relations. In the following paragraphs, the steps of this method are explained.

Generating of solid phase

The solid phase of the medium is generated based on the grain size distribution. The curve of the grain size distribution is divided into small linear segments.

The number of particles in the coarsest segment is assumed to be N_1. The total number of particles in each segment, N_i, with relative to previous segments can then be calculated:

$$N_i = N_{i-1} \frac{M_i - M_{i+1}}{M_{i-1} - M_i} \left[\frac{D_{i-1} - D_i}{D_i - D_{i+1}} \right]^3 \tag{7.33}$$

where M is the mass percent of the particles retained on the sieve diameter D. The void ratio of a soil sample, e, is another input of the simulation process. The void ratio of the packed medium is calculated and compared with e. If the error remains in the tolerance range of 0.02, the packing algorithm is validated, and the simulation will proceed to the next stage. The specific gravity is considered here to be a constant.

The particles are then arranged inside the medium. A particle is considered stable when it forms three contact points with other particles, or it rests at the bottom of the medium box. The stability of each particle is controlled. The periodic boundary condition is then applied. The particles that are located nearby the boundary of the medium box are replicated in the X, Y or XY direction. Figure 7.27 demonstrates the packed and duplicated particles in $2D$. If the particle's center lies in a mirroring region defined by $M_r = d_{max}$, where d_{max} is the largest particle diameter, then this particle is duplicated, as in Figure 7.27. By using the periodic boundary condition, there is no need anymore to define boundary-air-water interfaces.

Identification of pore bodies

The individual pores are then considered one by one. The pore water consists of bulk water and pendular rings. The pendular rings are formed due to the capillary force between two adjacent particles. The pore throats, which are the narrow connections of pores among particles, are identified. This results in quantifying the bulk water as well as the connectivity of pores. The boundaries of individual pores are determined by forming a plane among the centers of the adjacent three particles. This holds as long as other particles do not intersect this plane, for example, when a smaller particle is trapped among three larger particles. In this case, three smaller planes are formed. At opposite sides of each pore throat plane, a pair of points, called side-points, is generated, as shown in

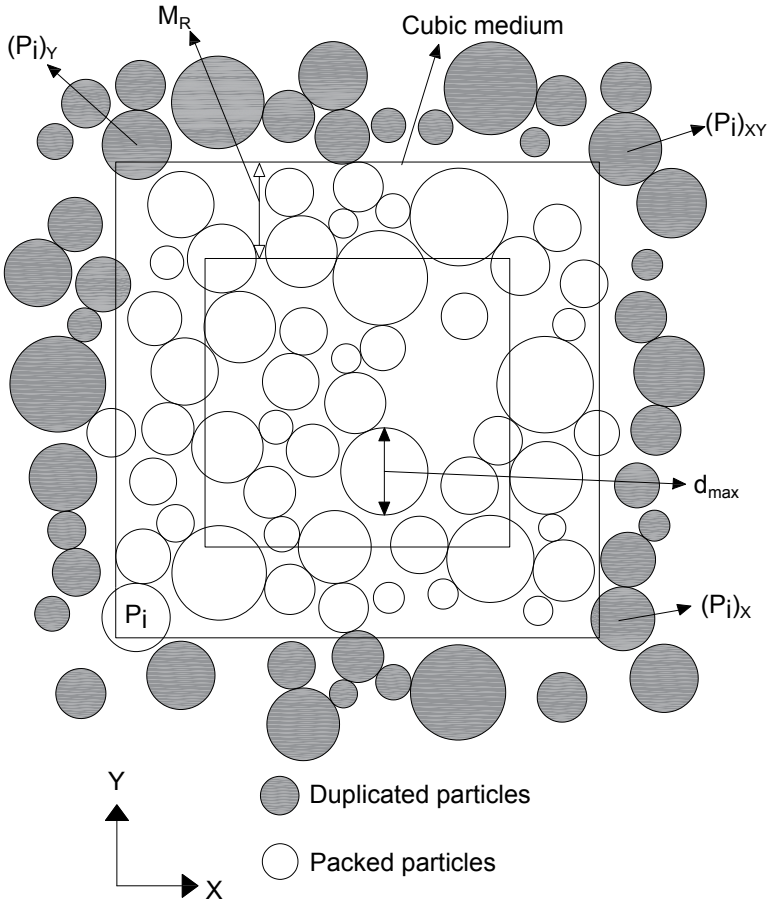

Figure 7.27: The application of periodic boundary condition in X- and Y-axis (modified after Sattari & Toker [2016])

Figure 7.28a. The figure illustrates the identification of a pore body between four particles and triangle pore throat planes. The volume of pore bodies is then determined. However, the shape of the pore bodies is irregular. To simplify this problem, the identified side-points of each bulk pore are considered to be vertices of tetrahedrons (Figure 7.28b). In this case, the volume of each pore body is represented by polyhedrons. For a bulk pore consists of four side-points, one tetrahedron can be formed, while for a bulk pore consists of five side-points, two tetrahedrons can be created. The volumes of the tetrahedrons are determined by means of Delaunay triangulation and convex hull functions, which are included in MATALB program.

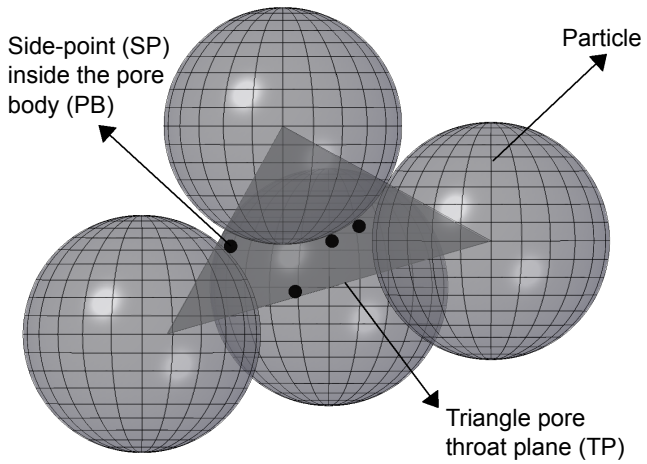

(a) Defined throat plane and side-points

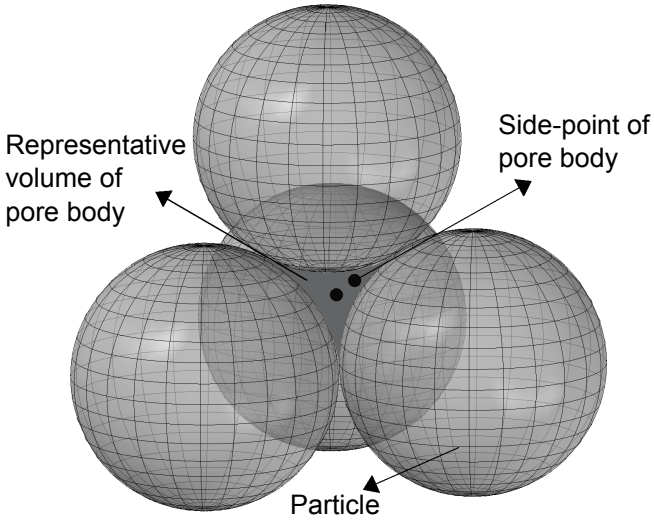

(b) Pore volume trapped among particles

Figure 7.28: The application of Delaunay triangulation (modified after Sattari & Toker [2016])

Identification of pendular rings

Four parameters control the volume of the pendular rings: applied suction load ψ, air-water surface tension σ_{st}, contact angle in the air-water-particle interface ϵ and distance between the particles d. Chen et al. [2011] calculated the volume of pendular rings that are developed between unequal-sized spheres. The surface of pendular rings is considered to be torus pieces, as shown in Figure 7.29. They determined the volume of the pendular ring ν_p as follows:

$$\nu_p = \nu_1 - \nu_2 \tag{7.34}$$

where ν_1 and ν_2 are:

$$\begin{aligned}\nu_1 =& \pi \left[(R_1+R_2)^2 + R_1^2\right] R_1 \left[cos(\phi_1+\epsilon) + cos(\phi_2+\epsilon)\right] \\ &+ 2\pi(R_1+R_2)^2 R_1^2(\phi_1+\phi_2+2\epsilon-\pi) \\ &- \frac{\pi}{3} R_1^3 \left[cos^3(\phi_1+\epsilon) + cos^3(\phi_2+\epsilon)\right] \\ &- 2\pi(R_1+R_2)^2 R_1^2 \left[(sin(\phi_1+\epsilon)cos(\phi_1+\epsilon) + sin(\phi_2+\epsilon)cos(\phi_2+\epsilon)\right]\end{aligned} \tag{7.35}$$

$$\nu_2 = \frac{\pi}{3}\left[r_1^3(2-3cos\phi_1+cos^3\phi_1)\right] + r_2^3(2-3cos\phi_2+cos^3\phi_2) \tag{7.36}$$

where R_1 and R_2 are the principal radii of the air-water interface, r_1 and r_2 are the radii of the particles and ϕ_1 and ϕ_2 are the filling angles determined regarding the Young-Laplace equation and the amount of applied suction. The Young-Laplace equation is given as follows:

$$\psi = \sigma_{st}\left(\frac{1}{R_1} - \frac{1}{R_2}\right) \tag{7.37}$$

Determining the inter-particle air entry value

In this method, the air entry value is considered to be a combination of air entry values of individual pore throats. The minimum pressure difference between air and water, in which air penetrates the air-water interface, is considered the air entry value for that pore. For this purpose, a grid that represents the air-water interface is defined in the pore throat region (Figure 7.30). The grid points are divided into three categories: grid points located outside the pore throat region, which are not considered in the air entry value estimation process, boundary

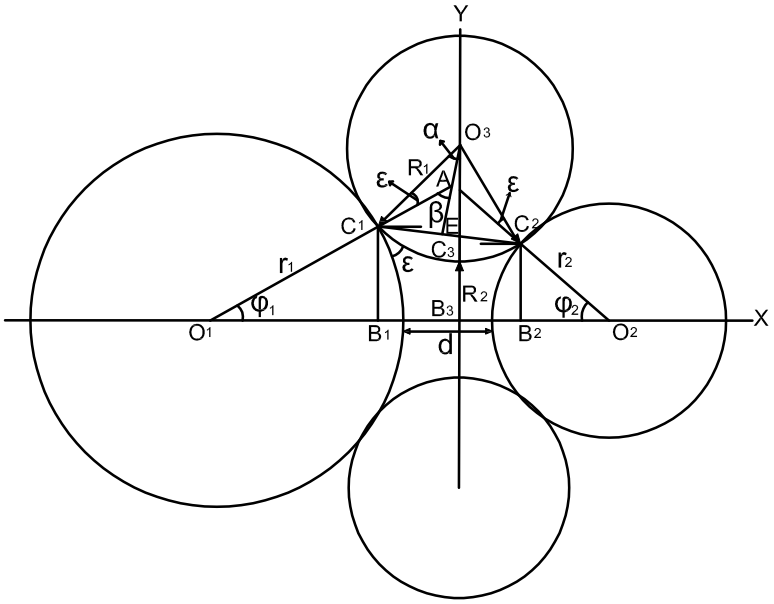

Figure 7.29: The pendular ring developed between two unequal-sized particles (modified after Sattari & Toker [2016])

points, which are located on the interface of air-water-particle and satisfy the contact angle formed in the interface, and curvature points, which represent the curvature of the air-water surface under applied suction value. The boundary points should satisfy the following relation:

$$\begin{aligned}&(x_i - x)z_x + (y_i - y)z_y + (z - z_i) = \\ &cos\epsilon\sqrt{1 + z_x^2 + z_y^2}\sqrt{(x_i - x)^2 + (y_i - y)^2 + (z_i - z)^2}\end{aligned} \tag{7.38}$$

where x_i, y_i and z_i are the coordinate of the particle i and z_x and z_y are the first-order partial derivatives.

The curvature points in equilibrium fulfill the following relation between the applied suction value and the curvature of the air-water interface:

$$\psi = \frac{\sigma_{st}}{(1 + z_x^2 + z_y^2)^{3/2}}\left[(1 + z_y^2)z_{xx} + (1 + z_x^2)z_{yy} - 2z_x z_y z_{xy}\right] \tag{7.39}$$

where z_{xx} and z_{yy} are second-order partial derivatives, and z_{xy} is the mixed partial derivative. Equation (7.38) for boundary points and Equation (7.39) for curvature points are solved using the finite difference approximation and Newton-Raphson (Jacobian) method as follows:

$$[z]^{t-1} = [z]^t - J^{-1}\left[f(z)\right]^t \tag{7.40}$$

where t is the time step and J^{-1} is the inverse of the Jacobian matrix, which is given as:

$$J = \frac{\partial f(z)^t}{\partial z^t} \tag{7.41}$$

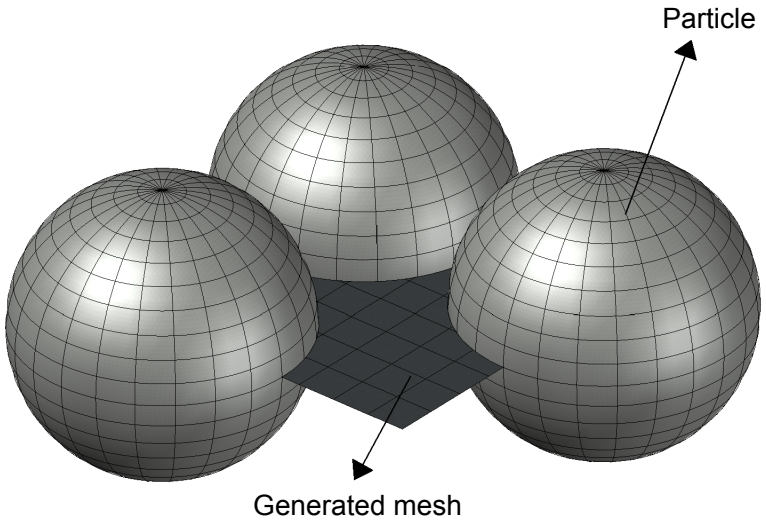

Figure 7.30: The generated mesh in the pore throat region, representing the air-water interface (modified after Sattari & Toker [2016])

Simulation of drainage

After determining the air entry value for each pore, the drainage process is started. The medium is considered saturated at the beginning. When suction exceeds the air entry value for a specific pore, air enters, and that pore is drained. As a result, throat planes surrounding this pore will be subjected to air, and the same process is repeated for neighboring pores. The volume of drained pores can then be calculated. When bulk pores are drained, pendular rings form, whose volume can also be determined.

By determining the volume of drained pore bodies and pendular rings for a specific suction after reaching equilibrium, the volume of the remaining water in the medium is then calculated. Volumetric and gravimetric water content, as well as saturation level, can then be computed using soil phase relations. Ultimately, the SWCC can be plotted as a relationship between matric suction and water content or degree of saturation.

7.5.3 Validation of the numerical model

The simulation was run on Hostun sand with the specimen properties used in this research. The grain size distribution was considered the same as of Hostun sand, as illustrated in Figure 3.1. The void ratio was 0.6 close to the one of the specimen for the unsaturated test with 100 kPA net stress. Other parameters considered in the simulation are: specific gravity, G_s, equals 2.65, air-water surface tension equals 72.8 mN/m, number of iterations is 10 and number of particles in the coarsest segment is 50. The definitions of these parameters and a sensitivity analysis are included in [Sattari, 2014]. The whole suction range of Hostun sand up to 20 kPa was simulated.

As a result of the simulation, roughly 8400 particles were generated. The residual degree of saturation, S_r, was found to be 7.3 %, which is very close to the experimental one $S_r = 6.3$ %. About 78400 pores and 157000 pore throats were considered. In the draining phase, suction was increased in 0.1-kPa intervals. The degree of saturation was calculated for each suction step and plotted in Figure 7.31, together with the experimentally acquired SWCC. The two curves show good agreement. At low suctions, lower than air entry value, the simulation demonstrates lower values for saturation than the experimental data. This is because, for high medium density, i.e., low void ratio, the simulation of drainage provides inaccurate values. The specimen used in this research had the minimum void ratio, which resulted in this divergence at low suctions.

In order to derive velocity based on models 1 and 2, fitting parameters should firstly be extracted from Equations 7.4 and 7.5 for the simulated SWCC by means of a statistical nonlinear regression analysis. Table 7.7 summarizes the fitting parameters. The fitting has a good agreement with R^2-values of 97.1 % for Equation (7.4) and 99.4 % for Equation (7.5).

Predictions of normalized velocity calculated after model 1 (Equation 7.11) and model 2 (Equation 7.12) are presented in Fig. 7.32. The parameters used in the models are based on fitting the simulated SWCC with the equations of Van Genuchten (Equation 7.4) and Fredlund and Xing (Equation 7.5), which are listed in Table 7.7. In the simulation, S_r equals 7.3 %. From experimental measurement $\Gamma = 0.05$. It is clear that the models fit the experimental data with

a very good agreement. Model 1 (Equation 7.11) fits data with $R^2 = 98.0$ %, while model 2 (Equation 7.12) achieves $R^2 = 98.4$ %. Both models were found to be equally suitable for describing the data. As described previously, the main difference is that model 1 describes velocity change between saturation and residual value, while model 2 describes velocity change between saturation and dry conditions. For this prediction, material properties were enough to simulate the SWCC. Consequently, the normalized velocity was calculated based on merely two measurements at saturation and residual water content to determine Γ. An extra measurement right after the AEV can improve the accuracy of the prediction. The residual degree of saturation, S_r, is also required, which is experimentally easily obtained.

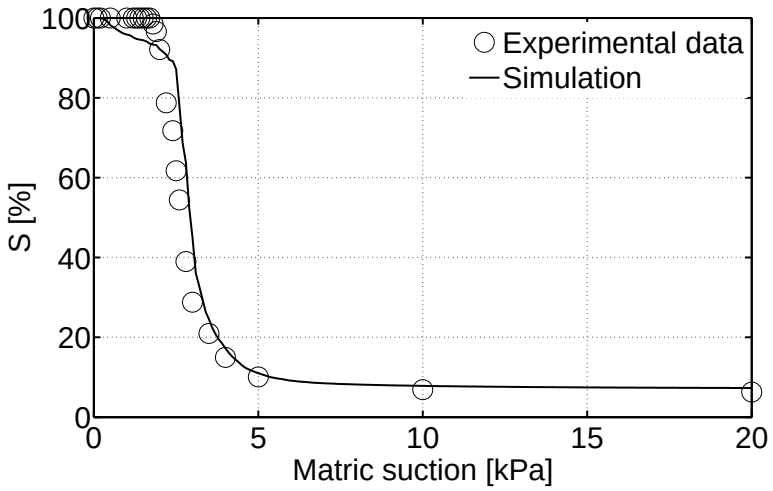

Figure 7.31: Degree of saturation against matric suction for simulation and experimental data

Table 7.7: Modeling parameters for numerical simulation of SWCC

Equation	*Fitting parameters*	R^2
Van Genuchten, Equation 7.4	$a_{vg} = 0.45$, $b_{vg} = 21.16$, $c_{vg} = 0.12$	97.1 %
Fredlund and Xing, Equation 7.5	$a_f = 2.58$, $b_f = 17.56$, $c_f = 0.81$	99.4 %

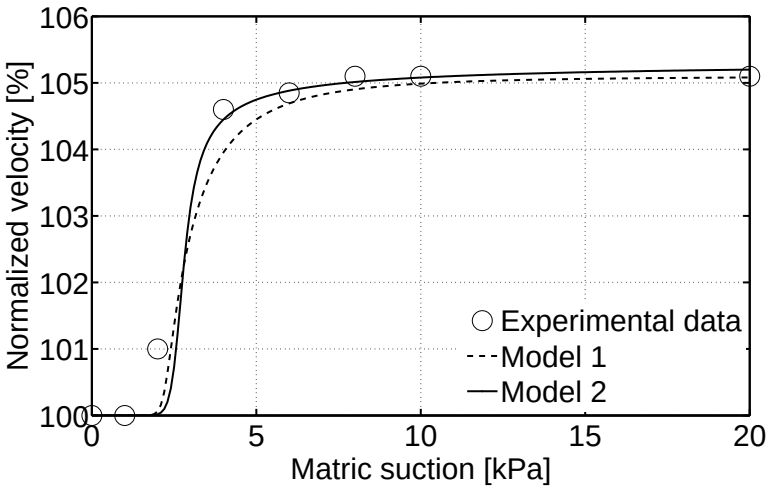

Figure 7.32: Predictions of normalized velocity calculated after model 1 (Equation 7.11) and model 2 (Equation 7.12) based on a simulated SWCC

7.6 Summary

Shear wave velocity was examined for unsaturated soils by means of a special cell that allows controlling two stress state variables, confining pressure and matric suction. Two approaches were developed to predict the change in shear wave velocity with matric suction or degree of saturation. The findings of this chapter can be summarized as follows:

- It was demonstrated that the coda wave interferometry is a robust tool for detecting fabric change in unsaturated soils. The sliding window technique was validated and can be recommended for further use.
- The curve of velocity change during drying has the same shape as the curve of absolute saturation change with suction. This suggests that both phenomena are related.
- A semi-empirical approach was considered to derive models to predict shear wave velocity from SWCC. The models can be written in terms of effective saturation (Equation 7.6), in terms of saturation (Equation 7.9) or in terms of suction (Equations 7.11 and 7.12). The models were validated with new data and data from the literature with good to excellent agreement.
- In order to avoid the difficulty and cost of obtaining the SWCC, a relationship between velocity change and grain size distribution, GSD, was established. It was shown that grain size distribution, which is a very easy, fast and cheap test, is enough to derive the fitting parameters in the proposed model (Equation 7.12).
- In the case of the absence of SWCC and GSD curve, more general models can be used. For these models, knowing a few points is enough to derive the whole gradient curve of velocity between saturation and residual value. The agreement for this case was excellent for the tested soil.
- Assumptions and limitations need to be addressed here. This analysis has been derived for soils with no volume change during drying or wetting. The conclusions here are limited to these soils. However, model 2 (Equation 7.32) was successfully validated with data from the literature that have some degree of volume change. The models are limited to soils with unimodal SWCC, such as the one used in this research. The bimodal SWCC

has more segments and needs additional parameters to be described. It is associated with bimodal grain size distribution [Wijaya & Leong, 2016]. Therefore, the above analysis is not valid for soils with bimodal SWCC. The models did not take into consideration the hysteresis of wetting and drying, and only the drying SWCC was examined. Further validation of the models for other types of soils is recommended, especially in the higher suction range.

- A numerical approach was considered as well so that it can be applied to a wide range of cohesionless soils. The simulation is based on basic soil properties, namely grain size distribution and void ratio. The approach results in the prediction of SWCC, and thus the necessary parameters to predict velocity can be obtained. Combining the analytical models from the semi-empirical approach and the numerical approach allows predicting shear wave velocity without performing the time-consuming test to obtain SWCC based on merely two measurements at saturation and residual water content as well as basic soil properties. This approach was validated with experimental data with a very good agreement. This gives researchers and engineers a valuable tool to assess the dynamic behavior of unsaturated soils for different degrees of saturation.

- For all the above-mentioned models and approaches, velocity measurements at saturation and residual condition are enough to estimate the suction-velocity curve. These extreme measurements, at saturation and residual conditions, are necessary to calculate Γ. An extra measurement right after the AEV can improve the accuracy of the prediction. The residual degree of saturation, S_r, is also required, which is experimentally easily obtained. The effect of creep can be considered here if the extreme measurements were carried out on the same specimen with a significant duration. Equation 6.18 helps to assess how much velocity change is due to creep. Considering Table 6.3, an average value of $\beta = 0.9954$ can be calculated. The ratio between post creep velocity and initial velocity is represented by the term $(t/t_{ref})^{(1-\beta)/4}$. For example, for the tests performed on Hostun sand, t on average was about 40 days. This results in 1.3 % increase in velocity due to creep. Then, $\Gamma_{unsat} = \Gamma_{total} - \Gamma_{creep}$. If the extreme measurements are taken on separate specimens, this correction is not necessary.

Chapter 8

Conclusions and Recommendations

The objective of this research is to investigate the complex behavior of the initial soil parameters, shear stiffness and shear wave velocity, under consideration of multiphase conditions and time effect. Predictive models to describe shear wave and shear modulus under fabric changing processes such as drying and creep were proposed. Such models provide a valuable tool for researchers and engineers to assess soil behavior. This chapter presents the findings of this research and recommendations for further studies.

8.1 Conclusions

This study on process monitoring in granular material has led to the following conclusions:

- The method of coda wave interferometry (CWI) has been proven to be of great usefulness for a wide range of geotechnical applications. This method can detect very small changes in a medium. It was successfully applied to detect slight changes in velocity due to creep and suction increase. An improved technique, the *sliding window technique* that offers stable, accurate results, even in the presence of noise, was presented in Chapter 4. A comparison among different techniques of CWI showed that the stretch technique and the sliding window technique have a great advantage over

the more commonly used doublet technique in the presence of noise. In the absence of noise, all three techniques deliver similar results.

- An analytical study was carried out in Chapter 6 to establish a model for granular material that includes the effect of time (see Equation 6.18). The model relates macro scale shear stiffness G_{eff} to particle parameters f, ν_g, R_c, R_g, G_g, to state parameters cn and σ and to time t. This allows studying the development of G_{eff} in the case of creep as a function of only time t.

- The interparticle friction value can be derived from macro scale shear strength. Friction, f, is directly linked to critical state angle, Φ_{cv}. Value of friction of 0.55 was calculated for Hostun sand. For a different sand, two approaches to estimate friction were suggested in Section 6.3.1.

- The angularity of the particles is considered in the model and calculated for Hostun sand. It was found to be 0.31. Neglecting angularity will result in an overestimation of velocity of 22 % and of shear modulus of 48 % for this sand.

- In order to validate the model in Equation 6.8 and to verify the capability of the coda wave interferometry, the influence of confining pressure on shear wave velocity, v, was examined experimentally. For this purpose, an artificial material was used to study this effect with bender elements. It was demonstrated that the theoretical values of shear modulus from Equation 6.8, where friction, angularity and coordination number were taken into account, explain the experimental data very well. It was also shown that the first arrival method results in the closest values to the theoretical ones.

- Creep has the highest rate in the dry condition for this sand. The presence of water appears to slow creep down. A micromechanical explanation for creep and for the effect of water is presented in Section 6.4. Values for the exponent β in Equation 6.8 are listed in Table 6.3.

- A semi-empirical approach was considered to derive two models to predict shear wave velocity from the soil-water characteristic curve (SWCC). The

models are in terms of effective saturation (Equation 7.6), in terms of saturation (Equation 7.9) or in terms of matric suction (Equations 7.11 and 7.12). They describe the data with good to excellent agreement.

- In order to avoid the difficulty and cost of obtaining the SWCC, a relationship between velocity change and grain size distribution curve was proposed in the semi-empirical approach. It was shown that grain size distribution, which is a very easy, fast and cheap test, is enough to derive the fitting parameters in the proposed model (Equation 7.12).

- In the case of the absence of SWCC and GSD curve, more general models can be used. The necessary parameters for this model are not derived from these curves. The agreement for this case was excellent for the tested soil.

- A numerical approach was developed relying on basic soil properties, namely grain size distribution and void ratio. The approach results in the prediction of SWCC, and thus the necessary parameters to predict velocity can be obtained. Predicting shear wave velocity without performing the time-consuming test to obtain SWCC can then be achieved by combining the analytical models from the semi-empirical approach and the numerical approach. This is based on merely two measurements at saturation and residual water content as well as basic soil properties. This approach was validated with experimental data with a very good agreement.

- For all the above-mentioned models and approaches, velocity measurements at saturation and residual condition are enough to estimate the suction-velocity curve. These extreme measurements, at saturation and residual conditions, are necessary to calculate Γ. An extra measurement right after the AEV can improve the accuracy of the prediction. The residual degree of saturation, S_r, is also required, which is experimentally easily obtained.

8.2 Recommendations

The findings of this research, in addition to the developed tools and approaches, can be used for further investigations of other types of soils and to monitor other phenomena. The following points are suggested for further studies:

- The coda wave interferometry has a huge potential. It can be used to study small changes in soil due to any perturbation, such as temperature, water content, void ratio and cementation.
- Creep can be investigated in fine soils, where it is more present, using CWI to verify the effect of water content found in this research.
- Validating the model in Equation 6.18 for other types of granular material and for other arrays of packing. Combining this model with the coda wave interferometry method results in a trend of velocity that can be compared to absolute velocity methods, like first arrival and cross correlation, to verify the most suitable absolute velocity.
- The approaches proposed here can be utilized to examine velocity change in fine materials, where the SWCC extends into high suctions.

Bibliography

Afifi, S. & Richart, F. (1973). Stress-history effects on shear modulus of soils. *Soils and Foundations*, 13(1), 77–95.

Alabdullah, J. (2010). *Testing unsaturated soil for plane strain conditions: A new double-wall biaxial device*. PhD thesis, Bauhaus-University Weimar, Weimar, Germany.

Alawneh, A., Nusier, O., & Awamleh, M. (2009). Time dependent capacity increase for driven piles in cohesionless soil. *Jordan Journal of Civil Engineering*, 3(1), 1–31.

Alramahi, B., Alshibli, K., & Fratta, D. (2010). Effect of fine particle migration on the small-strain stiffness of unsaturated soils. *Journal of Geotechnical and Geoenvironmental Engineering*, 136(4), 620–628.

Alramahi, B., Alshibli, K., Fratta, D., & Trautwein, S. (2008). A suction-control apparatus for the measurement of p and s-wave velocity in soils. *Geotechnical Testing Journal*, 31(1), 12–23.

Arulnathan, R., Boulanger, R., & Riemer, M. (1998). Analysis of bender element tests. *Geotechnical Testing Journal*, 21(2), 120–131.

Asslan, M. & Wuttke, F. (2010). An experimental study on the initial shear stiffness in granular dry and saturated material using bender elements test. In *the 14th European conference of earthquake engineering*, volume 7 (pp. 5032–5039). Ohrid, Macedonia: Red Hook.

Atkinson, J. (2000). Non-linaer soil stiffness in routine design. *Géotechnique*, 50(5), 487–508.

Atkinson, J. & Sallfors, G. (1991). Experimental determination of soil properties. In *the 10th conference of European soil mechanics*, volume 3 (pp. 915–956). Florence, Italy.

Augustesen, A., Liingaard, M., & Lade, P. (2004). Evaluation of time-dependent behavior of soils. *International Journal of Geomechanics*, 4(3), 137–156.

Bachrach, R. (1998). *High resolution shallow seismic subsurface characterization*. PhD thesis, Stanford University, Stanford, California.

Bachrach, R., Dvorkin, J., & Nur, A. (2000). Seismic velocities and Poisson's ratio of shallow unconsolidated sands. *Geophysics*, 65(2), 559–564.

Baldi, G. & Nova, R. (1984). Membrane penetration effects in triaxial testing. *Journal of Geotechnical Engineering*, 110(3), 403–420.

Barreto, D. & O'Sullivan, C. (2012). The influence of inter-particle friction and the intermediate stress ratio on soil response under generalised stress conditions. *Granular Matter*, 14(4), 505–521.

Baxter, C. (1999). *An experimental study on the aging of sands*. PhD thesis, Virginia Polytechnic Institute and State University, Blacksburg, Virginia.

Benz, T. (2007). *Small-strain stiffness of soils and its numerical consequences*. PhD thesis, University of Stuttgart, Stuttgart, Germany.

Bishop, A. (1954). Correspondence on "Shear characteristics of a saturated silt, measured in triaxial compression". *Géotechnique*, 4(1), 43–45.

Bishop, A. (1959). The principle of effective stress. *Teknisk Ukeblad*, 106(39), 859–863.

Bishop, A. & Donald, I. (1961). The experimental study of partly saturated soils in the triaxial apparatus. In *the 5th international conference on soil mechanics and foundation engineering*, volume 1 (pp. 13–21). Paris, France: Dunod.

Boggs, S. (2006). *Principles of sedimentology and stratigraphy*. Harlow: Pearson Prentice Hall, fourth edition.

Bolton, M. (1986). The strength and dilatancy of sands. *Géotechnique*, 36(1), 65–78.

Brignoli, E., Gotti, M., & Stokoe, K. (1996). Measurement of shear waves in laboratory specimens by means of piezoelectric transducers. *Geotechnical Testing Journal*, 19(4), 384–397.

Bromwell, L. (1966). *The friction of quartz in high vacuum (Phase report No. 7)*. Technical report, Massachusetts Institute of Technology, Vicksburg, Mississippi.

Brooks, R. & Corey, A. (1964). *Hydraulic properties of porous media*. Technical report, Colorado State University, Fort Collins, Colorado.

Caquot, A. (1934). *Équilibre des massifs à frottement interne, stabilité des terres, pulvérulentes ou cohérentes*. Paris: Gauthier-Villars.

Carmichael, R. (1989). *Practical handbook of physical properties of rocks and minerals*. Boca Raton, Florida: CRC Press.

Cavarretta, I., Rocchi, I., & Coop, M. (2011). A new interparticle friction apparatus for granular materials.

Chang, I., Cho, G., Lee, J., & Kim, L. (2006). Characterization of clay sedimentation using piezoelectric bender elements. *Key Engineering Materials*, 321-323, 1415–1420.

Chen, Y., Zhao, Y., Gao, H., & Zheng, J. (2011). Liquid bridge force between two unequal-sized spheres or a sphere and a plane. *Particuology*, 9(4), 374–380.

Cho, G. & Santamarina, J. (2001). Unsaturated particulate materials—particle-level studies. *Journal of Geotechnical and Geoenvironmental Engineering*, 127(1), 84–96.

Chow, F., Jardine, R., Brucy, F., & Nauroy, J. (1998). Effects of time on capacity of pipe piles in dense marine sand. *Journal of Geotechnical and Geoenvironmental Engineering*, 124(3), 254–264.

Clarke, D., Zaccarelli, L., Shapiro, N., & Brenguier, F. (2011). Assessment of resolution and accuracy of the moving window cross spectral technique for monitoring crustal temporal variations using ambient seismic noise. *Geophysical Journal International*, 186(2), 867–882.

Clayton, C. (2011). Stiffness at small strain: Research and practice. *Géotechnique*, 61(1), 5–37.

Dai, S., Wuttke, F., & Santamarina, J. (2013). Coda wave analysis to monitor processes in soils. *Journal of Geotechnical and Geoenvironmental Engineering*, 139(9), 1504–1511.

Daramola, O. (1980). Effect of consolidation age on stiffness of sand. *Géotechnique*, 30(2), 213–216.

Dinesh, S., Yamada, S., & Hyodo, M. (2008). Low strain shear modulus of sand-clay mixtures. *ASCE Geotechnical Special Publication*, 178, 335–342.

Dyvik, R. & Madshus, C. (1985). Laboratory measurements of G_{max} using bender element. In *Advances in the art of testing soils under cyclic conditions* (pp. 186–196). Detroit, Michigan: American Society of Civil Engineerings (ASCE).

Edil, T. & Sawangsuriya, A. (2005). Earthwork quality control using soil stiffness. In *the 16th international conference on soil mechanics and geotechnical engineering* (pp. 1689–1692). Rotterdam, Netherlands: Millpress.

Edlefsen, N. & Anderson, A. (1943). Thermodynamics of soil moisture. *Hilgardia*, 15(2), 31–298.

Ferreira, C., Viana, D., & Santos, J. (2007). Comparison of simultaneous bender elements and resonant column tests on Porto residual soil. In H. I. Ling, L. Callisto, D. Leshchinsky, & J. Koseki (Eds.), *Solid mechanics and its applications*, volume 146 (pp. 523–535). Springer, Dordrecht.

Flavigny, E., Desures, J., & Palayer, B. (1990). Note technique le sable d'Hostun « RF ». *Revue Française Géotechnique*, 53, 67 – 70.

Fox, P., Edil, T., & Lan, L. (1992). C_α/C_c concept applied to compression of peat. *Journal of Geotechnical Engineering*, 118(8), 1256–1263.

Fréchet, J., Martel, L., Nikolla, L., & Poupinet, G. (1989). Application of the cross-spectral moving-window technique (CSMWT) to the seismic monitoring of forced fluid migration in a rock mass. *International Journal of Rock Mechanics and Mining Sciences & Geomechanics Abstracts*, 26(3-4), 221–233.

Fredlund, D. & Rahardjo, H. (1993). *Soil mechanics for unsaturated soils*. New York: John Wiley & Sons.

Fredlund, D., Rahardjo, H., & Fredlund, M. (2012). *Unsaturated soil mechanics in engineering practice*. Hoboken, New Jersey: John Wiley & Sons.

Fredlund, D. & Xing, A. (1994). Equations for the soil-water characteristic curve. *Canadian Geotechnical Journal*, 31(3), 521–532.

Gao, Y., Wang, Y.-H., & Su, J. (2013). Mechanisms of aging-induced modulus changes in sand under isotropic and anisotropic loading. *Journal of Geotechnical and Geoenvironmental Engineering*, 139(9), 470–482.

García, X. & Medina, E. (2006). Hysteresis effects studied by numerical simulations: Cyclic loading-unloading of a realistic sand model. *Geophysics*, 71(2), F13.

Gavin, K., Jardine, R., Karlsrud, K., & Lehane, B. (2015). The effects of pile ageing on the shaft capacity of offshore piles in sand. In *the 3rd international symposium frontiers in offshore geotechnics*, volume 1 (pp. 129–152). Oslo, Norway: CRC Press.

Goudarzy, M. (2015). *Micro and macro mechanical assesssment of small and intermediate strain properties of granular material*. PhD thesis, Ruhr-Universität Bochum, Bochum, Germany.

Grêt, A., Snieder, R., & Özbay, U. (2006a). Monitoring in situ stress changes in a mining environment with coda wave interferometry. *Geophysical Journal International*, 167(2), 504–508.

Grêt, A., Snieder, R., & Scales, J. (2006b). Time-lapse monitoring of rock properties with coda wave interferometry. *Journal of Geophysical Research*, 111(B03305), 1–11.

Hadziioannou, C., Larose, E., Coutant, O., Roux, P., & Campillo, M. (2009). Stability of monitoring weak changes in multiply scattering media with ambient noise correlation: Laboratory experiments. *Journal of the Acoustical Society of America*, 125(6), 3688–3695.

Head, K. (1986). *Manual of soil laboratory testing*, volume 3. London, United Kingdom: Pentech Press.

Hilf, J. (1956). *An investigation of pore-water pressure in compacted cohesive soils (Technical memorandum 654).* Technical report, U.S. Department of the Interior, Bureau of Reclamation, Denver, Colorado.

Holtzman, R., Silin, D., & Patzek, T. (2010). Frictional granular mechanics: A variational approach. *International Journal for Numerical Methods in Engineering*, 81(10), 1259–1280.

Horn, H. & Deere, D. (1962). Frictional characteristics of minerals. *Géotechnique*, 12(4), 319–335.

Horne, M. (1965a). The behaviour of an assembly of rotund, rigid, cohesionless particles. I. *Proceedings of the Royal Society of London. Series A, Mathematical, Physical and Engineering Sciences*, 286(1404), 62–78.

Horne, M. (1965b). The behaviour of an assembly of rotund, rigid, cohesionless particles. II. *Proceedings of the Royal Society of London. Series A, Mathematical, Physical and Engineering Sciences*, 286(1404), 79–97.

Horne, M. (1969). The behaviour of an assembly of rotund, rigid, cohesionless particles. III. *Proceedings of the Royal Society of London. Series A, Mathematical, Physical and Engineering Sciences*, 310(1500), 21–34.

Houston, W., Mirza, M., & Zapata, C. (2006). *Environmental effects in pavement mix and structural design systems.* Technical report, Arizona State University.

Hoyos, L. & Macari, E. (2001). Development of a stress/suction-controlled true triaxial testing device for unsaturated soils. *Geotechnical Testing Journal*, 24(1), 5–13.

Hoyos, L., Takkabutr, P., Puppala, A., & Hosain, M. (2008). Dynamic response of unsaturated soils using resonant column and bender elements testing techniques. *ASCE Geotechnical Special Publication*, 181, 485–492.

Hsu, C.-C. & Vucetic, M. (2004). Volumetric threshold shear strain for cyclic settlement. *Journal of Geotechnical and Geoenvironmental Engineering*, 130(1), 58–70.

Inci, G., Yesiller, N., & Kagawa, T. (2003). Experimental investigation of dynamic response of compacted clayey soils. *Geotechnical Testing Journal*, 26(2), 125–141.

Ishihara, K. (1996). *Soil behaviour in earthquake geotechnics*. Oxford, United Kingdom: Clarendon Press.

Ivković, B., Djurdjanović, M., & Stamenković, D. (2000). The Influence of the contact surface roughness on the static friction coefficient. *Tribology in Industry*, 22(3&4), 41–44.

Jardine, R., Standing, J., & Chow, F. (2006). Some observations of the effects of time on the capacity of piles driven in sand. *Géotechnique*, 56(4), 227–244.

Jensen, J., Augustesen, A., & Sørensen, C. (2004). The influence of time on the bearing capacity of driven piles. In *the 14th Nordic geotechnical meeting* (pp. 103–111). Ystad, Sweden: Swedish Geotechnical Society.

Jovičić, V., Coop, M., & Simić, M. (1996). Objective criteria for determining G_{max} from bender element tests. *Géotechnique*, 46(2), 357–362.

Kang, D., Yun, T., Lau, Y., & Wang, Y. (2012). DEM simulation on soil creep and associated evolution of pore characteristics. *Computers and Geotechnics*, 39, 98–106.

Karlsrud, K., Jensen, T., Lied, E., Nowacki, F., & Simonsen, A. (2014). Significant ageing effects for axially loaded piles in sand and clay verified by new field load tests. In *the annual offshore technology conference*, volume 2 (pp. 1307–1325). Houston, Texas: Offshore Technology Conference (OTC).

Kramer, S. (1996). *Geotechnical earthquake engineering*. Upper Saddle River, New Jersey: Prentice Hall.

Kraus, H. (1980). *Creep analysis*. New York: John Wiley & Sons.

Kuwano, R. & Jardine, R. (2002). On measuring creep behaviour in granular materials through triaxial testing. *Canadian Geotechnical Journal*, 39(5), 1061–1074.

Lade, P. (2009). Creep, stress relaxation, and rate effects in sand. In *the 17th international conference on soil mechanics and geotechnical engineering*, volume 1 (pp. 264–267). Alexandria, Egypt: IOS Press.

Lade, P., Liggio, C., & Nam, J. (2009). Strain rate, creep, and stress drop-creep experiments on crushed coral sand. *Journal of Geotechnical and Geoenvironmental Engineering*, 135(7), 941–953.

Lambe, T. & Whitman, R. (1979). *Soil mechanics, SI version*. New York: John Wiley & Sons.

Landon, M. & DeGroot, D. (2006). Measurement of small strain shear modulus anisotropy on unconfined clay samples using bender elements. In *GeoCongress 2006: Geotechnical engineering in the information technology* (pp. 179–184). Atlanta, Georgia: American Society of Civil Engineers.

Lee, C. & Huang, H. (2007). Wave velocities and their relation to fabric evolution during the shearing of sands. *Soil Dynamics and Earthquake Engineering*, 27(1), 1–13.

Lee, I. (1966). Stress-dilatancy performance of feldspar. *Journal of the Soil Mechanics and Foundations Division*, 92(2), 79–103.

Leonards, G. & Altschaeffl, A. (1964). Compressibility of clay. *Journal of the Soil Mechanics and Foundations Division*, 90(5), 133–156.

Leong, E. & Rahardjo, H. (1997). Review of soil-water characteristic curve equations. *Journal of Geotechnical and Geoenvironmental Engineering*, 123(12), 1106–1117.

Leroueil, S. (1996). Compressibility of clays: Fundamental and practical aspects. *Journal of Geotechnical Engineering*, 122(7), 534–543.

Li, Y., Xu, Y., & Thornton, C. (2005). A comparison of discrete element simulations and experiments for 'sandpiles' composed of spherical particles. *Powder Technology*, 160(3), 219–228.

Lim, J. & Lehane, B. (2015). Time effects on the shaft capacity of jacked piles in sand. *Canadian Geotechnical Journal*, 52(11), 1830–1838.

Mair, R. (1993). Developments in geotechnical engineering research: Application to tunnels and deep excavations. *Proceedings of Institution of Civil Engineering: Civil Engineering*, 97(1), 27–41.

Makhlouf, H. & Stewart, J. (1967). Elastic constants of cubical-tetrahedral and tetragonal sphenoidal arrays of uniform spheres. In *International symposium of wave propagation and dynamic properties of earth materials* (pp. 825–837). Albuquerque, New Mexico: University of New Mexico Press.

Mancuso, C., Vassallo, R., & D'Onofrio, A. (2002). Small strain behavior of a silty sand in controlled-suction resonant column–torsional shear tests. *Canadian Geotechnical Journal*, 39(1), 22–31.

Manegold, E. & Engelhardt, W. (1933). Über Kapillar-Systeme, XII (4). Die Berechnung des Stoffgehaltes heterogener Gerüststrukturen. *Kolloid-Zeitschrift*, 63(2), 149–154.

Marinho, F., Chandler, R., & Crilly, M. (1995). Stiffness measurements on an unsaturated high plasticity clay using bender elements. In *the 1st international conference on unsaturated soils, UNSAT '95* (pp. 535–539). Paris, France: Balkema.

Mavko, G., Mukerji, T., & Dvorkin, J. (2009). *The rock physics handbook: Tools for seismic analysis of porous media*. New York: Cambridge University Press, second edition.

McKee, C. & Bumb, A. (1987). Flow-testing coalbed methane production wells in the presence of water and gas. *Spe Formation Evaluation*, 2(4), 599–608.

Mesri, G., Feng, T., & Benak, J. (1990). Postdensification penetration resistance of clean sands. *Journal of Geotechnical Engineering*, 116(7), 1095–1115.

Mikesell, T., Malcolm, A., Yang, D., & Haney, M. (2015). A comparison of methods to estimate seismic phase delays: Numerical examples for coda wave interferometry. *Geophysical Journal International*, 202(1), 347–360.

Mindlin, R. (1949). Compliance of elastic bodies in contact. *Journal of Applied Mechanics*, 16, 259–268.

Mindlin, R. (1954). *Mechanics of granular media (Report No. 14)*. Technical report, Columbia University, New York.

Mitchell, J. & Soga, K. (2005). *Fundamentals of soil behavior*. Hoboken, New Jersey: John Wiley & Sons.

Modoni, G., Flora, A., Mancuso, C., Anh Dan, L., Koseki, J., Balakrishnaiyer, K., & Tatsuoka, F. (1999). A simple experimental procedure for the complete characterization of small strain stiffness of gravels. In *Pre-failure deformation characteristics of geomaterials* (pp. 123–130). Torino, Italy: Balkema.

Moroto, N. (1988). Some considerations on shearing resistance angles of sands. In *Micromechanics of granular materials: Proceedings of the U.S./Japan seminar on the micromechanics of granular materials*, volume 20 (pp. 47–54). Sendai-Zao, Japan: Elsevier.

Mualem, Y. (1976). A new model for predicting the hydraulic conductivity of unsaturated porous media. *Water Resources Research*, 12(3), 513–522.

Murphy, W. (1982). *Effects of microstructure and pore fluids on the acoustic properties of granular sedimentary materials*. PhD thesis, Stanford University, Stanford, California.

Nascimento, U. (1981). *Lubricant and antilubricant effects of water (Memória 56)*. Technical report, LNEC - Laboratório Nacional de Engenharia Civil, Lisbon, Portugal.

Nazarian, S. & Yuan, D. (2008). Variation in moduli of base and subgrade with moisture. *ASCE Geotechnical Special Publication*, 178, 570–577.

Norwegian Geotechnical Institute (2014). *Time effects on pile capacity: Summary and evaluation of test results (Report No. 20061251-00-279-R, 1. Revision. March 2014)*. Technical report, Norwegian Geotechnical Institute.

Oh, W. & Vanapalli, S. (2014). Semi-empirical model for estimating the small-strain shear modulus of unsaturated non-plastic sandy soils. *Geotechnical and Geological Engineering*, 32(2), 259–271.

Omar, T. & Sadrekarimi, A. (2014). Effects of multiple corrections on triaxial compression testing of sands. *Journal of GeoEngineering*, 9(2), 33–40.

Pennington, D., Nash, D., & Lings, M. (2001). Horizontally mounted bender elements for measuring anisotropic shear moduli in triaxial clay specimens. *Geotechnical Testing Journal*, 24(2), 133–144.

Pestana, J. & Salvati, L. (2006). Small-strain behavior of granular soils. I: Model for cemented and uncemented sands and gravels. *Journal of Geotechnical and Geoenvironmental Engineering*, 132(8), 1071–1081.

Pettijohn, F. (1949). *Sedimentary rocks*. New York: Harper and brothers.

Picornell, M. & Nazarian, S. (1998). Effect of soil suction on the low-strain shear modulus of soils. In *the 2nd international conference on unsaturated soils*, volume 2 (pp. 102–107). Beijing, China: International Academic Publishers.

Piriyakul, K. (2006). *Anisotropic stress-strain behaviour of Belgian boom clay in the small strain region*. PhD thesis, Ghent University, Ghent, Belgium.

Porras Ortiz, O. (2004). *Small and large strain monitoring of unsaturated soil behavior by means of multiaxial testing and shear wave propagation*. PhD thesis, Louisiana State University, Baton Rouge, Louisiana.

Poupinet, G., Ellsworth, W., & Fréchet, J. (1984). Monitoring velocity variations in the crust using earthquake doublets: An application to the Calaveras Fault, California. *Journal of Geophysical Research*, 89(B7), 5719–5731.

Powers, M. (1953). A new roundness scale for sedimentary particles. *Journal of Sedimentary Petrology*, 23(2), 117–119.

Procter, D. & Barton, R. (1974). Measurements of the angle of interparticle friction. *Géotechnique*, 24(4), 581–604.

Rowe, P. (1962). The stress-dilatancy relation for static equilibrium of an assembly of particles in contact. *Proceedings of the Royal Society of London. Series A, Mathematical, Physical and Engineering Sciences*, 269(1339), 500–527.

Russell, R. & Taylor, R. (1937). Roundness and shape of Mississippi river sands. *The Journal of Geology*, 45(3), 225–267.

Sadek, T., Lings, M., Dihoru, L., & Wood, D. (2007). Wave transmission in Hostun sand: Multiaxial experiments. *Rivista Italiana di Geotecnica*, 41(2), 69–84.

Sanchez-Salinero, I. (1987). *Analytical investigation of seismic methods used for engineering applications*. PhD thesis, University of Texas at Austin, Austin, Texas.

Santamarina, J., Klein, K., & Fam, M. (2001). *Soils and waves: Particulate materials behavior, characterization and process monitoring*. Chichester: Wiley & Sons.

Sattari, A. (2014). *Obtaining soil-water characteristic curves by numerical modeling of drainage in particulate media*. Master thesis, Middle East Technical University, Ankara, Turkey.

Sattari, A. & Toker, N. (2016). Obtaining soil-water characteristic curves by numerical modeling of drainage in particulate media. *Computers and Geotechnics Journal*, 74, 196–210.

Sawangsuriya, A. (2006). *Stiffness-suction-moisture relationship for compacted soils*. PhD thesis, University of Wisconsin-Madison, Madison, Wisconsin.

Sawangsuriya, A., Edil, T., & Bosscher, P. (2008). Modulus-suction-moisture relationship for compacted soils. *Canadian Geotechnical Journal*, 45(7), 973–983.

Sawangsuriya, A., Edil, T., & Bosscher, P. (2009). Modulus-suction-moisture relationship for compacted soils in postcompaction state. *Journal of Geotechnical and Geoenvironmental Engineering*, 135(10), 1390–1403.

Schanz, T. & Vermeer, P. (1996). Angles of friction and dilatancy of sand. *Géotechnique*, 46(1), 145–151.

Schmertmann, J. (1991). The mechanical aging of soils. *Journal of Geotechnical Engineering*, 117(9), 1288–1330.

Schultheiss, P. (1981). Simultaneous measurement of P & S wave velocities during conventional laboratory testing procedures. *Marine Geotechnology*, 4(4), 343–367.

Scott, R. (1963). *Principles of soil mechanics*. Reading, Massachusetts: Addison-Wesley.

Seed, H., Wong, R., Idriss, I., & Tokimatsu, K. (1986). Moduli and damping factors for dynamic analyses of cohesionless soils. *Journal of Geotechnical and Geoenvironmental Engineering*, 112(11), 1016–1032.

Sens-Schönfelder, C. & Larose, E. (2008). Temporal changes in the lunar soil from correlation of diffuse vibrations. *Physical Review E: Statistical, Nonlinear, and Soft Matter Physics*, 78(4), 045601.

Senthilmurugan, T. & Ilamparuthi, K. (2005). Study of compaction characteristics and strength through ultrasonic methods. *ASCE Geotechnical Special Publication*, 130, 1–12.

Shirley, D. (1978). An improved shear wave transducer. *Journal of Acoustical Society of America*, 63(5), 1643–1645.

Shirley, D. & Hampton, L. (1978). Shear wave measurements in laboratory sediments. *Journal of Acoustical Society of America*, 63(2), 607–613.

Silva, C., Ortiz, O., Fratta, D., & Macari, E. (2002). Mechanical response of unsaturated particulate materials – A stiffness assessment study under controlled matric suction. In *the ASME international mechanical engineering congress & exposition* (pp. 269–274). New Orleans, Louisiana: American Society of Mechanical Engineers.

Skinner, A. (1969). A note on the influence of interparticle friction on the shearing strength of a random assembly of spherical particles. *Géotechnique*, 19(1), 150–157.

Smith, W., Foote, P., & Busang, P. (1929). Packing of homogeneous spheres. *Physical Review*, 34(9), 1271–1274.

Snieder, R. (2004). Coda wave interferometry. In *McGraw-Hill yearbook of science & technology* (pp. 54–56). New York: McGraw-Hill.

Snieder, R. (2006). The theory of coda wave interferometry. *Pure and Applied Geophysics*, 163(2-3), 455–473.

Snieder, R. & Hagerty, M. (2004). Monitoring change in volcanic interiors using coda wave interferometry: Application to Arenal Volcano, Costa Rica. *Geophysical Research Letters*, 31(L09608).

Stokoe, K. & Richart, F. (1973). Shear moduli of soils, in-situ and from laboratory tests. In *the 5th world conference on earthquake engineering*, volume 1 (pp. 356–359). Rome, Italy.

Takkabutr, P. (2006). *Experimental investigations on small-strain stiffness properties of partially saturated soils via resonant column and bender element testing*. PhD thesis, University of Texas at Arlington, Arlington, Texas.

Tinjum, J., Benson, C., & Blotz, L. (1997). Soil-water characteristic curves for compacted clays. *Journal of Geotechnical and Geoenvironmental Engineering*, 123(11), 1060–1069.

Torres Hernandez, G. (2011). *Estimating the soil-water characteristic curve using grain-size analysis and plasticity index*. Master thesis, Arizona State University.

Van Genuchten, M. (1980). A closed-form equation for predicting the hydraulic conductivity of unsaturated soils. *Soil Science Society of America Journal*, 44(5), 892–898.

Viggiani, G. & Atkinson, J. (1995). Stiffness of fine-grained soil at very small strains. *Géotechnique*, 45(2), 249–265.

Vucetic, M. (1994). Cyclic threshold shear strains in soils. *Journal of Geotechnical and Geoenvironmental Engineering*, 120(12), 2208–2228.

Wadell, H. (1932). Volume, shape, and roundness of rock particles. *Journal of Geology*, 40(5), 443–451.

Walton, K. (1987). The effective elastic moduli of a random pack of spheres. *Journal of the Mechanics and Physics of Solids*, 35(2), 213–226.

Wang, Y.-H., Gao, Y., & Leng, G. (2016). Experimental characterizations of an aging mechanism of sands. *Journal of Geotechnical and Geoenvironmental Engineering*, 142(2), 06015016.

Wang, Y.-H. & Tsui, K.-Y. (2009). Experimental characterization of dynamic property changes in aged sands. *Journal of Geotechnical and Geoenvironmental Engineering*, 135(2), 259–270.

Wang, Y.-H., Xu, D., & Tsui, K. (2008). Discrete element modeling of contact creep and aging in sand. *Journal of Geotechnical and Geoenvironmental Engineering*, 134(9), 1407–1411.

Weidinger, D., Ge, L., & Stephenson, R. (2009). Ultrasonic pulse velocity tests on compacted soil. *ASCE Geotechnical Special Publication*, 189, 150–155.

Wichtmann, T. & Triantafyllidis, T. (2009). On the influence of the grain size distribution curve of quartz sand on the small strain shear modulus G_{max}. *Journal of Geotechnical and Geoenvironmental Engineering*, 135(10), 1404–1418.

Wijaya, M. & Leong, E. (2016). Equation for unimodal and bimodal soil-water characteristic curves. *Soils and Foundations*, 56(2), 291–300.

Wuttke, F., Asslan, M., & Schanz, T. (2012). Time-lapse monitoring of fabric changes in granular materials by coda wave interferometry. *Geotechnical Testing Journal*, 35(2), 353–362.

Yesiller, N., Inci, G., & Miller, C. (2000). Ultrasonic testing for compacted clayey soils. *ASCE Geotechnical Special Publication*, 99, 54–68.

Youn, J.-U., Choo, Y.-W., & Kim, D.-S. (2008). Measurement of small-strain shear modulus G_{max} of dry and saturated sands by bender element, resonant column, and torsional shear tests. *Canadian Geotechnical Journal*, 45(10), 1426–1438.

Zapata, C. (1999). *Uncertainty in soil-water-characteristic curve and impacts on unsaturated shear strength predictions*. Phd thesis, Arizona State University.

Zapata, C., Houston, W., Houston, S., & Walsh, K. (2000). Soil-water characteristic curve variability. *ASCE Geotechnical Special Publication*, 99, 84–124.

Zeng, X. & Grolewski, B. (2005). Measurement of G_{max} and rstimation of K_0 of saturated clay using bender elements in an oedometer. *Geotechnical Testing Journal*, 28(3), 264–274.

The initial shear stiffness at small strain is a signif cant factor to consider for a wide range of geotechnical applications. Determining this initial parameter is critical for describing dynamic soil behavior in the case of wave, wind, machine or traff c vibrations. It is very sensitive to fabric changing processes. Monitoring shear wave velocity, which is directly related to shear stiffness, is an effective tool to detect these fabric changing processes in soil. The complex behavior of initial soil parameters, namely initial shear stiffness and shear wave velocity, under consideration of multiphase conditions and time effect, is in the focus of this research.

In this thesis, two fabric changing processes, namely creep and unsaturation, were detected experimentally using a signal processing tool called coda wave interferometry and described mathematically. For creep, a model that describes the evolution of shear stiffness is presented. This model includes, in addition to the time effect, other physical soil properties at the micro scale, such as particle parameters (interparticle friction, angularity and grain properties) and state parameters (coordination number and conf ning pressure). For unsaturated soils, a predictive relationship based on semi-empirical or alternatively numerical approaches that describes the change in shear wave velocity with matric suction or degree of saturation is proposed. This gives researchers and engineers a valuable tool to assess the dynamic behavior of unsaturated soils for different degrees of saturation.

ISSN: 2365-7162